NTNU – Trondheim
Norwegian University of
Science and Technology

Targeting kinetics of RGD-conjugated nanoemulsions

Linda Sønstevold

Nanotechnology
Submission date: June 2015
Supervisor: Catharina de Lange Davies, IFY

Norwegian University of Science and Technology
Department of Physics

Abstract

The overall aim of this project was to study targeting kinetics of fluorescently labelled RGD-conjugated nanoemulsions (RGD-NE) to $\alpha_v\beta_3$-expressing human umbilical vein endothelial cells, and obtain a better understanding of how kinetics of $\alpha_v\beta_3$ internalisation and recycling, affect nanoemulsion (NE) targeting kinetics. An understanding of these kinetics may contribute to obtain more efficient delivery of NE. Flow cytometry and confocal laser scanning microscopy was used for analysis. One part of the project concerned investigation of the credbility of an hypothesis proposed by Hak et al., where *in vivo* periodicity in NE targeting kinetics was explained by $\alpha_v\beta_3$ binding, internalisation and recycling kinetics. In accordance with the hypothesis, saturation binding of surface $\alpha_v\beta_3$-integrins by RGD-NE, was found within 2.5 min for concentrations above 0.1 mM. Immunolabelling indicated RGD-NE incubation reduced surface expression of $\alpha_v\beta_3$-integrins, when incubated 10 min or longer. The indicated enhancement of $\alpha_v\beta_3$ internalisation by RGD-NE binding, is in compliance with Hak et al.'s hypothesis, but the *time frame* and *extent* of enhanced internalisation is not. Also, from modifications of *in vitro* experiments performed by Hak et al., results suggest that the time frame or other assumptions regarding the occurence of $\alpha_v\beta_3$ internalisation and recycling in the hypothesis, is likely not correct. Together, this indicates that the observed *in vivo* targeting periodicity is not (only) caused by $\alpha_v\beta_3$ kinetics. The other part of the project concerned the establishment of a protocol based on confocal laser scanning microscopy, where the cellular distribution of $\alpha_v\beta_3$-integrins and RGD-NE could be monitored during NE incubation. Fixation was tested, but live cell imaging was prioritised in development of the protocol. NE incubation was performed on the microscope and imaged in real-time. To study kinetics of NE internalisation and trafficking to the perinuclear region, cell stainings were tested to detect regions-of-interest for whole cell cytosols and perinuclear regions throughout the time series. Staining with Hoechst 34580 and Calcein AM was found suitable for this. However, in contrast to unstained cells, no NE uptake and cell death was observed with these stainings, most likely due to phototoxicity. Optimisation of the imaging process is therefore needed for usage in intended studies. To monitor $\alpha_v\beta_3$ internalisation and recycling kinetics, transfection of a GFP-tagged β_3-integrin was tested. The method showed potential, but further studies and optimisation of transfection protocols are necessary before kinetics may be monitored.

Sammendrag

Formålet med denne oppgaven, var å studere kinetikken i opptaket av RGD-konjugerte nanoemulsjoner (RGD-NE) i endotelceller som uttrykker reseptoren $\alpha_v\beta_3$-integrin, for å oppnå en bedre forståelse av hvordan kinetikken til $\alpha_v\beta_3$-internalisering og -resirkulering, påvirker kinetikken i opptaket av nanoemulsjonene (NE). En slik forståelse kan bidra til å oppnå mer effektiv levering av NE. NE var merket med fluroforer, og analyse ble utført med flow cytometri eller konfokalmikroskopi. En del av prosjektet omhandlet å undersøke troverdigheten til en hypotese foreslått av Hak et al., der en observert *in vivo* periodisitet i opptak av NE ble forklart ut fra kinetikk i $\alpha_v\beta_3$-binding, -internalisering og -resirkulering. I overensstemmelse med hypotesen, ble det funnet at metning av overflatebinding av $\alpha_v\beta_3$ hendte innen 2.5 min for konsentrasjoner over 0.1 mM. Immunomerking indikerte at inkubasjon med RGD-NE reduserte overflateekspresjonen av $\alpha_v\beta_3$-integriner ved inkubasjon i 10 min eller lenger. Den indikerte økningen i $\alpha_v\beta_3$-internalisering stemmer med hypotesen til Hak et al., men tidsrammen og mengden $\alpha_v\beta_3$ som internaliseres, stemmer ikke. Fra videreutvikling av *in vitro* forsøk utført av Hak et al., tyder også resultatene på at tidsrammen eller andre antakelser angående hendelsesforløpet til $\alpha_v\beta_3$-internalisering og -resirkulering, sannsynligvis ikke er riktig. Totalt tyder dette på at den observerte *in vivo* periodisiteten i opptak av NE, ikke er (alene) forårsaket av $\alpha_v\beta_3$-kinetikk. Den andre delen av prosjektet gikk ut på å utvikle en protokoll basert på konfokalmikroskopi, der den cellulære fordelingen av $\alpha_v\beta_3$-integriner og RGD-NE kunne følges under inkubasjon med NE. Fiksering ble tested, men avbilding av levende celler ble prioritert i utviklingen av protokollen. Celler ble inkubert med NE mens de ble avbildet på mikroskopet i en tidsserie. For å studerer kinetikk i internalisering av RGD-NE og intracellular transport til området rundt cellekjernen, ble ulike cellemerkinger testet for å detektere omrisset av de relevante områdene gjennom hele tiddserien. Merking med Hoechst 34580 og Calcein AM passet til å detektere områdene, men i motsetning til for celler uten merking, ble ingen opptak av NE observert og celler så ut til å dø under avbilding når de var merket med disse. Dette skyldes mest sannsynlig fototoksisitet, og videre optimalisering av avbildingsprosedyren er nødvendig før den kan benyttes til å utføre studiene som var tiltenkt. For å overvåke kinetikken til $\alpha_v\beta_3$-internalisering og -resirkulering ble transfeksjon av GFP-merket β_3-integrin testet. Metoden viste potensial, men videre studier og optimalisering av transfeksjonsprotokollen er nødvendig før kinetikken til $\alpha_v\beta_3$ kan monitoreres med denne metoden.

Preface

This project was carried out at the Norwegian University of Science and Technology, at the Department of Physics during the spring 2015. I would like to give a special thank to my supervisors Sjoerd Hak and Catharina de Lange Davies for their steady guidance and assistance throughout the semester. Especially, I would like to thank Sjoerd for training in and assistance with laboratory techniques. Furthermore, I would like to thank Kristin G. Sæterbø for training and guidance regarding HUVEC culturing and flow cytometry, and Astrid Bjørkøy for training and assistance with confocal laser scanning microcopy experiments, and to thank both for helpful advice througout the semester.

Contents

1 Introduction

Cancer represents a leading cause of death worldwide, and caused 8.2 million deaths in 2012 [1]. To increase cancer survival rates, there is a strong need for earlier detection and more specific cancer therapies than what we have today. The use of nanoparticles is a novel approach in cancer therapy and diagnostics, which shows potential to achieve this. Anti-cancer and contrast agents may be incorporated in nanoparticles, and the nanoparticles may be directed to interact only with specific cells and tissue, e.g. by the conjugation of targeting ligands. This may provide increased efficacy and reduced side-effects of treatment, and allow for *in vivo* molecular imaging for early detection of cancerous tissue [2, 3, 4].

The formation of new blood vessels (angiogenesis) is a hallmark of a growing tumor. Targeting angiogenesis therefore represents a method to target cancer. This method has the advantage that the blood vessel lumens are directly available to circulating species, which significantly ease the targeting process [5]. Targeting angiogenesis by targeting the receptor $\alpha_v\beta_3$-integrin on blood vessel endothelial cells, has been studied for decades, and show potential both for anti-angiogenic therapy and diagnostic purposes [5, 6, 7, 8]. However, there has been little emphasis on the fact that $\alpha_v\beta_3$-integrin is a recycling receptor, although this may significantly affect targeting kinetics [9].

One of the few studies adressing $\alpha_v\beta_3$ recycling in the context of *in vivo* targeting kinetics of nanoparticles targeted to this receptor, is a study by Hak et al. [9] published in 2013. Here, a periodicity in targeting kinetics of ligand-functionalised nanoparticles to tumor vasculature was observed, where the accumulation of nanoparticles first rapidly increase, then level off, and followingly increase further. In the paper, Hak et al. propose an hypothesis of how binding, internalisation, and recycling of $\alpha_v\beta_3$-integrins, may account for the observed periodicity. They also performed *in vitro* experiments, which support their hypothesis. In the hypothesis, the temporary halt in nanoparticle accumulation is explained by temporary few available $\alpha_v\beta_3$-integrins on the cell surfaces.

If receptor recycling is, in fact, the cause of the observed periodicity, this could have important implications, e.g. for optimisation of dosage regimes for agents targeted to $\alpha_v\beta_3$-integrin [6]. As administration of targeted therapeutics will only be effectful when the receptors are available, long, continuous drug administration could be exchanged by shorter, multiple administrations, without reducing the overall delivery to the target cells. This could significanlty reduce both side-effects and the cost of therapy.

In experiments by Hak et al., nanoemulsions (NE) conjugated to the targeting ligand RGD (arginine-glycine-aspartate) peptide was used. The overall aim of this project was to study further the targeting kinetics of RGD-conjugated NE to $\alpha_v\beta_3$-expressing cells *in vitro*, as initiated by Hak et al. More specifically, the project may be divided in two aims: **1:** To investigate *in vitro* if the hypothesis proposed by Hak et al., concerning receptor recycling kinetics as a cause of observed *in vivo* targeting kinetics of RGD-conjugated NE, may in fact be correct. **2:** To develop an experimental protocol based on confocal laser scanning microscopy, where the cellular distribution of $\alpha_v\beta_3$-integrins and RGD-conjugated NE, may be monitored during NE-incubation, to study internalisation and recycling kinetics of $\alpha_v\beta_3$-integrins, and internalisation and intracellular trafficking kinetics of NE.

2 Theory

2.1 Cancer; challenges of conventional therapy and diagnostics

Cancer defines a large group of diseases characterised by the ability of cancer cells to undergo uncontrolled cell division and spread throughout the body. Cancer may develop in almost any organ, and there are more than a hundred distinguishable cancer types. Cancer typically arises due to a mutation in a cells genome, which may be caused by both external factors like tobacco, infectious organisms and radiation, and internal factors like inherited and spontaneous mutations. One of the main causes of the high death rates of cancer, is the cancer cells' ability to spread to other parts of the body (metastasise). In fact, 90% of cancer deaths are caused by metastases rather than by the primary tumor, due to attack on vital organs [10].

Today, several therapeutic approaches are utilised in the attempt to treat different cancer types. However, the number of cancer deaths are still high. The typical treatment strategy today is removal of the tumor by surgery, followed by cytotoxic chemotherapy and/or radiotherapy [3]. A significant disadvantage of chemo- and radiotherapy is that they are non-specific to cancer cells and thus may also kill healthy cells, causing severe side-effects. This reduces the dose which may be used to treat a patient, and thereby also reduces the chance of defeating the cancer [11, 12]. One of the great challenges in cancer therapy is, in fact, to achieve a high enough delivery of anticancer agents to the cancerous tissue, without injuring other parts of the body [2].

Another great challenge for successful defeat of cancerous diseases, is that most cancers are discovered too late. For example, by the time patients are diagnosed with breast, lung, colon and ovarian cancer, more than 60% already have hidden or known metastases. For these patients, the available treatments are often unable to reverse the course of the disease. Successful treatment is much more likely at an early stage of cancer developement and before metastasis occur. Unfortunately, today's clinical imaging technologies, such as magnetic resonance imaging (MRI), computed tomography (CT), positron emission tomography (PET) and ultrasound (US), do still not offer sufficient sensitivity and spatial resolution for early detection of precancerous and neoplastic lesions. Hence, a key contribtion to increasing the survival rates from cancer, is the development of novel diagnostic tools for early detection of tumor development [3].

2.2 Novel strategies; nanoparticles in medicine

The use of entities called *nanoparticles* in medical applications (Figure 1), has experienced increasing interest the last decades, also within cancer research. The use of nanoparticles is part of the evolving field of nanomedicine, where several disciplines, like biology, chemistry, physics and medicine, are combined to develop novel nanotechnology-based platforms for biomedical applications [6, 13, 14, 15]. The use of nanoparticles in medicine offer several benefits compared to conventional therapy, and

may help overcome some of the challenges of cancer therapy and improve cancer diagnostics. Typical nanoparticles used in medical research today are entities ranging from one to several hundred nanometers in size [16, 17]. In comparison, typical proteins are 1-20 nm in size [18]. Nanoparticles may be used to carry drugs and/or contrast agents, and be directed to specific sites in the body. This allows for the design of specialised drug delivery systems and novel imaging techniques, or even a combination of the two [3].

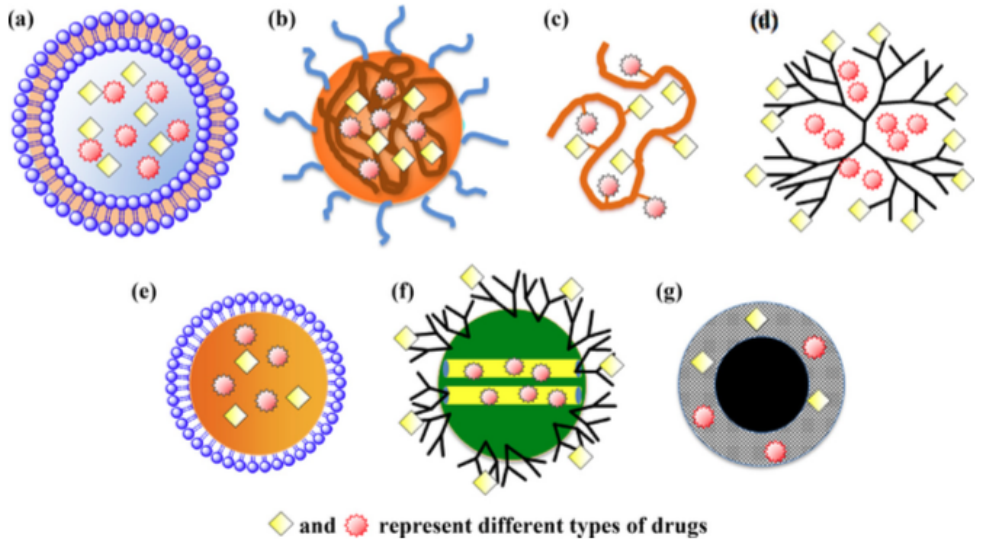

Figure 1: Schematic illustration of typical nanoparticles used in medical research. (a) liposome, (b) polymeric micelle, (c) polymer-drug conjugate, (d) dendrimer, (e) oil nanoemulsion, (f) mesoporous silica nanoparticle, and (g) iron oxide nanoparticle. Nanoparticles may be loaded with drugs and/or contrast agents. Illustration adapted from Hu & Zhang [19].

Nanoparticles utilised in medical research today vary greatly in composition, from mineral to lipid based entities. Some typical nanoparticles used are liposomes, solid lipid nanoparticles, nanoemulsions, dendrimers, polymeric nanoparticles, polymer-drug conjugates, and iron oxide nanoparticles [16, 19]. Despite differences in composition, most nanoparticles for medical applications have a similar design, as illustrated in figure 2. The nanoparticles usually have a core, a shell and a hydrophilic surface coating, where a payload of different drugs and/or imaging agents may be incorporated in either layer [6]. The design of a nanoparticle's surface is crucial for the particle's interaction with the body, and may be tailored for optimal performance. Shape, size, surface charge and surface composition may affect the circulation half-life and biodistribution of the nanoparticles. To achieve desired nanoparticle behaviour, surface coating with suitable molecules is therefore extensively utilised. One of the most common coating molecules, is the hydrophilic poly-ethylene glycol (PEG), which is shown to increase circulation half-life and improve biodistribution of nanoparticles. The exact mechanism behind this is not fully understood, but a widely accepted explanation is that PEG hinders opsonisation of nanoparticles, and thereby decrease their rate of elimination by the immune system [14, 16, 20, 21]. In addition to be surface coated, the particles may also be functionalised with targeting ligands or antibodies, directing them to bind to

and interact only with cells expressing specific surface molecules [14, 16]. This allows e.g. for targeted drug delivery and molecular imaging - two important achievements for improved cancer therapy and diagnostics.

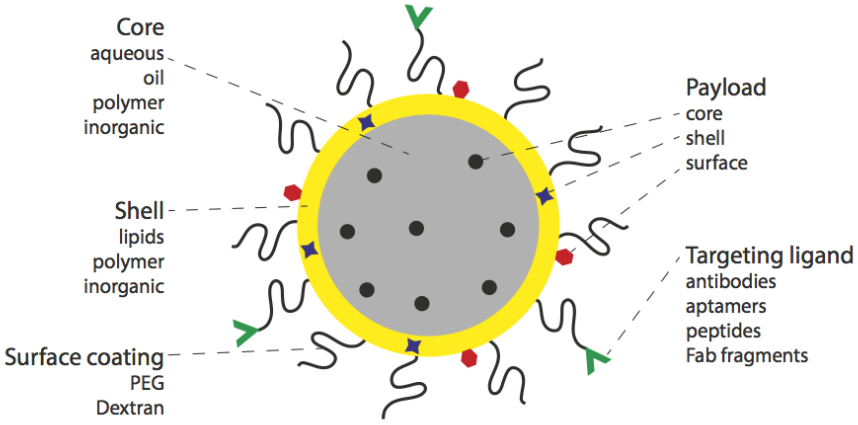

Figure 2: Schematic illustration showing a general design of nanoparticles used for *in vivo* applications. Illustration adapted from Hak [6].

A reason for the great interest in nanoparticles in medicine, is their beneficial size range. Their size give them preferable physicochemical and biological properties for biomedical applications, such as the ability to cross cell and tissue barriers. It is generally thought that nanoparticles with a hydrodynamic diameter of 10-100 nm have optimal pharmacokinetic properties for clinical applications. Renal clearance and extravasation into tissues are problematic with smaller nanoparticles, and larger nanoparticles are relatively quickly detected by the immune system and removed from the bloodstream by macrophages in the reticuloendothelial system [16].

2.2.1 Drug delivery

As mentioned earlier, encapsulation of drugs in a nanocarrier provides the possibility to design a custom-made controllable drug delivery system. To reduce the extent of dose-limiting side-effects and increase the efficacy of treatment, it is desirable that the drug is transported to, and only exerts its function, at the target site in the body. This may be possible to achieve by utilising nanocarriers [16]. It then requires the nanocarrier to hold and 'shield' the drug from the body until it reaches the desired site, and once there, release the therapeutic agent. By careful selection of nanoparticle composition, nanoparticles may be tailored to respond in a particular manner to different exogenous (e.g. ultrasound, temperature, magnetic field) and endogenous (e.g. pH, enzymatic activity, osmolarity) stimuli. Such functionalities, together with the use of targeting ligands, may be utilised both to direct nanoparticles to the target tissue and cells, and to induce controlled release of the therapeutic agent once there [16, 22, 23].

In addition to a controllable, site specific drug delivery system, drug encapsulation by nanocarriers offer several other advantages. An example of this is the possibility to deliver hydrophobic drugs [24] and larger biomolecules like peptides, DNA and RNA, to diseased tissue [25]. Another advantage is that several drugs may also be incorporated

in the same nanoparticle, allowing e.g. for improved combination therapy [14, 19]. Combination therapy is the use of multiple therapeutic agents in combination, and is an important strategy to treat drug resistant cancers. Encapsulation of the multiple therapeutic agents in nanoparticles, show potential for improved efficacy of this method [19].

2.2.2 Diagnostics

Nanoparticles may also be designed for usage in imaging, such as magnetic nanoparticles, quantum dots, and liposomes or dendrimers loaded with contrast agents. With the unique properties of nanoparticles, they may present several advantages compared to existing solutions, such as greater stability, longer circulation half-life and higher contrast. With the incorporation of targeting ligands, the nanoparticles may be directed towards detection of specific biomolecules of diagnostic value, and allow for non-invasive *in vivo* molecular imaging. By careful design of nanoparticles, they may greatly improve sensitivity, resolution and information content in *in vivo* imaging. Together, this may allow for an earlier detection of tumor development than currently available, and may even make biopsies taken for diagnostic purposes redundant [3, 4, 24].

Furthermore, real-time *in vivo* imaging may be used to monitor the therapeutic efficacy of administered drugs, both drugs of conventional and nanoparticle-based formats, and to guide effective surgery [3]. Molecular imaging may also allow selection of specific treatments for specific patients, and contribute to the development of personalised medicine for improved therapy [13].

The incorporation of several imaging agents in the same nanoparticle may allow for multimodal imaging with complementary imaging techniques. The major imaging modalitites currently available are typically characterised either by high sensitivity, but low spatial resolution, or high spatial resolution, but low sensitivity [26]. Combining complementary imaging techniques in one nanoparticle, may allow both macroscopic (to study the distribution and targeting on the whole body/organ level) and microscopic (to study interaction on the (sub)cellular level) imaging with the same nanoparticle. This is specifically helpful in understanding nanoparticle behaviour and hence, in development of nanoparticles for clinical usage [6].

2.2.3 Theranostics

In addition to carrying either therapeutic agents or contrast agents, nanoparticles may be made to carry *both* therapeutic and contrast agents simultaneously. Such nanoparticles are called 'theranostic' nanoparticles. Theranostic nanoparticles show potential in fields like non-invasive assessment of biodistribution and target site accumulation of drug-carrying nanoparticles, and visualisation of drug distribution and drug release at the target site. They also show potential for optimisation of strategies for triggered drug release, prediction and real-time monitoring of therapeutic responses, and development of the field of personalised medicine [27, 28].

2.3 Targeting nanoparticles to the tumor microenvironment

When targeting a specific disease, distinctive characteristics of the diseased tissue typically form the basis for targeting. For tumor tissue, there are several hallmarks which may be exploited to target nanoparticles specifically to this tissue. Tumors do, in fact, have a unique microenvironment which allows for both passive and active targeting of nanoparticles, and both have been widely studied [11, 17].

Passive targeting of nanoparticles to tumor tissue form the basis of current clinically available nanoparticle-based systems for drug delivery to solid tumors [29]. This targeting technique utilises a phenomenon called the enhanced permeability and retention (EPR) effect. This effect allows for accumulation of species of specific sizes in solid tumors, as illustrated in figure 3. The EPR effect is a result of an abnormally rapid growth of blood vessels, which is crucial to supply the rapidly growing tumor with oxygen and nutrients. The rapid growth leads to a chaotic tumor vasculature with several abnormalities, including disorganised and loosly connected endothelial cells and discontinuous or absent basement membrane [30]. This causes the blood vessels to be leaky. In fact, gap openings between endothelial cells in tumor tissue range from 20 nm to ~ 2 μm, while healthy vasculature has gap openings of <5 nm [31]. Hence, nanoparticles larger than ~ 5 nm may extravasate in tumor tissue, but not in healthy tissue. In addition to the leakiness causing enhanced permeability for nanoparticles, a dysfunctional lymphatic system in tumor tissue causes poor drainage, hence enhanced retention. These effects together allow for accumulation of nanoparticles with long circulation half-lives in tumor tissue, and hence selective drug delivery or imaging [31].

The EPR effect is an endogenous tumor characteristic which allows for selective tumor delivery simply by adjusting the size of the administered species. For this, most nanoparticles are suitable. Another method to achieve tumor-selective delivery, is to implement active components in the nanoparticle which 'perform' the targeting by reacting or binding to endogenous tumor features. One possibility is to create nanoparticles that are responsive to pH. The pH of the tumor microenvironment is $\sim$ 6.8, which is lower than in healthy tissue, and may therefore be exploited for targeting [32]. For example, Ling et al. [32] produced pH-sensitive nanoparticles which targets tumors by swithcing the surface charge from negative to positive when entering the acidic tumor microenvironment. This facilitated both tissue permeation and triggered cell internalisation of the nanoparticles, due to attractive electrostatic interactions between the nanoparticles and the negatively charged surrounding cells [10, 32]. Another possibility is to add specific targeting ligands to the nanoparticles, which bind to receptors or other biomolecules which are selectively expressed in cancer cells [11].

Active targeting may also be performed without only exploiting endogenous characteristics of the disease. This typically proceeds by applying an external stimuli to physically direct nanoparticles to move to or extravasate in a specific area. Examples of such stimulation are magnetic fields to direct the position of magnetic nanoparticles [33], and ultrasound to enhance extravasation and interstitial transport of nanoparticles in a specific area [34, 35, 36, 37, 38].

Although the EPR effect alone and in combination with active techniques has shown promising potential for selective delivery of nanoparticles to tumor tissue, a general

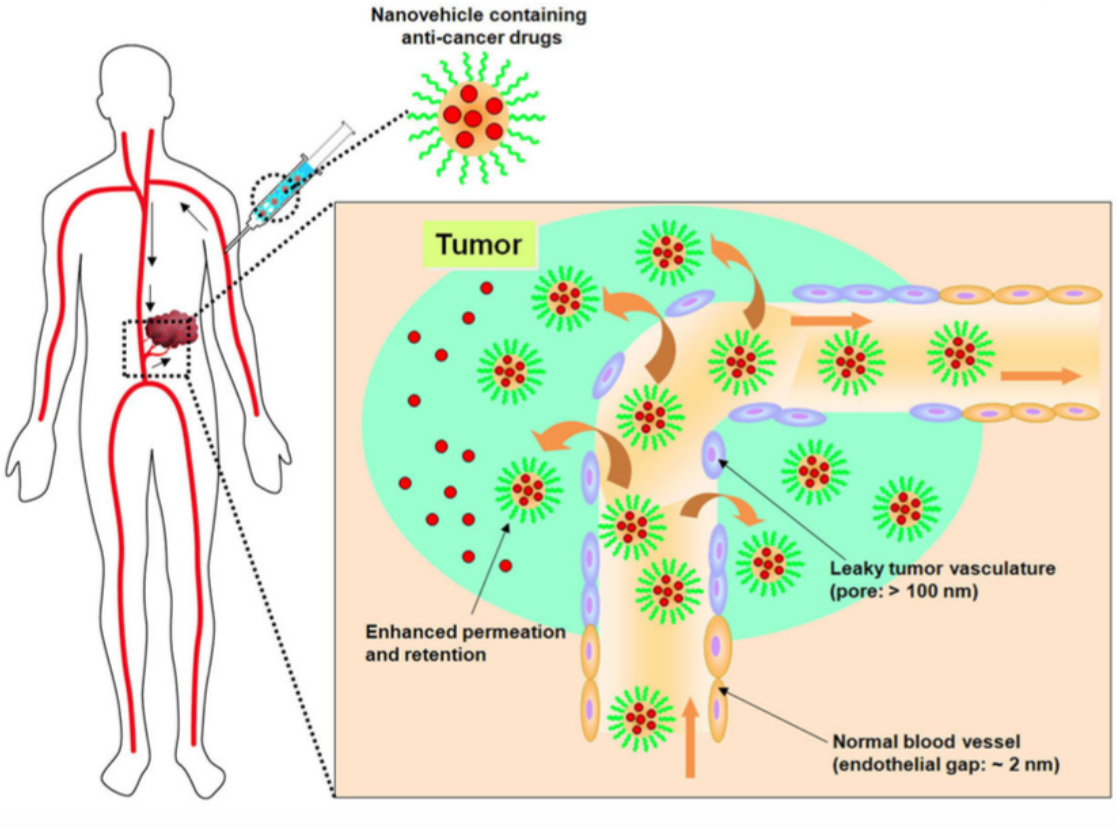

Figure 3: Schematic illustration of the enhanced permeability and retention effect observed for nanoscale species in solid tumors. Illustration adapted from Bae et al. [12].

problem is that a *uniform* delivery of nanoparticles to tumor tissue is very difficult to achieve [31]. Especially in cancer therapy, this is important to be able to kill all cancer cells. Several characteristics of the tumor microenvironment contribute to the non-uniform delivery, including an uneven distribution of blood vessels [39], an elevated tumor interstitial fluid pressure, and a dense and viscous extracellular matrix with accumulated solid stresses, slowing down transcapillary and interstitial transport of nanoparticles [40, 34].

As described above, there is extensive formation of new blood vessels in a growing tumor. Neovasculature differs from regular vasculature in several manners, e.g. in expression of certain surface receptors on constituting cells. Neovasculature may therefore be targeted specifically without affecting all existing vasculature. Hence, targeting neovasculature may represent a method to target cancer [41]. As the vasculature is necessary for tumor survival, one could easily imagine that affecting the vasculature could also significantly affect the tumor itself. A great advantage of targeting angiogenesis compared to targeting cancer cells themselves, is that the cells forming the blood vessels are readily available for agents carried by the blood stream [5]. Targeting angiogenesis therefore circumvents the difficulties of nanoparticle delivery that occurs due to the need for transcapillary and interstital transport of nanoparticles. In this manner, targeting angiogenesis represents an alternative and perhaps a more efficient method to target the tumor microenvironment, than to target cancer cells directly.

2.3.1 Targeting angiogenesis

Angiogenesis is a necessary contributor in a number of physiological processes, e.g. embryogenesis, tissue remodelling, the female reproductive cycle and wound healing. In addition, angiogenesis is upregulated in a number of pathological processes, such as rheumatoid arthritis, psoriasis, restenosis, diabetic retinopathy, and tumor growth and metastasis [7].

Some decades ago, it was a widely held belief that a shift in the equilibrium between tumor cell proliferation and apoptosis towards excess proliferation, was necessary and *sufficient* for the development of a large tumor that could kill its host [42]. Folkman et al. [43] was the first to suggest that tumor growth is angiogenesis-dependant. The reasoning was that for supplyment of oxygen and nutrients, tumors having a size larger than 1-2 mm^3 would indeed require angiogenesis [8]. Today, it is widely accepted that *both* tumor cell proliferation and angiogenesis together are necessary and sufficient to generate a detectable tumor mass. An increasing body of evidence suggest that tumor cell proliferation alone, in the absence of angiogenesis, can only give rise to dormant, microscopic tumors of ~ 1 mm^3 or less, and that these cancers are harmless to the host [42]. This suggests that blockage of angiogenic activity has great potential in cancer therapy.

After the theory of angiogenesis' importance for cancer progression was presented, the field of anti-angiogenic therapy has evolved and angiogenesis inhibitors for the treatment of cancer have been approved by the Food and Drug Administration (FDA) in the United States. The first angiogenesis inhibitor approved by the FDA was Avastin for the treatment of colorectal cancer. Avastin is an antibody against vascular endothelial growth factor (VEGF), which causes upregulation of angiogenic activity [42].

The process of tumor angiogenesis is highly complex, and is controlled by numerous signalling events between endothelial cells, cancer cells, soluble factors and extracellular matrix components. In 2006, Folkman et al. [42] reported that there were in total 27 endogenous angiogenesis inhibitors identified in the circulation and tissue, which act as tumor suppressors under physiological conditions. There are likely as many angiogenesis inducers, together indicating that many signalling pathways have potential for exploitation in anti-angiogenic therapy. The relevant regulatory pathways may also be affected at different levels - thereby different classes of angiogenesis inhibitors exist, e.g. growth factor blockers, inhibitors of growth factor signalling, modulators of extracellular matrix and direct inhibitors of endothelial cell proliferation and migration [5].

An important class of molecules investigated for anti-angiogenic therapy, is cell surface receptors with upregulated or selective surface expression in angiogenic endothelial cells. In addition to serve as targets for anti-angiogenic therapy, such receptors may also serve as diagnostic markers for angiogenesis [6, 7, 5, 8]. Detection of angiogenesis imply detection of a potential tumor, and could represent a novel non-invasive tool for detecting tumors at an early stage. One important endothelial cell surface receptor in tumor angiogensis, is the $\alpha_v\beta_3$-integrin. This receptor is known as the vitronectin receptor, and is selectively overexpressed on the surface of endothelial cells of growing blood vessels [41]. The $\alpha_v\beta_3$-integrin has been extensively studied and shows great

potential both for anti-angiogenic therapy and diagnostic purposes [6, 7, 5, 8].

2.4 $\alpha_v\beta_3$-integrin

Integrins are a family of heterodimeric transmembrane receptors binding to various extracellular matrix (ECM) components, including collagens, laminins, fibronectin and vitronectin. Intracellularly, integrins binds to the actin cytoskeleton and thereby connect the inside and outside of the cell. Integrins consist of one α and one β subunit (Figure 4). Until now, 18 α and 8 β subunits have been identified, forming together 24 distinct heterodimers which bind different ligands. Members of the integrin family are expressed in a cell- and tissue-specific manner and contribute in the control of various cellular processes such as proliferation, apoptosis, differentiation and cell migration. Integrins therefore play key roles in development, immune responses and the progression of diseases like cancer [7, 44].

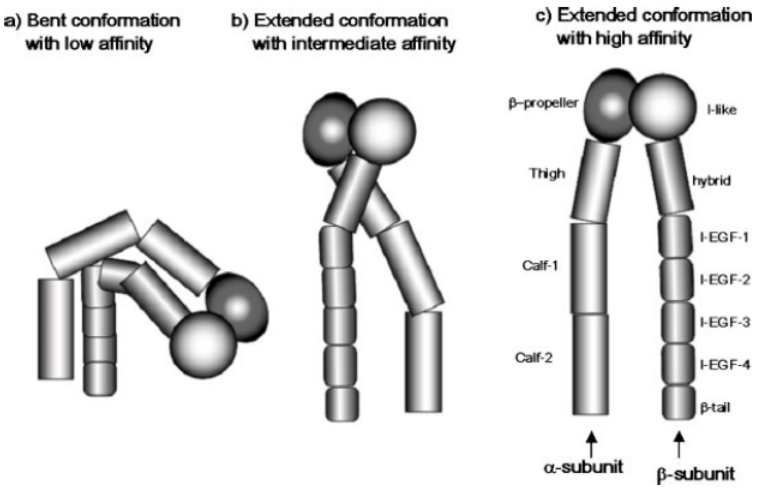

Figure 4: Schematic illustration showing the general structure of integrins. The different segments of the α- and β-subunits are illustrated based on the structure of $\alpha_v\beta_3$. There are three possible conformations of integrins: (a) a bent conformation with a low affinity for the ligand, (b) an extended conformation with intermediate ligand affinity and closed headpiece, and (c) a high ligand affinity conformation with an extended conformation that has open headpiece when bound to RGD peptide. Illustration and figure legend adapted from Dunehoo et al. [45].

In cancer progression, integrins are specifically important for angiogenesis, as they are necessary for mediating migration of endothelial cells into the basement membrane, as well as regulating endothelial cell growth, survival and differentiation during angiogenesis [7]. As mentioned, $\alpha_v\beta_3$-integrin is selectively overexpressed on angiogenic endothelial cells, and play key roles in these processes [41]. In addition, some types of cancer cells also express $\alpha_v\beta_3$-integrin (e.g. melanoma, glioblastoma, ovarian, and breast cancer cells) [8, 7]. For these cancer cells, $\alpha_v\beta_3$-integrin typically promotes several cellular functions like invasion, migration and cell survival, necessary for tumor growth and metastasis [46].

For exploiting the receptor $\alpha_v\beta_3$-integrin to perform anti-angiogenic therapy and molecular imaging, the peptide sequence RGD has been utilised as a targeting ligand for decades. This peptide sequence has been identified as an essential binding motif for 7 out of the 24 integrin receptors, including $\alpha_v\beta_3$-integrin [7]. After this discovery was made, many groups have worked with designing high affinity and selective ligands for $\alpha_v\beta_3$-integrin containing the RGD sequence [7, 41]. RGD-containing peptides that bind selectively to only one or a few of the RGD-binding integrins, may be designed by restricting the conformation of the RGD sequence to fit with the binding site on the relevant integrin. To achieve this, many researchers have designed a variety of cyclic RGD peptides that provide the necessary secondary structure at the RGD sequence to bind specifically to $\alpha_v\beta_3$-integrin, or they have synthesised suitable RGD mimics [47, 45].

The most successful monovalent ligand for $\alpha_v\beta_3$ developed so far, is the cyclic pentapeptide *cyclo*[-RGDf(*N*Me)V-], known as Cilengitide and developed by Merck KGa [41]. Cyclic pentapeptides containing the RGD sequence have been shown to inhibit angiogensis, induce endothelial cell apoptosis, decrease tumor growth, and reduce invasiveness and spread of metastasis [7]. However, Cilengitide, which managed to enter phase III clinical trials for the treatment of glioblastoma, did not lead to clinical success. There may be several reasons for this, but one possible cause of clinical failure for such agents, may lie in poor knowledge of the molecular mechanisms behind receptor functioning and the effect of receptor-ligand interactions [6]. Silva et al. [48] suggest that a possible explanation of the lack of general success of the $\alpha_v\beta_3$-integrin drugs in clinical trials, may lie in the dose administered and the pharmacokinetics of the drugs. In general, clinical trials of such drugs involve periodic bolus injections and the plasma concentration of the drugs drop significantly between injections. Silva et al. present that several studies have shown that low doses of drugs can have agonistic effects. For example, Legler et al. [49] showed that low doses of an RGD-peptide actually enhanced the adhesive function of $\alpha_v\beta_3$ to its ECM ligand vitronectin, instead of acting as an antagonist to block binding between the two. Understanding how this might occur, how high and low doses of the same agent may induce opposite effects, is crucial to develop safe and more effective therapeutic strategies [48].

In addition to utilising free cyclic RGD-peptides as antagonists of the receptor $\alpha_v\beta_3$-integrin to inhibit angiogenesis, the RGD peptide may be used in both cancer therapy and imaging by conjugation to nanoparticles or other species. The RGD peptide may be conjugated to e.g. anti-cancer agents, contrast agents, and nanoparticles carrying anti-cancer and/or contrast agents. By this, the RGD peptide may direct association between these agents and cells expressing the $\alpha_v\beta_3$-integrin [8]. This may be used both to kill angiogenic endothelial cells and to detect areas of angiogenesis by *in vivo* molecular imaging.

2.4.1 $\alpha_v\beta_3$-integrin is a recycling receptor

An important notice when targeting $\alpha_v\beta_3$-integrins for medical applications, is that integrins are recycling receptors. The fact that integrins undergo an exocytic-endocytic cycle, and that the control of integrin availability at the plasma membrane is key to integrin function, has been known for over 20 years. However, the details of inte-

grin cycling pathways has only been studied recently. Integrins have been shown to internalise through the major endocytic routes macropinocytosis, clathrin-dependant endocytosis and clathrin-independant endocytosis. Integrin endocytosis may either be constitutive or promoted by specific interactions [44]. Promotion of integrin endocytosis has been studied extensively for viral entry, as several viruses utilise integrins to internalise in host cells [50, 51, 52, 53], but also cell adhesion to ECM components has been found to promote integrin endocytosis [44].

An illustration of $\alpha_v\beta_3$-integrin recycling is presented in figure 5. Once integrins have internalised, they are rapidly trafficked to early endosomes (EEs) that are distributed in the peripheral cytoplasm [44, 54]. In EEs, integrins are sorted for degradation or recycling. For degradation, integrins are transported to mulitvesicular bodies and late endosomes. For recycling, $\alpha_v\beta_3$-integrins have been shown to either recycle through a 'short-loop' or 'long-loop' recycling pathway. $\alpha_v\beta_3$-integrins for 'short-loop' recycling are sorted to certain subdomains of EEs and rapidly returned to the plasma membrane through a Rab4-dependant mechanism. $\alpha_v\beta_3$-integrins for 'long-loop' recycling are transported to the perinuclear recycling compartment (PNRC), and return to the plasma membrane via a Rab11-dependant mechanism. The half-lives of $\alpha_v\beta_3$ recycling through the 'short-loop' and 'long-loop' pathways, are reported to be 3 min and 10 min, respectively [44, 54].

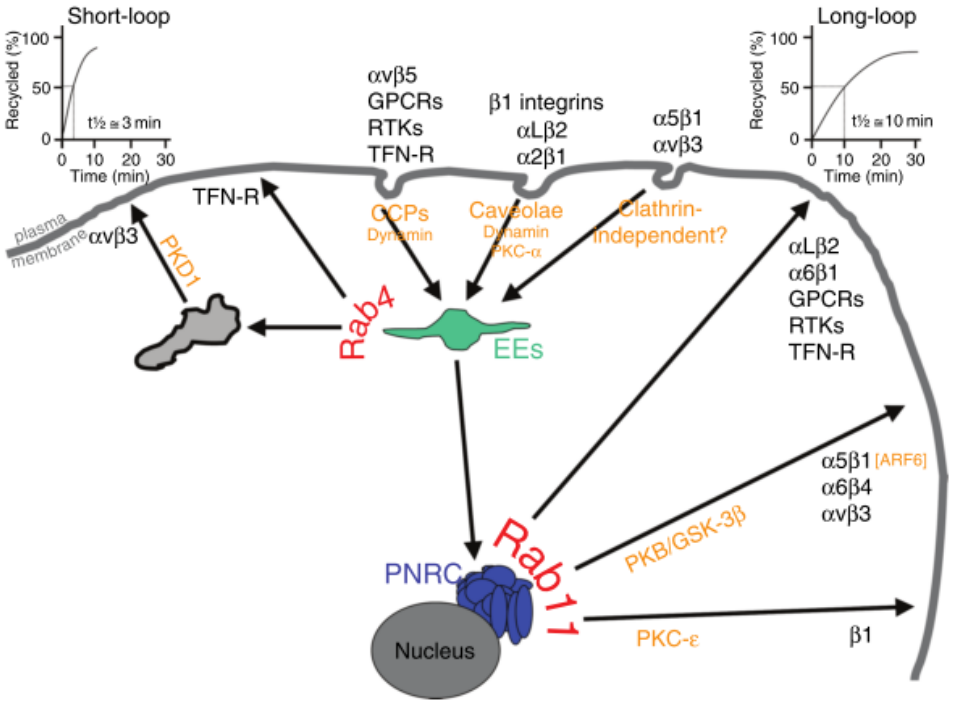

Figure 5: Schematic illustration of the Rab GTPase and kinase control of integrin trafficking. The trafficking of multiple integrins and the receptors transferrin receptor (TFN-R), G-protein coupled receptors (GPCRs) and receptor tyrosine kinases (RTKs), are presented. $\alpha_v\beta_3$-integrins are transported to early endosomes (EEs) upon internalisation. Followingly, $\alpha_v\beta_3$ may either recycle via the Rab11-dependant 'long-loop' pathway through the perinuclear recycling compartment (PNRC), or via the Rab4-dependant 'short-loop' pathway without passing the PNRC. The cartoon graphs in the top left- and right-hand corners, respectively, denote the kinetics of recycling via the short and long loops. Illustration and figure legend adapted from Caswell & Norman [54].

2.4.2 Consequences of receptor recycling for targeting kinetics

As presented in the introduction of this thesis, targeting of $\alpha_v\beta_3$-integrin has been studied for decades, while little focus has been placed on the fact that $\alpha_v\beta_3$ is a recycling receptor. One of the few papers adressing this, was published by Hak et al. [9] in 2013. Here, a periodicity in the accumulation of RGD-conjugated nanoemulsions (NE) was observed, which was not present for non-targeted control NE. This *in vivo* periodicity is presented in figure 6, together with an hypothesis proposed by Hak et al. on how receptor recycling may be a cause of these targeting kinetics.

Hak et al. propose that the *in vivo* observations are caused by $\alpha_v\beta_3$-integrin binding, internalisation and recycling kinetics. They propose that the bolus injection of RGD-NE will cause the majority of $\alpha_v\beta_3$-integrins to be bound and internalised within minutes upon injection. Further, they propose that the majority of these integrins will also recycle and reappear at the cell surface at a similar time point. Together, this may explain the periodicity observed; After binding of the first pool of RGD-NE,

$\alpha_v\beta_3$-integrin is unavailable for circulating RGD-NE, hence NE accumulation level off. When the pool of recycled $\alpha_v\beta_3$ return to the plasma membrane, new binding and internalisation may occur, hence NE accumulation increase.

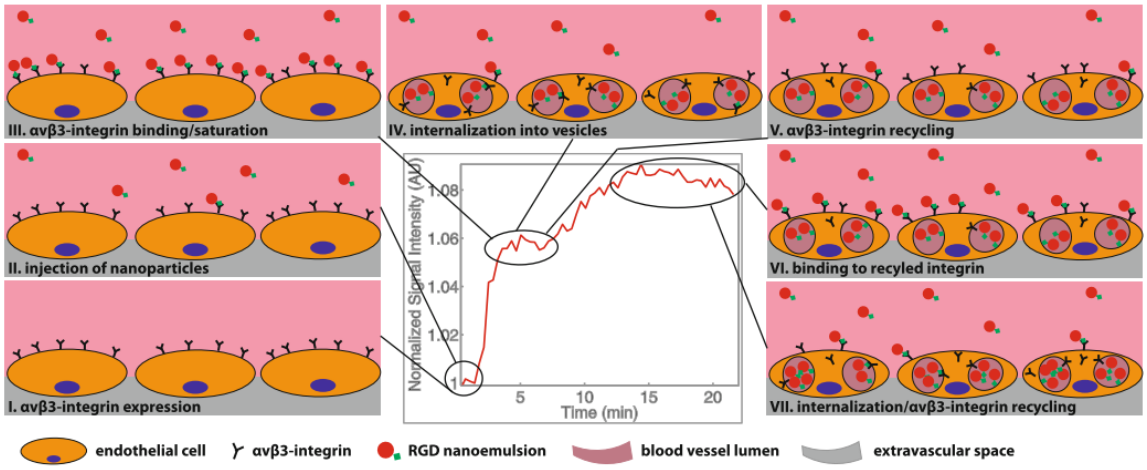

Figure 6: Graphical representation of the hypothesized chronological events leading to the observed periodicity in *in vivo* experiments. (The seven illustrations are numbered I - VII in the lower left corner.) **I, II** Show the situation before and just after injection of NE. **III** Depicts the binding/saturation which leads to the first signal increase. **IV** Shows the internalization during the first interval where no signal increase is observed and **V** shows the recycling of integrin back to the cell membrane which is occurring towards the end of the first interval with constant signal intensity. **VI** Shows the binding which has occurred after the second signal increase and **VII** shows internalisation/recycling occurring again towards the end of the measurement. Illustration and figure legend adapted from Hak et al. [9].

2.4.3 Receptor change due to ligand binding affects targeting efficiency

The cyclic RGD-containing pentapeptides described previously (like Cilengitide), are monovalent RGD ligands. However, it is known that a wide diversity of natural processes involve multivalent interactions between ligands and receptors. Multivalency has in many cases been shown to increase the binding strength of ligands to their receptors, and to promote receptor-mediated internalisation of the bound species [41]. Therefore, a number of species presenting multiple RGD peptide sequences, have also been developed to target $\alpha_v\beta_3$-integrin [41]. Some examples of this will be presented after a closer description of why multivalency may have an impact on targeting efficiency.

It has been shown that as a ligand binds to its receptor, this interaction may trigger receptor changes. Such changes may for example be changes in receptor conformation and redistribution of receptors in the cell membrane. A common response to ligand binding is receptor clustering. Receptor clustering has been shown to happen for multiple types of receptors, including integrins. As the receptors cluster in the cell membrane, the distance between the receptors significantly decreases. For nanocarriers coated with RGD peptides, the clustering of receptors may have important implications

for how the RGD peptide should be presented to most efficiently target $\alpha_v\beta_3$-integrins [55].

Interestingly, several adenovirus serotypes have evolved to utilise clustered RGD ligands to gain access into cells by binding multiple integrin receptors simultaneously [56]. An example of this is Adenovirus 2 (Ad2), where each of the twelve vertices of the virus surface contains a penton base. This penton base consist of five identical subunits, which each contain an RGD peptide sequence [56, 50] (Figure 7). The RGD peptide sequences in the penton base are located 5.7 nm apart from eachother [56]. For Ad2, it is shown that the virus attaches to the cell surface through binding of its fiber protein to the receptor CAR, with a 30-fold higher affinity than the binding of RGD to $\alpha_v\beta_3$-integrin [51, 50]. The penton base presenting the RGD peptides is, however, critical for viral entry into the cell [56]. The engagement of integrins by the penton base induces signals, including activation of PI3 kinase, $p130^{CAS}$, and Rho GTPases, that are important for rearrangements in the actin cytoskeleton and initiation of virus internalisation [51].

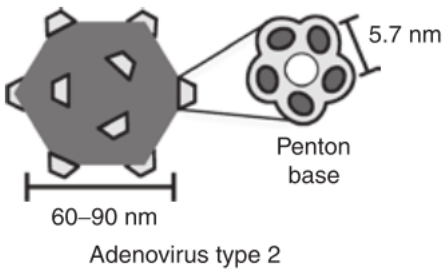

Figure 7: Schematic illustration of Adenovirus type 2, with a penton base containing five RGD peptide sequences on each of the twelve vertices of the virus surface. The distance between RGD peptide sequences in the penton base in ~ 5.7 nm. Illustration adapted from Ng et al. [56].

Examples of studies with multivalent RGD ligands

Several researchers have investigated the effect of multivalency on the interaction between RGD and $\alpha_v\beta_3$-integrins. One example of this is the tetrameric RGD structure named RAFT(c[-RGDfK-])$_4$ [41]. This structure was developed by Boturyn et al. [57], and an illustration is presented in figure 8. The molecule contains four copies of the c[-RGDfK-] monomer bound to a cyclic decapeptide scaffold (RAFT, Regioselectively Adressable Functionalised Template). By exchanging n of the four c[-RGDfK-] monomers with c[-RβADfK-] (which does not bind to $\alpha_v\beta_3$-integrin), in addition to making an array of four RAFT(c[-RGDfK-])$_4$, the binding affinity of ligands displaying 1, 2, 3, 4 and 16 c[-RGDfK-] was compared. The best binding affinity was found for ligands displaying three or four copies of the c[-RGDfK-] peptide [41].

It has also been found that for the RAFT(c[-RGDfK-])$_4$, cellular uptake *in vitro* happens through receptor-mediated endocytosis. The monovalent c[-RGDfK-] peptide, however, has been shown to internalise through an independant fluid phase endocytosis pathway [41]. The RAFT(c[-RGDfK-])$_4$ has also been shown to inhibit lateral mobility

of $\alpha_v\beta_3$-integrin in HEK293(β_3) *in vitro*, probably due to the formation of integrin clusters upon binding. This was not observed for c[-RGDfK-] or RAFT(c[-RβADfK-])$_4$. Also exposure to 1 μmol/l RAFT(c[-RGDfK-])$_4$, was shown to induce increased $\alpha_v\beta_3$ internalisation, while the monovalent c[-RGDfK-] did not affect $\alpha_v\beta_3$ internalisation compared to control [58].

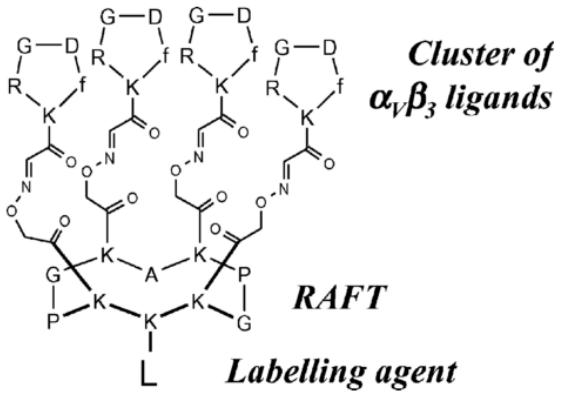

Figure 8: Schematic illustration showing the chemical stucture of the tetravalent RGD ligand RAFT(c[-RGDfK-])$_4$. Here, the structure is conjugated to a labelling agent, but it may also be conjugated to different species, e.g. to nanoparticles. Illustration adapted from Garanger et al. [41].

Guo et al. [55] investigated the effect of multivalency with emphasised focus on the effect of ligand intervals on targeting efficiency. They designed and constructed three RGD-modified nanocarriers with different ligand intervals; stealth liposomes conjugated to monomeric RGD (moRGD-LP), dimeric RGD (diRGD-LP) and a special dimeric RGD with a linker between two cyclic RGD motifs (P-diRGD-LP) (Figure 9). In their studies, Guo et al. performed both experimental studies and calculations. From 3D models of $\alpha_v\beta_3$ clustering, they calculated a receptor distance of 41.916 - 65.779 Å in clusters of $\alpha_v\beta_3$-integrins. Molecular computation simultaneously showed that the RGD ligand distance for diRGD-LP, P-diRGD-LP and moRGD-LP was 20.944 Å, 42.753 Å and 78.196 Å, respectively (see figure 9). This indicates that, if the calculations are correct, the distance between RGD ligands in P-diRGD-LP matches the distance between clustered $\alpha_v\beta_3$-integrins the best, and P-diRGD-LP may bind several clustered $\alpha_v\beta_3$-integrins simultaneously. From experimental studies, Guo et al. found that P-diRGD-LP did in fact show the strongest interaction with $\alpha_v\beta_3$ positive tumor cells (Melanoma B16) and the highest cellular uptake. The enhanced endocytosis of P-diRGD-LP was shown to be $\alpha_v\beta_3$-dependant, and P-diRGD-LP was shown to increase the involvement of the clathrin-mediated endocytosis pathway. Both *in vivo* and *ex vivo*, P-diRGD-LP showed the best targeting effect in B16-tumor bearing mice, about 2.4-fold better than moRGD-LP and 2.8-fold better than diRGD-LP at 3h.

Together, these studies indicate that the presentation of RGD ligands, has a strong impact on the interaction with $\alpha_v\beta_3$-integrin expressing cells. Both valency and ligand intervals seem to have an effect both on binding affinity, extent of cellular uptake, cellular uptake pathway (receptor-mediated endocytosis, or receptor-independant endocytosis), and whether binding of the RGD ligand induces $\alpha_v\beta_3$ internalisation. It

becomes evident that the interplay between RGD ligands and $\alpha_v\beta_3$-integrin is not a simple process, but a highly dynamic process which is most likely influenced by a large number of factors.

Integrin conformation and bidirectional signalling

As a binder of ECM proteins and intracellular actin filaments, integrins participate in both inside-out and outside-in signalling. As illustrated in figure 4, integrins may namely adopt both a non-activated and an activated (intermediate and highly activated) state. The non-activated state has low affinity and the activated state has high affinity for ligand binding. Integrins thereby mainly bind to their ligands in the intermediate activated or highly activated state. Due to the switching between conformations, integrins are able to signal bidirectionally across the cell membrane. Ligand binding induces intracellular signalling processes (outside-in signalling), while intracellular proteins may bind to integrins causing integrin activation, and promote ligand-binding (inside-out signalling). The bidirectional signalling may also participate in a positive feedback loop. For example, when ECM proteins bind their integrin receptors, activated integrins typically form clusters in the cell membrane that are associated with a cytoskeletal complex to promote actin filament assembly. As a positive feedback, the actin filament reorganisation further increases integrin clustering followed by enhanced binding of ECM ligands [45, 44].

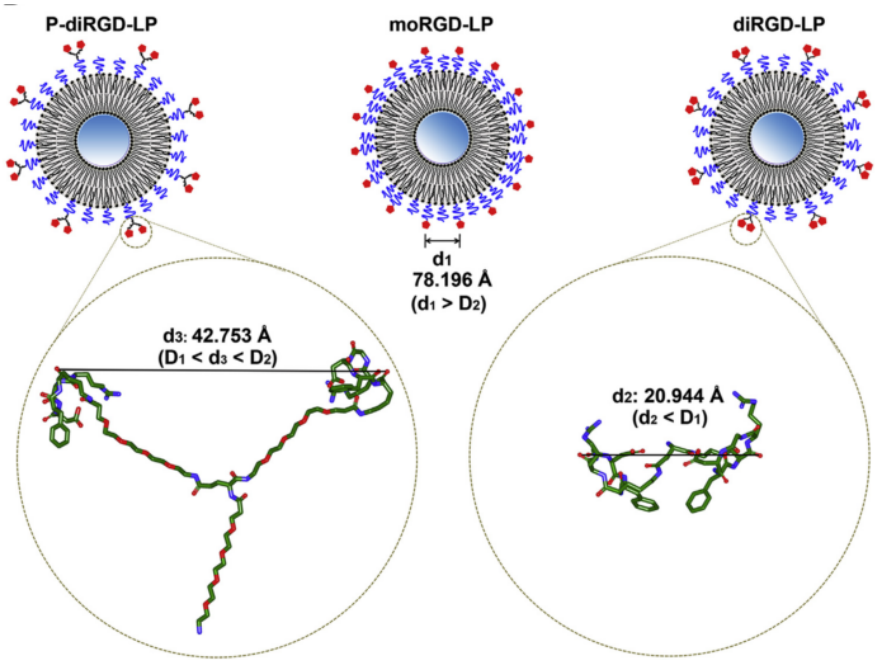

(a) Schematic representations of the RGD interval of the three different RGD-modified liposomes moRGD-LP, diRGD-LP and P-diRGD-LP. The calculated distances between two RGD peptide sequences are written next to each RGD-modified liposome.

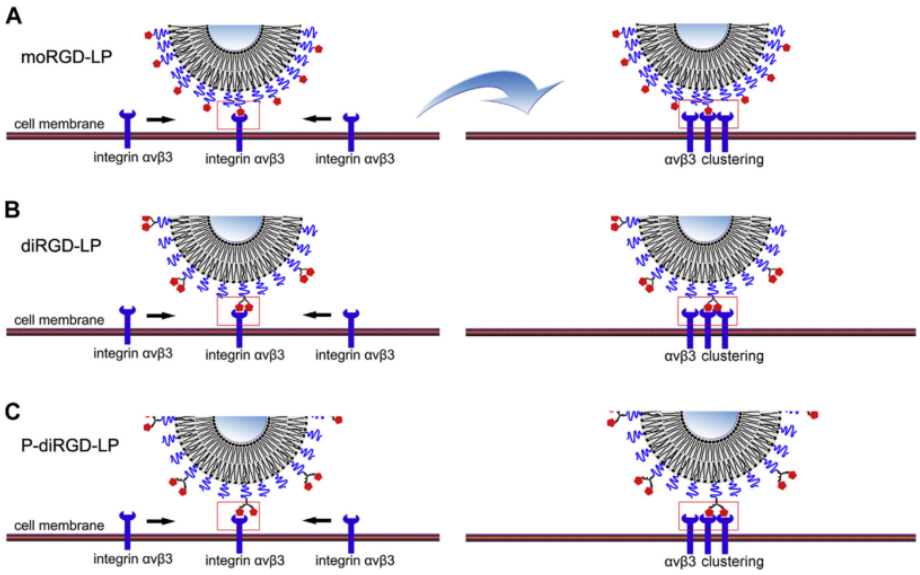

(b) Schematic illustration of the interactions between different RGD-modified nanocarriers with adjacent binding sites in $\alpha_v\beta_3$ clustering. (A) For moRGD-LP, the two RGD molecules on the surface of liposomes were too far to bind two $\alpha_v\beta_3$ molecules simultaneously. (B) For diRGD-LP, the distance between the two RGD motifs was much shorter than the distance between the two $\alpha_v\beta_3$ binding sites in the case of $\alpha_v\beta_3$ clustering. (C) The distance between the two RGD motifs of P-diRGD-LP was just compatible for simultaneous binding of two integrin $\alpha_v\beta_3$ molecules in the case of $\alpha_v\beta_3$ clustering.

Figure 9: Illustrations and figure legends adapted from Guo et al. [55], presenting schematic illustrations of their findings on the effect of ligand intervals on targeting efficiency of RGD-modified nanocarriers.

Summary
From the information given in this section, it seems like $\alpha_v\beta_3$-integrin function may be affected by numerous known and unknown factors. For example, all of integrin occupancy, conformation and clustering seem to regulate integrin signal transduction [56]. As mentioned previously, the concentration of RGD ligands also seem to have an effect on integrin signalling [48]. In addition, crosstalk with other receptors is also highly likely to occur [48]. To successfully and safely utilise targeting of the $\alpha_v\beta_3$-integrin in anti-angiogenic therapy and for molecular imaging, it is crucial to obtain a better understanding of the mechansims by which different presentations of RGD ligands affect integrin function [48].

To summarise what was presented here, and what we may infer about integrin function during interaction with different RGD ligands, it may seem like:
Activation of $\alpha_v\beta_3$-integrins by binding of RGD ligands, causes clustering of $\alpha_v\beta_3$. Further, it seems like species which present multiple RGD peptides in the correct interval to match the distance between clustered $\alpha_v\beta_3$-integrins, show a higher binding affinity than monovalent RGD peptides. This is most likely because they may bind several clustered $\alpha_v\beta_3$-integrins simultaneously. These species also seem to be more efficiently taken up into the $\alpha_v\beta_3$-expressing cells, than species with monovalent RGD presentation. This is in compliance with the fact that the penton base of Adenovirus 2 with five RGD peptides in distance 57 Å (5.7 nm) apart, and the P-diRGD-LP with two RGD peptides calculated to be 42.753 Å apart, are both effectively internalised in $\alpha_v\beta_3$-expressing cells and they both perfectly match the calculated distance between clustered $\alpha_v\beta_3$-integrins (41.916 - 65.779 Å). It may also seem like species able to bind several clustered $\alpha_v\beta_3$-integrins simultaneously, are taken up through $\alpha_v\beta_3$-dependant endocytosis pathways, while monovalent RGD is taken up through endocytosis pathways independant of $\alpha_v\beta_3$-integrin. From the information presented about RAFT(c[-RGDfK-])$_4$ and the Adenovirus 2 penton base, it may also seem like species able to bind multiple clustered $\alpha_v\beta_3$-integrins simultaneously, manage to induce increased internalisation of $\alpha_v\beta_3$-integrin, while monovalent RGD does not.

2.5 Oil-in-water nanoemulsion - a lipid-based nanoparticle

A group of nanoparticles extensively studied for medical applications, is lipid-based nanoparticles (Figure 10). These are all primarily composed of amphiphilic lipids (see below), and include particles like micelles, liposomes and nanoemulsions. Lipid-based nanoparticles are self-assembled structures, formed due to the nature of the amphiphiles combined with properties of the solvent(s). This allows easy preparation, as well as easy incorporation of different functionalities in the nanoparticles. It is also relatively straight forward to incorporate *multiple* functionalities in the same nanoparticle. Lipids utilised in lipid-based nanoparticles are usually phospholipids, cholesterol and synthetic lipids closely related to these. Phospholipids and cholesterol are important constituents of biological membranes, and lipid-based nanoparticles are therefore generally considered biocompatible. Other types of nanoparticles, e.g. inorganic and polymeric nanoparticles, may also be coated with lipid layers to enhance biocompatibility and to ease incorporation of several functionalities [24].

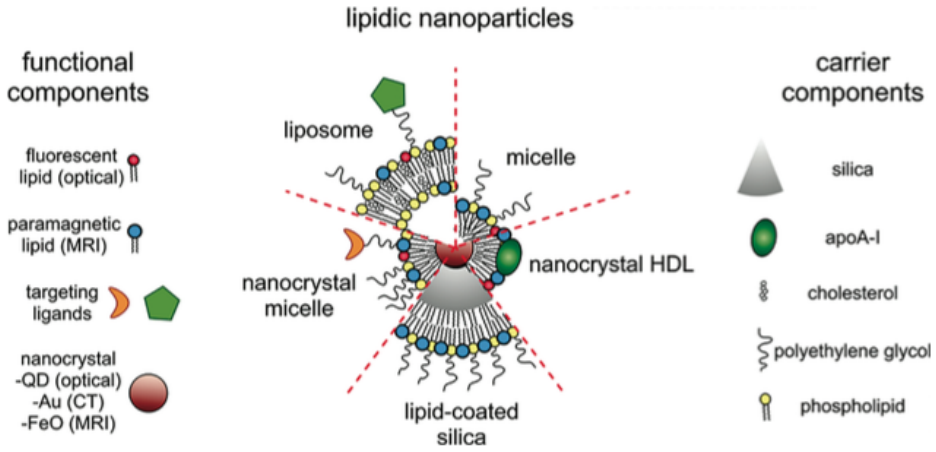

Figure 10: An illustration showing examples of lipid-based nanoparticles. It is here demonstrated how lipid-based nanoparticles may be functionalised with several imaging agents simultaneously, creating so-called multimodal imaging agents. Surface coating with polyethylene glycol (PEG) and targeting ligands are also illustrated. In addition to this, lipid-based nanoparticles may be loaded with different drugs. Multifunctional nanoparticles are made when loading nanoparticles with both imaging agents and drugs, simultaneously. Illustration adapted from Mulder et al. [59].

2.5.1 Amphiphiles

Amphiphilic molecules are molecules with both hydrophobic and hydrophilic domains. At very low concentrations in aqueous solutions, amphiphiles are present as single molecules. However, contact between hydrophobic molecules and water is entropically unfavourable due to restricted mobility of water molecules in the contact area. At concentrations above a critical value, amphiphiles therefore start forming aggregates where the hydrophobic domains cluster together, and are separated from the water solution by the hydrophilic domains of the same molecules. The hydrophilic domains are able to form hydrogen bonds with the surrounding water molecules, hence achieving a more entropically favourable situation as the mobility of water molecules is less restricted [24].

There is a large variation in the structures of the hydrophobic and hydrophilic domains of amphiphiles, as illustrated in figure 11. Depending on the length and size of the hydrophobic domain, the size and charge of the hydrophilic domain, pH, temperature and concentration, amphiphiles may self-assemble into different structures. It is difficult to predict the specific structure formed under different conditions, but in a low concentration regime, structures like liposomes and micelles are most common. Typically, amphihiles with large hydrophilic and small hydrophobic domains, tend to form micelles (upper right portion of figure 10) because relatively large curvatures are formed upon membrane formation. When the volume of the hydrophobic domain increases relative to the surface area of the hydrophilic domain, liposomes (bilayer structures) are the most likely structures formed. A unilamellar liposome is illustrated in the upper left portion of figure 10. Bilayer structures are typically formed by phos-

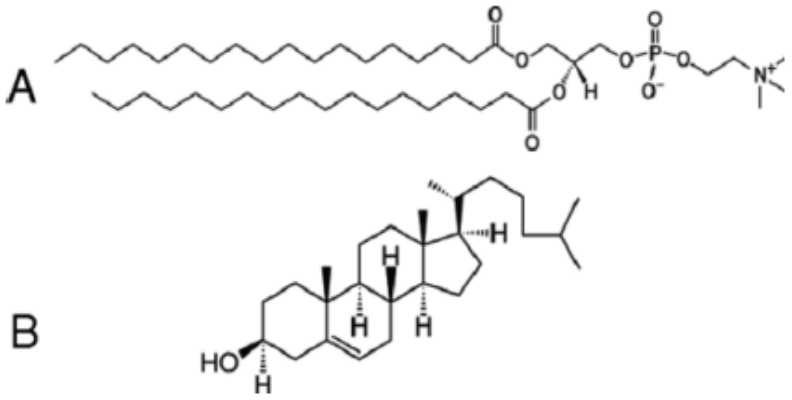

Figure 11: An illustration of two commonly used amphiphiles in lipid-based nanoparticles. A) The phospholipid distearoylphosphatidylcholine (DSPC) contains two fatty acyl chains in the hydrophobic domain, while the hydrophilic part is composed of the phosphate moiety with the surrounding nitrogen and oxygen atoms. B) In cholesterol, the hydrophobic part is represented by the hydrocarbon ring structures, while the hydrophilic part solely consists of the hydroxyl group. Illustration and figure legend adapted from Hak et al. [24].

pholipids with two hydrocarbon chains making up the hydrophobic domain, as seen in figure 11A [24].

Lipid-based nanoparticles with desired structure and characteristics may be achieved by mixing different amphiphiles, and optimise their ratios. This will affect the type of self-assembled structure, and may also affect the stability of different structures. The addition of cholesterol to lipid bilayers, will for example decrease the curvature of the bilayer and stabilise the structure [24].

2.5.2 The first lipid-based nanoparticles - liposomes

Liposomes are defined as spherical, self-closed structures of one or several lipid bilayers with an aqueous phase inside and in between the bilayer membranes [60]. Unilamellar liposomes typically have a diameter of 50 - 800 nm, and are the most studied lipid-based nanoparticles for *in vivo* applications [6]. The first FDA-approved nanoparticle-based drug delivery system was, in fact, Doxil® - liposomes loaded with the anti-cancer agent doxorubicin [61]. After the FDA-approval of Doxil® in 1995, liposomes have been studied extensively. Liposomes have been studied for the usage in both therapy, diagnostics, and the combination of the two, theranostics, and have proven highly suitable for many applications [6, 61]. Due to the similar nature of different lipid-based nanoparticles, lessons learned from the study of liposomes may in many cases be utilised quite directly in the study of other lipid-based nanoparticles.

2.5.3 Nanoemulsions

Liposomes and micelles are structures formed by amphiphiles in a pure aqueous phase. By exchanging the pure aqueous phase with both a hydrophilic and a hydrophobic

phase, e.g. water and oil, the addition of amphiphiles will generate emulsion droplets. An emulsion may either be oil-in-water or water-in-oil. Oil-in-water emulsions consist of small oil droplets in water (and vice versa for water-in-oil) stabilised by a single layer of amphiphiles. The amphiphiles then have their hydrophobic domain embedded in the oil and the hydrophilic domain facing the water, reducing the total free energy of the system [6].

Nanoemulsions are typically produced simply by mixing all components (amphiphiles, oil, water/buffer) to obtain a crude emulsion. Once a crude emulsion is made, nanoemulsions (emulsion droplets at the nanometer scale) may be formed by exposing the solution to specific stresses, e.g. by ultrasonication. From this, stable nanoemulsions with narrow size distributions may be formed, with the size depending on the oil-to-amphiphile ratio [6]. Oil-in-water nanoemulsions (Figure 12), where the continuous phase is aqueous, are suitable for medical applications and benefit from the same advantageous properties as other lipid-based nanoparticles. In addition, nanoemulsions offer the possibility to carry a high load of hydrophobic molecules, both hydrophobic drugs and contrast agents [6, 24].

Oil-in-water nanoemulsions utilised in medical research today are typically in the size range of 30 - 500 nm. Amphiphiles commonly utilised in nanoemulsions are phosphatidyl-choline, cholesterol and PEGylated phosphatidyl-ethanolamine (PEG-PE). Phosphatidyl-choline is widely used and known to form relatively stable oil-in-water nanoemulsions. Cholesterol further stabilises the structure, and PEG-PE gives additional steric stabilisation and increases the particles' circulation half-lifes [6].

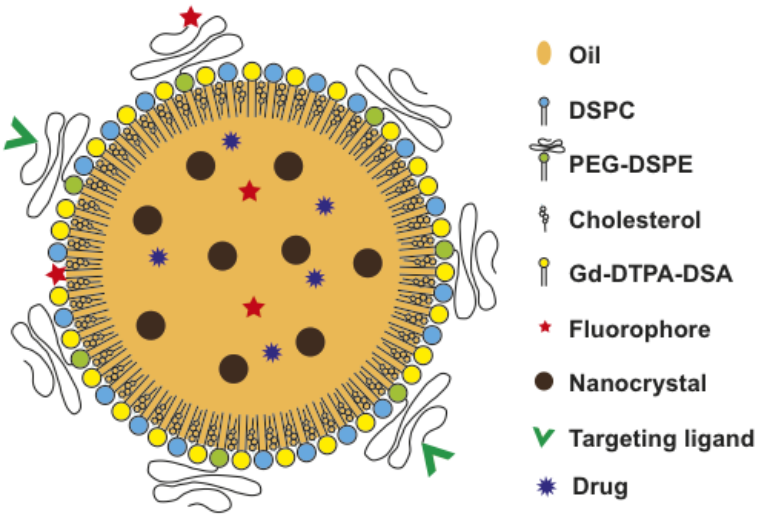

Figure 12: Schematic illustration of a multimodal and multifunctional nanoemulsion with example components incorporated. Illustration adapted from Hak [6].

2.5.4 Loading of functional molecules in nanoemulsions

For imaging, several types of contrast agents are suitable for incorporation into nanoemulsions. Hence, nanoemulsions may be detected with different imaging techniques, e.g fluorescence detection, MRI, CT and single photon emission computed to-

mography (SPECT). As mentioned earlier, by incorporating multiple contrast agents in the same nanoparticle, complementary imaging techniques may be used to detect the same nanoparticle. This may be critical for a good understanding of *in vivo* and *in vitro* nanoparticle behaviour [24]. Nuclear imaging techniques like SPECT and PET do, for example, represent techniques of high sensitivity, but low spatial resolution [6, 24, 26]. This is suitable for scanning large areas and achieve information about the biodistribution of the nanoparticles [24]. MRI on the other hand, has low sensitivity, but high spatial resolution [6, 24, 26]. MRI may therefore be utilised to inspect the areas of interest detected by nuclear imaging techniques, in closer detail and with higher resolution than would otherwise be possible. The ability to perform this complementary imaging with the same nanoparticle, represents a great advantage of utilising nanoemulsions in medical applications, and especially in preclinical optimisation processes [24].

Contrast agents may be incorporated in different layers of nanoemulsions. Hydrophobic molecules may be incorporated in the oil lumen of oil-in-water nanoemulsions. For fluorescence detection, hydrophobic fluorophores like Nile Red 668, DiR and hydrophobically capped quantum dots may be added. For MRI, hydrophobically capped superparamagnetic iron oxide nanoparticles, may be added, as well as fluorinated hydrophobic molecules, which may be used in ^{19}F-MRI. Iodinated hydrophobic molecules, which may be used for CT, is another example [24].

Contrast agents may also be associated with the lipid monolayer of nanoemulsions. Several lipids are commercially available with fluorescent tags, like rhodamine-PE and fluorescein-PE. As fluorescence detection is sensitive, small amounts of fluorophores are necessary for labelling, which is advantageous because it only causes a slight change in nanoemulsion morphology [24]. For MRI, there exist several amphiphilic Gd(III)-chelates which may easily be incorporated into the lipid layer. In such amphiphiles, the Gd-chelate may either *be* the hydrophilic domain of the amphiphile, or the Gd-chelate may be conjugated to the hydrophilic part of another amphiphile [6]. Because nanoemulsions consist of a large number of lipids, it is relatively easy to achieve a high load of amphiphilic Gd-chelates, which is preferable because of the low sensitivity of MRI [24]. Similar to amphiphilic Gd-chelates, amphiphilic ^{99m}Tc(III)-chelates may be utilised for SPECT imaging [62].

In addition to enabling complementary imaging, nanoemulsions may also be utilised to carry a high payload of hydrophobic drugs. Since these drugs are poorly soluble in aqueous solution, they are difficult to administer individually. Encapsulation in nanoemulsions may eliminate the poor solubility problem, and improve the bioavailability of these drugs. This is an important achievement, as approximately 40% of potential new drugs identified by pharmaceutical companies, are poorly soluble in water [63]. Simultaneous loading of drugs and imaging agents is also possible in nanoemulsions, allowing for theranostic nanoparticle production [28].

2.5.5 Surface modification of nanoemulsions

As described above, surface coating of nanoparticles is often necessary to achieve desired pharmacokinetics and biodistribution of the nanoparticles. PEG is one of

the most common molecules for surface coating, and may be very easily incorporated in nanoemulsions. Several commercially available PEG-conjugated amphiphiles exist, e.g. PEG-PE described earlier, which may be incorporated simply by addition to the mixture of other amphiphiles before nanoemulsion production [6]. By utilising the PEG-conjugated lipid DSPE-PEG(2000), up to 50 mol% PEG may be added without affecting nanoemulsion size or size distribution [64]. This is distinctively more than for liposomes, where the maximum achievable PEG-lipid content is ∼10 mol% [6].

Targeting of nanoparticles to specific biomarkers may be achieved by conjugating specific targeting ligands to the nanoparticle surface. This is also relatively easy to perform in nanoemulsions. The most common method utilised, is to covalently attach the targeting ligand to the surface of a nanoparticle which is already formed. Lipids with different functional groups, e.g. maleimide, thiol, amine and carboxylic acid moieties, are commercially available. By the incorporation of these lipids during nanoemulsion production, targeting ligands may later be conjugated to the surface by reaction with the functional groups. A typical pair of chemical groups used for ligand conjugation, is maleimide and thiol groups. For PEGylated nanoemulsions, targeting ligands should be conjugated to the distal end of PEG-lipids, as this will increase the efficiency of both the conjugation and targeting process. An alternative method to achieve targeting ligands on the nanoemulsion surface, is to add a hydrophobic anchor on the targeting ligand. This will create an amphiphile, which may be mixed with the other amphiphiles during nanoemulsion production. From this, the amphiphiles will simply self-assemble into nanoemulsions with targeting ligands on the surface [24].

2.6 Flow cytometry

Flow cytometry is a single cell analysis technique which offers rapid achievement of quantitative data. In flow cytometry, suspended cells or other particlulates are consecutively passed through a laser beam in a directed fluid stream. As the cells or particles pass through the laser beam one by one, information about their interaction with the light is detected, i.e. light scattering in sideways and forward direction, and/or fluorescence emission. This may, for example, give important information about cell phenotype and characteristics [65], such as cell size, membrane potential, intracellular pH, and levels of cellular components like DNA, proteins, surface receptors and calcium [66]. As the parameters of interest are detected seperately for each cell or particle, the *distribution* of the desired parameters in the investigated cell/particle population is visualised. This ability to obtain parameter *distributions* as opposed to one average value for the entire population, is a great advantage of flow cytometry and makes it a unique tool for cell analysis [66].

A flow cytometer has five main components; one or more laser light sources, a flow cell, optical filter units for specific wavelength detection over a broad spectral range, photodiodes and/or photomultiplier tubes for sensitive detection of the signals of interest, and a data processing and operating unit[66]. Figure 13 shows the basic setup of a flow cytometer.

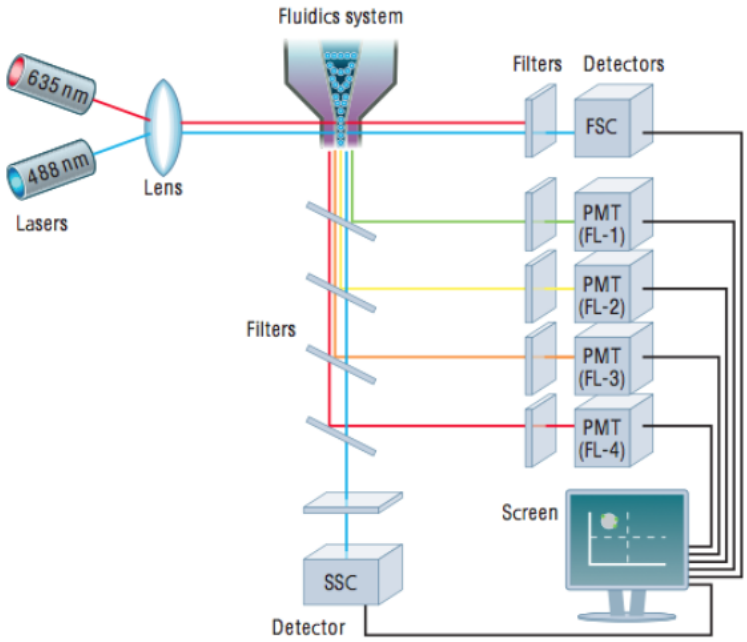

Figure 13: A schematic illustration of the main components of a flow cytometer. Illustration adapted from Rahman [67].

In a flow cytometer, the sample suspension is injected into a flow cell where it is hydrodynamically focused into a fluid stream of very small diameter, allowing only one cell at a time to pass through its cross-section. Hydrodynamic focusing is achieved by surrounding the sample fluid with a sheath fluid, having both stream velocities at the level of laminar flow, and gradually narrow the flow cell diameter. A laser is placed

orthogonal to the flow, and when the hydrodynamically focused flow passes through the laser beam, one and one cell will be illuminated and eject light signals for detection [66].

As the cells pass through the laser beam, light is scattered in all directions. Light scattered in the forward direction (FS), meaning at low angles (0.5-10°) from the direction of the incident beam, is proportional to the square of the radius of a sphere, and thereby gives information about the size of the cell or particle. Light which is scattered to the side (90°) relative to the direction of the incident beam, has typically been reflected and refracted by intracellular components [66]. Hence, the amount of side scatter (SS) gives information about the granularity of the cell [68], but is also affected by cell size and cell morphology [66]. In addition to FS and SS, certain cell components may be selectively detected by the use of fluorescence. Autofluorescent compounds (e.g. NAD(P)H) and compounds stained with fluorescent molecules may be detected by exciting them with proper wavelength laser light, and simultaneously detect their emission at proper wavelengths. If the spectral overlap of different fluorophores' emission spectra is not too large, multiple fluorophores may also be analysed simultaneously. In fact, the most sophisticated flow cytometers are capable of analysing 11 colors of fluorescence at the same time [68].

The emitted light from fluorophores is collected by an objective lens positioned at right angles to the incident beam. The light then passes through a filter which block laser excitation wavelengths, before passing through dichroic mirrors and appropriate filters to select the required wavelengths for fluorescence detection, and direct them to the correct detectors, as illustrated in figure 13. Fluorescence emission and side scattered light is typically detected by photomultiplier tubes, which convert the incoming photons to an electrical impulse. The electrical impulse is then processed by an analog-to-digital converter which produces a numerical signal. Photomultiplier tubes are often utilised for detection of these signals because they are suitable for weak light conditions and they offer the necessary amplification of relatively weak fluorescent signals. In the forward scatter direction, scattered light intensity is generally high, and photodiodes are typically used as detectors. A beam absorber is placed in front of the detector to stop the incident laser beam itself or any diffracted light from entering the detector. The scattered light is focused onto the photodiode by a collective lens, and the photodiode converts the signal into voltage pulses which are proportional to the amount of light detected [68].

The different parameteres detected for each cell are processed and analysed by the cytometer software. The different scattering and fluorescent signals may then be plotted in various combinations, to select and observe all subpopulations [66]. Although cells are analysed individually in flow cytometry, results are analysed collectively [68]. Data acquired from the flow cytometer may be presented i single-parameter histograms or in two- or three-parameter scatter plots. The FS versus the SS signal is typically plotted in a two-parameter scatter plot. This enables the visualisation of different subpopulations of cells, and may be utilised to exclude cellular fragments and cell agglomerations from the further analysis. In a single-parameter histogram, the x-axis represents the parameter to be investigated and the y-axis represents the number of cells (count). This is typically utilised to present the number of cells as a function of the fluorescence intensity of a specific fluorophore.

2.7 Confocal laser scanning microscopy

Confocal laser scanning microscopy (CLSM) is an optical microscopy technique which has proved very useful for studying biological samples stained with one or several fluorescent probes. This technique has become increasingly popular in recent years, mainly because of its ability to obtain extremely high-quality images from samples prepared for conventional fluorescence microscopy. The key advantage of confocal microscopy compared to other conventional widefield optical microscopy techniques, is that confocal microscopy manages to eliminate out-of-focus light in specimens whose thickness is larger than the plane of focus. Hence, using confocal microscopy, imaging of thin optical slices of biological samples may be achieved with minimal background noise [69]. In comparison to flow cytometry which is a quantitative technique, confocal laser scanning microscopy acquires qualitative data.

An illustration of the principle of confocal microscopy is shown in figure 14. In a confocal microscope, the laser system emits coherent light (excitation light), which passes through a pinhole aperture before it is reflected by a dichromatic mirror towards the sample. This pinhole aperture is positioned in a conjugate (confocal) plane to the focal plane of the sample. After the dichromatic mirror, the excitation light is collected by an objective lens and focused to a small focal volume centered in the focal plane in the sample, where it excites fluorophores. Fluorescence emission from the sample as well as reflected and refracted excitation light, pass back through the objective lens and hit the dichromatic mirror. Here, excitation wavelengths are blocked, allowing only fluorescence emission signals to pass through [69].

A second pinhole is placed, also in a conjugate (confocal) plane to the focal plane in the specimen, in front of the detector. Fluorescence emission from out-of-focus planes are not confocal with the pinhole, and are thereby projected onto the pinhole aperture as airy disks with relatively large diameter. Fluorescence emission from in-focus planes, on the other hand, are projected onto the pinhole aperture as very small airy disks. The largest fraction of these small disks fit through the pinhole and thereby reach the detector. However, only a small fraction of the large airy disks from out-of-focus signals do the same, and most out-of-focus signals are thereby eliminated from the image. In this clever manner, an image taken by a confocal microscope contains much less background noise and achieves better contrast than conventional fluorescence microscopy techniques. By refocusing the objective, the plane in the sample which is confocal with the pinhole apertures of the light source and detectors is shifted. This allows easy selection of the desired focal plane. Also, the thickness of the imaged optical section may be varied by changing the diameter of the pinhole in front of the detector [69].

As mentioned, the objective lens focuses the excitation light to a small focal volume centered in the focal plane. The size of the illuminated volume typically ranges from ~ 0.25 - 0.8 μm in diameter and ~ 0.5 - 1.5 μm in height at the brightest intensity. To achieve an image of the desired specimen with confocal microscopy, the focused illumination spot has to be scanned across the relevant area. This scanning is controlled by two high-speed oscillating mirrors driven by galvanometer motors, positioned between the dichromatic mirror and the objective. The illumination spot is scanned in a raster pattern, where one of the mirrors moves the spot in the x-direction and the other mir-

ror moves the spot in the y-direction in the focal plane. As the scanning system works its way across the relevant area, fluorescence emission is collected by the objective and pass back through the scanning unit towards the dichromatic mirror. As the speed of the scanning mirrors is very slow compared to the speed of light, fluorescence emission will follow the exact same path as the excitation light back to the dichromatic mirror [69].

The detector in a confocal microscope is usually a photomultiplier tube. When fluorescence emission hit the photomultiplier tube, the signal is converted to an analog electrical signal, with a continuously varying voltage corresponding to light intensity. This analog signal is then converted by an analog-to-digital converter and the confocal microscope software processes the data, and reconstructs the image point by point to display the final image. A general advantage of utilising fluorescence in microscopy, is that fluorescent molecules of sizes below the spatial resolution (governed by the diffraction limit of specimen features) may be detected. This allows for detection of very small features. In confocal laser scanning microscopy, several fluorophores may also be imaged simultaneously by the utilisation of various lasers and filters. Each fluorophore is then detected seperately and form individual images, which may later be merged and visualised together [69].

The resolution and contrast of the final image in confocal microscopy, may be adjusted by adjusting the scan speed of the illumination spot across the sample. A slower scan speed results in improved resolution and contrast, but naturally requires longer time. In confocal microscopy, magnification may also be adjusted electronically (without the need to change objective), by adjusting the area scanned by the laser. This adjustment is called the *zoom factor*. Increasing the zoom factor both reduces the scanned area and the scanning rate. This results in an increased number of samplings along a certain length of the sample, and increases the image spatial resolution of the magnified area [69].

A key attribute of confocal laser scanning microscopy, and a reason for its popularity for imaging biological samples, is the ability to perform *optical* sectioning of samples. Due to its non-invasiveness, thin-section-imaging may be achieved for both living and fixed specimens, as physical sectioning is not needed. In addition, artifacts which may arise during physical sectioning of samples are eliminated when utilising optical sectioning. Serial optical sections may also be imaged and processed to form a three dimensional image of the sample. Several other methods of imaging is also available when utilising a confocal microscope, e.g. imaging of the specimen cross-section by scanning a specific line at serial depths, the formation of image time-series, and imaging of unstained samples utilising reflected or transmitted light to form the image [69].

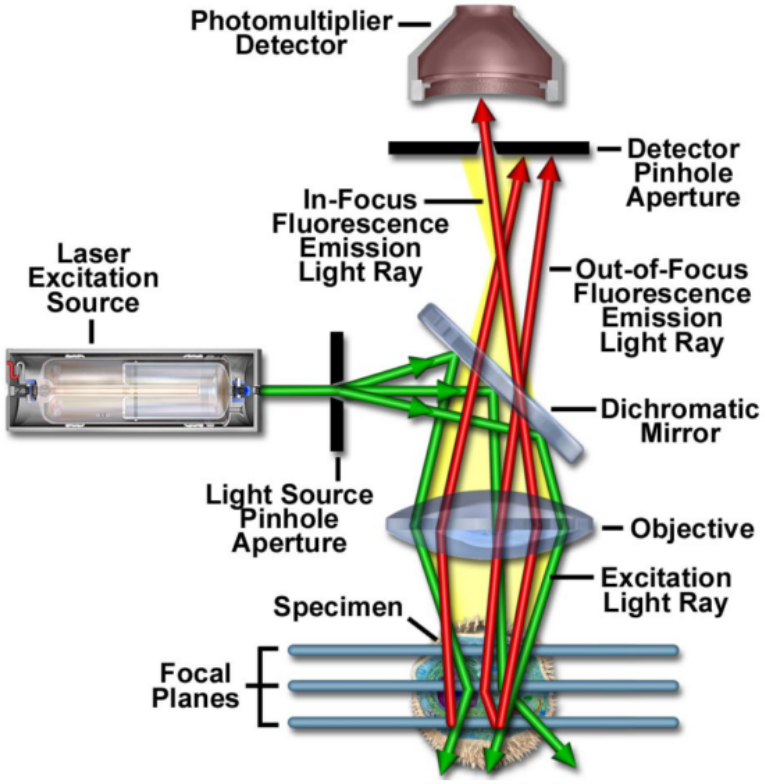

Figure 14: A schematic illustration of the main components and working principle of a confocal laser scanning microscope. Illustration adapted from Claxton et al. [69].

2.8 *In vitro* model system

For development and investigation of potential new therapeutic and diagnostic approaches, initial experiments are often performed *in vitro* with cells in culture. The use of *in vitro* experiments is necessary to reduce the extent of animal testing, which is important due to ethical constraints, and to reduce cost and time consumption. However, an important limitation for *in vitro* experiments, is that the cellular environment in a culture dish differ significantly from the *in vivo* cellular environment [70]. Therefore, cellular responses observed *in vitro* are not necessarily representative for cellular responses *in vivo*.

In this project, cultured human umbilical vein endothelial cells (HUVEC) were utilised as an *in vitro* model system to study $\alpha_v\beta_3$-integrin targeting. HUVEC grown in culture display many of the characteristics of angiogenic endothelial cells, including expression of $\alpha_v\beta_3$-integrins [71]. HUVEC are adherent cells. Cell growth of cultured cells, begin with the lag phase after seeding, where adherent cells adhere to the new substrate. Next, the log phase follows, where cells proliferate exponentially. At one point, the adherent cells will occupy all available substrate. Hence, the cells have no space left for expansion, and proliferation is greatly reduced or cease entirely [72]. The phase of cell growth is important for experiments investigating the $\alpha_v\beta_3$-integrin in cultured HUVEC, because expression of $\alpha_v\beta_3$-integrin is upregulated in proliferating endothelial cells *in vitro*, while non-proliferating endothelial cells express $\alpha_v\beta_3$ at low levels [73].

3 Materials and methods

3.1 Materials

The fluorescent cell markers CellMask™ Deep Red Plasma Membrane Stain (further 'CellMask™') and Calcein AM were purchased from Life Technologies, and Hoechst 34580 (further 'Hoechst') was purchased from Sigma-Aldrich®. The CellMask™ consist of amphipathic molecules providing a lipophilic moiety for membrane loading and a negatively charged hydrophilic dye for "anchoring" of the probe in the plasma membrane. CellMask™ has excitation and emission maxima at approximately 649 nm and 666 nm, respectively [74]. Hoechst belongs to the family of blue fluorescent Hoechst dyes which are cell permeable nucleic acid stains. Hoechst has excitation and emission maxima at approximately 360 nm and 440 nm, respectively, when bound to DNA [75]. Calcein AM is a non-fluorescent cell-permeant molecule which, in live cells, is converted to the fluorescent molecule Calcein by intracellular esterases. Calcein is not cell-permeant and is therefore trapped inside the cell. Calcein has excitation and emission maxima at approximately 490 nm and 515 nm, respectively [76].

The antibody Anti-Integrin $\alpha_v\beta_3$ Antibody (clone LM609, MAB1976) was purchased from Merck Millipore. This antibody is a monoclonal antibody against integrin $\alpha_v\beta_3$ produced in mice, suitable for e.g. flow cytometry. The clone LM609 has been demonstrated to block adhesion of a human melanoma cell line (M21) to synthetic RGD containing peptides. However, LM609 does not interact directly with the RGD binding site. Instead, LM609 appears to be an allosteric inhibitor of integrin $\alpha_v\beta_3$, which binds to a conformational epitope resulting from the post-translational association of the α_v and β_3 subunits [77].

The antibody F(ab')2-Goat anti-Mouse IgG (H+L) Secondary Antibody, Alexa Fluor® 488 conjugate was purchased from Life Technologies. This antibody is a polyclonal, secondary antibody with well-characterised specificity for mouse immunoglobulins. It is conjugated to the fluorescent molecule Alexa Fluor® 488, which has excitation and emission maxima at approximately 495 nm and 519 nm, respectively [78].

The plasmid DNA ITGB3 (GFP-tagged) - Human integrin, beta 3 (platelet glycoprotein IIIa, antigen CD61) was purchased from OriGene Technologies. This plasmid clone was engineered to express the complete open-reading-frame with an expression tag, which is a C-terminal TurboGFP (green fluorescent protein) [79]. TurboGFP has excitation and emission maxima at approximately 482 nm and 502 nm, respectively [80]. As $\alpha_v\beta_3$-integrin is the only β_3-containing integrin in HUVEC [81], successful transfection of a GFP-tagged β_3-integrin should provide a suitable and selective marker for $\alpha_v\beta_3$-integrins in HUVEC.

8-well μ-Slides (ibiTreat) purchased from Ibidi were utilised for imaging of live cells. 8-well μ-Slides are chambered coverslips and cells grown in these chambers may therefore be imaged directly on the microscope. 8-well Nunc™ Lab-Tek™ II Chamber Slides™ with cover, purchased from LAB-TEK® Brand Products, Thermo Fisher Scientific, were utilised for imaging of fixed cells. 8-well Nunc™ Lab-Tek™ II Chamber Slides™ are chambered glass microscope slides with removable polystyrene chamber walls. After fixation, cells on the glass microscope slides may therefore be imaged

by removing the chamber walls and sealing a cover glass to the microscope slide. Vectashield® Mounting medium for fluorescence with DAPI, was purchased from Vector Laboratories, Inc. Burlingame. DAPI stains nucelic acids and has excitation and emission maxima at approximately 358 nm and 461 nm, respectively [82].

3.1.1 Nanoemulsions

Oil-in-water nanoemulsions (NE) were prepared by Postdoc Sjoerd Hak through a method based on swift evaporation of organic solvents as previously described [83]. The amphiphilic lipids 1,2-disteraoyl-sn-glycerol-3-phosphocholine (DSPC), cholesterol, and 1,2-disteraoyl-sn-glycerol-3-phosphoethanolamine-N-[maleimide(polyethylene glycol)-2000] (Mal-PEG-DSPE) (all from Avanti Polar Lipids) were used at a molar ratio of 62:33:5. For fluorescently labelled NE, 0.2 mol% of the fluorophore Nile Red 668 (a hydrophobic nile red analogue [84], a kind gift from Sintef) or rhodamine-PE (L-α-phosphatidylethanolamine-N-(lissamine rhodamine B sulfonyl)) (Avanti Polar Lipids) and 2.6 mg of soybean oil per μmole of the amphiphilic lipid mixture were included. The hydrophobic Nile Red 668 is incorporated in the oil core, while rhodamine conjugated to PE is on the NE surface. Unlabelled NE were prepared the same way as fluorescent NE, except fluorophores were left out. All ingredients were combined in chloroform and dripped into 5 ml of Hepes Buffered Saline (HBS, 2.38 g/L Hepes and 8 g/L NaCl, pH 6.7) at 72°C under vigorous magnetic stirring (1300 rpm). The obtained crude emulsions were tip-sonicated for 20 min (Heat System Ultrasonics, W-225R, duty cycle 35%, 30 W and 20 kHz) in a water bath to maintain room temperature. Half of the final NEs were conjugated with RGD peptide (c[-RGDf(-S-acetylthioacetyl)K-], Peptides International) and half of the emulsions were conjugated with RAD peptide (c[-RADf(-S-acetylthioacetyl)K-], Peptides International). Before conjugation, the thiol group on the RGD peptide was deacetylated at pH 7 for 1 h. The activated peptide was added to the NEs and the mixture was left to react overnight at 4°C. The NEs were dialysed (Spectra/Por Float-A-Lyzer G2, 100 kDa molecular weight cut-off, Spectrum Laboratories) against HBS of pH 7.4 to remove unconjugated RGD and to obtain physiological pH. After preparation, the NEs were stored at 4°C for a minimum of 5 days before using them in experiments to ensure hydrolysis of unreacted maleimide groups.

NE conjugated with the RAD peptide serve as control NE. The substitution of glycine (G) with alanine (A) makes the peptide inactive when it comes to $\alpha_v\beta_3$-binding. The RAD peptide sequence is therefore a strong negative control for investigating the biological activity mediated by $\alpha_v\beta_3$-integrin [85].

NE labelled with rhodamine-PE and Nile Red 668 will further be referred to as RHO-NE and NR-NE, respectively, while unlabelled NE will be referred to as UL-NE. Further, NE conjugated with RGD and RAD will be referred to as RGD-NE and RAD-NE, or targeted and non-targeted NE, respectively. The stated concentrations of NE solutions in this thesis, refer to the concentration of amphiphilic lipids in the solution (sum of DSPC, cholesterol and Mal-PEG-DSPE). The NE produced by this method are $\sim$ 100 nm in diameter.

3.2 Cell cultivation

Human umbilical vein endothelial cells (HUVEC, Lonza Biosciences) were cultured in Endothelial cell basal medium-2 (EBM-2, Lonza, Clonetics) supplemented with a SingleQuots™ Kit (EGM-2 SingleQuots, Lonza, Clonetics) containing 10 ml fetal bovine serum (FBS), 2 ml rhFGF-B, 0.5 ml ascorbic acid, 0.5 ml R^3-IGF-1, 0.5 ml rhEGF, 0.5 ml VEGF, 0.5 ml heparin, 0.5 ml GA-1000, gentamicin sulfate amphotericin-B, and 0.2 ml hydrocortisone. HUVEC were grown in 75 cm^2 cell cultivation flasks (VWR International), incubated in 15 ml culture medium at 37 °C with 5% CO_2, and passaged onto new flasks at $\sim$ 80 % confluency. Passaging occured by removal of culture medium, washing with 5 ml phosphate buffered saline (PBS, Sigma Aldrich), and addition of 3 ml solution of 0.25%/0.02% trypsin/EDTA (Sigma Aldrich) before the flask was placed at 37 °C for 2-3 minutes for cell detachment. Cell detachment was confirmed using a light microscope (Leica DMIL), before trypsination was stopped by addition of 10 ml culture medium. 12 ml of cell suspension was transferred to a centrifuge tube (Corning® CentriStar™), and centrifuged (Heraeus Instruments, Megafuge 1.0) for 5 min at 1500 rpm. The remaining 1 ml in the flask was used to count the cells with a digital cell counter; a droplet of cell suspension was transferred to each chamber of a Countess™ cell counting chamber slide (Invitrogen™) and cells were counted by the Countess™ Automated Cell Counter (Invitrogen™). The supernatant was removed from the centrifuged cells and cells were resuspended in culture medium to a concentration of 200 000 or 250 000 cells/ml. 300 000 cells were transferred to a new flask and incubated in a total volume of 15 ml culture medium. Culture medium, PBS and trypsin solution were all heated to 37 °C in a water bath prior to use.

Cells of passage 4 to 7 were used in experiments. For flow cytometry experiments, cells were seeded in 12-well Tissue Culture Plates (Falcon®) 1 or 2 days before experiments, with respectively 40 000 or 25 000 cells in 1 ml culture medium per well. For microscopy experiments, cells were seeded in 8-well μ-Slides (ibiTreat, Ibidi), or 8-well Nunc™ Lab-Tek™ II Chamber Slides™ with cover (LAB-TEK® Brand Products, Thermo Fisher Scientific). For optimisation of fixation protocol, cells were seeded in both 8-well μ-slides (Ibidi) and 8-well Nunc™ Lab-Tek™ II Chamber Slides™ with cover, 1 day before experiments, with 15 000 cells in 300 μl culture medium per well. For experiments with real-time imaging of NE incubation and transfection, cells were seeded in 8-well μ-slides (Ibidi) 1 day before experiments, with 5000 cells in 300 μl culture medium per well. Cells were incubated at 37 °C with 5% CO_2 until experiments were performed.

3.3 Experiments with FCM

3.3.1 Studies of fluorophore leakage

To investigate the occurence of fluorophore leakage from fluorescently labelled NE to HUVEC, cells were incubated with NE at 4°C to inhibit endocytic uptake of NE [85]. The experiment was also performed at 37°C, to compare the extent of leakage to actual NE uptake. Cells seeded in 12-well plates were placed at the correct temperature (4°C or 37°C) 15 min prior to incubation. Stock-solutions of fluorescently labelled NE (RHO-NE or NR-NE) were diluted to a concentration of 1 mM in culture medium of correct temperature (4°C or 37°C), immediately before incubation. Cells were incubated in 300 μl of 1 mM NE-solution in the fridge (4°C) or incubator (37°C) for 15 min or 60 min. After incubation, NE-solutions were removed and cells were washed three times with 1 ml PBS of the correct temperature (4°C or 37°C). 200 μl of 0.25%/0.02% trypsin/EDTA (37°C) was added and cells placed at 37°C for 2-3 min for cell detachment. 400 μl ice cold 15 % FBS (Life Technologies, Invitrogen) in PBS was added, and samples were pipetted into flow tubes and placed on ice until flow cytometry analysis. Experiments were performed in singlet for each fluorophore. An autofluorescent sample (not incubated with NE-solution, but with pure culture medium) was also included.

3.3.2 Saturation studies of RGD-to-surface-$\alpha_v\beta_3$ binding

To study saturation kinetics of binding between surface $\alpha_v\beta_3$-integrins and RGD-NE, cells were incubated with different concentrations of NE for 2.5 min. The experiment was performed as described in 3.3.1, except cells were incubated in 300 μl of 1 μM, 10 μM, 0,1 mM, 0.5 mM or 1 mM RHO-NE or NR-NE-solution for 2.5 min, at 37°C. Experiments were performed in duplicates for RHO-NE and in singlet for NR-NE. An autofluorescent sample (not incubated with NE-solution, but with pure culture medium) was also included.

3.3.3 Incubation pause experiments

In vitro experiments performed by Hak et al. [9] supporting their hypothesis, were repeated and developed further in this project. These experiments will further be referred to as *incubation pause experiments*. In the study by Hak et al., cells were incubated with 1 mM RHO-NE for two periods of 4 min separated by a pause of varying length. Here, both NR-NE and RHO-NE were utilised, and two different concentrations (0.1 mM and 0.9 or 1 mM) of NE-solution were tested. For NR-NE, a concentration of 0.9 mM was used in stead of 1 mM, due to insufficient amounts of NR-NE left. In addition to incubate cells with fluorescently labelled NE in both incubation periods, cells were incubated with unlabelled (UL) NE in one period and fluorescently labelled NE in the other. A summary of the different incubation pause experiments performed, is found in table 1.

Concentration of NE-solution (mM)	NE-type in first incubation	NE-type in second incubation	Number of parallels (n)
0.1	NR-NE	NR-NE	2
0.1	RHO-NE	RHO-NE	2
0.9	NR-NE	NR-NE	1
1	RHO-NE	RHO-NE	2
0.9	UL-NE	NR-NE	1
1	UL-NE	RHO-NE	4
1	RHO-NE	UL-NE	2

Table 1: Table summarising the different incubation pause experiements performed. NR-NE: Nile Red 668 labelled NE, RHO-NE: Rhodamine-PE labelled NE, UL-NE: unlabelled NE.

Experiments were performed at 37°C. Stock-solutions of the relevant type of NE were diluted in culture medium (37°C) immediately before incubation. Cells seeded in 12-well plates were incubated in 300 μl of NE-solution (with concentration and type of NE as presented in table 1, first incubation) for 4 minutes. NE-solution was removed and cells were washed 3 times with 1 ml PBS (37°C), prior to addition of 300 μl culture medium. After a total incubation pause of 1.5, 3, 6, 10 or 15 minutes (counted from the time of removal of NE-solution), cells were again incubated in 300 μl of NE-solution (with concentration and type of NE as presented in table 1, second incubation) for 4 minutes. After incubation, NE-solution was removed and cells were washed three times with 1 ml PBS (37°C). 200 μl of 0.25%/0.02% trypsin/EDTA (37°C) was added and incubated 2-3 min to allow cell detachment. 200 μl ice cold 15 % FBS in PBS was added, and samples were pipetted into flow tubes and placed on ice until flow cytometry analysis.

An autofluorescent sample (not incubated with NE-solution, but with pure culture medium) was included in all incubation pause experiments. In most experiments, samples only incubated with fluorescently labelled NE for 4 min were also included. In one experiment, a sample incubated with fluorescently labelled NE for 8 min was also included. These samples were washed and detached like the other samples.

3.3.4 Introductory studies for immunolabelling of surface $\alpha_v\beta_3$-integrin

To determine surface expression of $\alpha_v\beta_3$-integrins, adherent cells were immunolabelled on ice. Cells were detached after immunolabelling and three different cell detachment methods were tested to find the one most suitable for our experiments. An experiment was also performed to assure saturation binding of the primary antibody.

Comparison of three cell detachment methods
Cells seeded in 12 well plates were placed on ice for two minutes, prior to incubation with 300μl of mouse anti-integrin $\alpha_v\beta_3$ antibody (0.3μg/100μl) solved in ice cold PBS with 1% BSA (Sigma-Aldrich), for 45 minutes on ice. Cells were washed 3 times with 1 ml of ice cold PBS with 1% BSA, prior to incubation with 300μl of Alexa Fluor® 488 goat anti-mouse IgG secondary antibody (0.5μg/100μl) solved in ice cold PBS with

1% BSA, for 30 minutes on ice. Cells were washed 3 times with 1 ml of ice cold PBS with 1% BSA, before three different cell detachment methods were tested:

- **Detachment by EDTA:** 300 μl of EDTA-solution (10mM EDTA (EMD Biosciences, Inc) in PBS, 37°C) was added and cells incubated at 37°C until they were detached ($\sim$ 25 min). Samples were transferred to flow tubes and placed on ice.
- **Detachment by trypsination:** 200 μl of 0.25%/0.02% trypsin/EDTA (37°C) was added and cells incubated at 37°C until they were detached (2-3 min). 200 μl of ice cold 15 % FBS in PBS was added to stop trypsination. Samples were transferred to flow tubes and placed on ice.
- **Detachment by scraping:** 200 μl of culture medium was added and cells detached by utilising a Cell Scraper (BD Falcon). Samples were transferred to flow tubes and placed on ice.

To assure the same backgroud signal from all detached samples, they were centrifuged (Heraeus Instruments, Megafuge 1.0) for 5 min at 1500 rpm, and resuspended in 300 μl of culture medium at 4°C. The samples were subsequently placed on ice until flow cytometry analysis. Experiments were performed in duplicates.

Assuring saturation binding of primary antibody
To assure saturation binding of surface $\alpha_v\beta_3$-integrins with the utilised concentration of primary antibody (0.3μg/100μl), experiments were performed as described above for samples detached with EDTA, except both 0.3μg/100μl and 1μg/100μl of mouse anti-integrin $\alpha_v\beta_3$ antibody solutions were tested. Experiments were performed in duplicates.

3.3.5 Expression of surface $\alpha_v\beta_3$-integrins after incubation with nanoemulsions

To investigate if incubation with RGD- and RAD-NE affect the surface expression of $\alpha_v\beta_3$-integrin in HUVEC, cells were incubated with NE for different periods, prior to immunolabelling of surface $\alpha_v\beta_3$-integrins. Stock-solutions of RHO-NE were diluted to a concentration of 1 mM in culture medium (37°C), immediately before incubation. Cells seeded in 12 well plates were incubated with 300 μl of NE-solution for 0, 2, 5, 10 or 30 minutes at 37°C. Immediately after incubation with NE, cells were placed on ice and washed 3 times with 1 ml of ice cold PBS. Cells were then immunolabelled as described in 3.3.4, and trypsination was utilised as detachment method. As different background signals was not an issue in this experiment, samples were not centrifuged and resuspended prior to flow cytometry analysis. Experiments were performed in duplicates.

One experiment was also performed where cells were allowed time for $\alpha_v\beta_3$-integrin recycling to occur, after NE-incubation. Cells were then treated as described above, except after NE-incubation cells were washed 3 times with 1 ml PBS (37°C) before 300 μl of culture medium (37°C) was added. Cells were then placed in the incubator (37°C) for 20 minutes, before they were placed on ice and washed 3 times with 1 ml

of ice cold PBS. Immunolabelling and cell detachment was as for the other samples. Experiments were performed in singlet.

Control samples included in these experiments were; An autofluorescent sample (not exposed to NE or antibodies), a sample to test unspecific binding of the secondary antibody (not exposed to NE or primary antibody, but exposed to secondary antibody), and a sample to test possible bleedthrough of rhodamine-PE emission in the detection of the secondary antibody fluorescence (incubated with NE for 30 min, but not exposed to antibodies).

3.3.6 Expression of surface $\alpha_v\beta_3$-integrins on cells of different confluency

As non-proliferating HUVEC have reduced expression of the target $\alpha_v\beta_3$-integrin, compared to proliferating cells [73], samples of different confluency (up to $\sim$ 100% confluency) were labelled with the described immunolabelling protocol, to test if we could detect differences in $\alpha_v\beta_3$-integrin surface expression. To achieve samples of different confluency on the day of experiments, 10 000, 25 000, 50 000 and 80 000 cells were seeded in 12 well plates, as described in 3.2. Experiments were performed when the wells seeded with 80 000 cells appeared 100% confluent, which was three days after seeding. Although causing more cell death in the almost confluent wells, the experiment was repeated, but now with seeding of 10 000, 25 000, 50 000 and 100 000 cells, four days prior to experiments. On the day of experiments, cells were immunolabelled with the protocol described in 3.3.4, and trypsination was utilised as detachment method. As different background signals was not an issue in this experiment, samples were not centrifuged and resuspended prior to flow cytometry analysis. Experiments were performed in duplicates. Control samples included in these experiments were; An autofluorescent sample (not exposed to antibodies), and a sample to test unspecific binding of the secondary antibody (not exposed to primary antibody, but exposed to secondary antibody).

3.3.7 Uptake of nanoemulsions in cells of different confluency

For the same reason as above (section 3.3.6), cells of different confluency were incubated with RGD- and RAD-NE to test if we could detect differences in NE uptake in the different samples. To achieve cells with different confluency on the day of experiments, 10 000, 25 000, 50 000 and 100 000 cells were seeded four days prior to experiments. Cells were seeded in 12 well plates, as described in 3.2. On the day of experiments, stock-solutions of RHO-NE were diluted to a concentration of 1 mM in culture medium (37°C), immediately before incubation. Cells were incubated with 300 μl of NE-solution for 15 minutes at 37°C. Subsequently, cells were washed 3 times with 1 ml PBS (37°C). 200 μl of 0.25%/0.02% trypsin/EDTA (37°C) was added and cells placed at 37°C for 2-3 min for cell detachment. 200 μl ice cold 15 % FBS in PBS was added, and samples were pipetted into flow tubes and placed on ice until flow cytometry analysis. Experiments were performed in duplicates. An autofluorescent sample (not incubated with NE, but with pure culture medium) was included for comparison.

3.3.8 Flow cytometric measurements

Fluorescence intensity of the different fluorophores was measured by flow cytometry (Gallios, Beckman Coulter). A 488 nm laser was used to excite Alexa Fluor® 488 goat anti-mouse IgG secondary antibody, and a 561 nm laser was used to excite rhodamine-PE and Nile Red 668. Fluorescence emission from Alexa Fluor® 488 goat anti-mouse IgG secondary antibody was detected in the interval 505 - 545 nm, fluorescence emission from rhodamine-PE was detected in the interval 574,5 - 589,5 nm and fluorescence emission from Nile Red 668 was detected in the interval 605 - 635 nm. For each sample, collection of data was terminated either when 10 000 cells had been counted or data had been collected for 5 min. Cell counts ranged from 4000 - 10 000 cells.

Cellular fragments, debris and agglomerations were excluded from the analysis by gating the SSC versus the FSC plot. Histograms of cell count as a function of fluorescence intensity were used to position the fluorescence peak in the center of the first decade for the autofluorescent sample (by adjusting the gain of the detector), before recording of data was initiated.

3.4 Experiments with CLSM

3.4.1 Optimisation of fixation protocol

To investigate the possibility of studying the distribution of NE in HUVEC after different incubation periods by using fixed cells, an experiment testing 12 different fixation protocols was performed. The results for fixed cells were compared to live cells incubated with NE for the same time as the fixed samples.

Fixed cell samples
Stock-solutions of RHO-NE were diluted to a concentration of 1 mM in culture medium (37°C), immediately before incubation. Cells seeded in 8-well Nunc™ Lab-Tek™ II Chamber Slides™ were incubated with 100 μl of NE-solution for 20 minutes at 37°C. Cells were then washed 3 times with 1 ml PBS (37°C). Followingly, cells were fixed with paraformaldehyde (PFA, Sigma-Aldrich) by incubation with 300 μl PFA in PBS (concentrations and incubation times listed below). Each combination of PFA concentration and incubation time was tested at three different temperatures (4°C, 22°C and at 37°C). This gave a total of 12 different fixation protocols tested.

- 2% PFA in PBS, 10 min incubation, at 4°C, 22°C or 37°C
- 2% PFA in PBS, 15 min incubation, at 4°C, 22°C or 37°C
- 4% PFA in PBS, 10 min incubation, at 4°C, 22°C or 37°C
- 4% PFA in PBS, 15 min incubation, at 4°C, 22°C or 37°C

After incubation with PFA in PBS, samples were washed 3 times with 1 ml of PBS (22°C). The polystyrene media chambers of the Nunc™ Lab-Tek™ II Chamber Slides™ were removed from the glass microscope slides making up the bottom of the wells. One droplet of Vectashield® Mounting medium for fluorescence with DAPI,

was added to each of the eight samples on the glass microscope slide. A cover glass (Thickness no. 1, borosilicate glass, VWR International) was pressed down on the Vectashield®-covered surface, and nail polish was used to seal the glass microscope slide and the cover glass together. Samples were imaged on a confocal microscope (Leica TCS SP8) the same day as experiments, as described in 3.4.4. Each fixation protocol was performed in singlet.

Live cell samples
Stock-solutions of RHO-NE were diluted to a concentration of 1 mM in culture medium (37°C), immediately before incubation. Cells seeded in 8-well μ-slides (Ibidi) were incubated with 100 μl of NE-solution for 20 minutes at 37°C. Cells were then washed 3 times with 1 ml PBS (37°C), and immediately imaged on a confocal microscope (Leica TCS SP8) as described in 3.4.4.

3.4.2 Real-time imaging of NE incubation - optimisation for automated data analysis

A series of experiments were performed to develop a protocol where the intracellular NE distribution could be monitored by real-time imaging of NE-incubation. This was done by imaging a 30 min time series of cells incubated with NE on the microscope. As previous work within the group has shown NE accumulation in the perinuclear region [86], we aimed to detect NE fluorescence in the cell cytosol as a whole and selevtively in the perinuclear region. The experimental protocol was optimised with cell stainings to allow automated data analysis, with detection of the relevant regions-of-interest (ROIs) (cytosol and perinuclear region) and measurment of fluorescence intensity in these ROIs throughout the time series.

No cell staining
Cells seeded in 8-well μ-slides (Ibidi) were given the proper volume of culture medium needed to make a final solution of 150 μl with 1 mM NE-concentration after addition of NE stock-solution. (This volume was approximately 125 μl.) Cells in 8-well μ-slides (Ibidi) were placed on the confocal microscope (Leica TCS SP8). Once a desired region to image was found, the proper amount of NE stock-solution to make a final solution of 150 μl with 1 mM NE-concentration, was added into the culture medium of the relevant well and mixed by pipetting. As fast as possible after addition of NE stock-solution, the z-position and detector gain and offset was chosen, and the capturing of a time series of 30 min was initiated. Details on the imaging procedure is found in 3.4.4. The time from addition of NE stock-solution to the initiation of the time series was noted. Images were also taken before and after each 30 min time series was captured. Cells imaged in the time series were imaged in different z-positions, and cells from other parts of the well were imaged. These experiments were performed with both RHO-NE and NR-NE. 2 - 3 parallels were performed for each of RAD- and RGD-conjugated RHO-NE and NR-NE.

Cells stained with Hoechst nuclear stain and CellMask™ plasma membrane stain or Calcein AM cytoplasm stain

Staining of the nucleus with Hoechst was performed on all wells simultaneously, on the morning of experiments. Cells seeded in 8-well μ-slides (Ibidi) were incubated with 150 μl of 1 μg/ml Hoechst solved in culture medium for 15 min at 37°C. Cells were then washed 3 times with 200 μl of culture medium (37°C). Cells were given 300 μl of culture medium and incubated at 37°C with 5% CO_2 until they were the next sample to be imaged. Staining of the plasma membrane with CellMask™ or of the cytoplasm with Calcein AM, was performed on each well directly before real-time imaging of NE-incubation. For staining of the plasma membrane, cells were incubated with 150 μl of 2.5 μg/ml CellMask™ solved in culture medium for 5 min at 37°C. For staining of the cytoplasm, cells were incubated with 150 μl of 1 μg/ml Calcein AM solved in culture medium for 15 min at 37°C. Cells were then washed 3 times with 200 μl of culture medium. After this, cells were treated as described for cells with no cell staining. These experiments were only performed with RHO-NE. For cells stained with CellMask™, 3 parallels were performed for RGD-NE and 2 parallels were performed for RAD-NE. For cells stained with Calcein AM, 5 parallels were performed for RGD-NE and 3 parallels were performed for RAD-NE. One experiment was also performed where cells were only stained with Hoechst according to the protocol described above. This experiment was only performed once with RGD-NE.

3.4.3 Introductory studies with transfection of GFP-tagged β_3-integrin

To monitor the distribution of $\alpha_v\beta_3$-integrins in HUVEC during NE incubation or other stimuli, transfection of a vector encoding a GFP-tagged human β_3-integrin was tested (presented in section 3.1). As we had no experience with transfection in HUVEC or with the purchased plasmid, an experiment testing several transfection protocols was performed. For transfection experiments, the transfection reagent Lipofectamine® 2000 Reagent (1mg/ml, Invitrogen) was utilised. Amounts of plasmid DNA utilised per well, as well as transfection reagent-to-DNA ratios tested, are presented in table 2.

μg of plasmid DNA	Ratio of Lipofectamine® 2000 (μl) : DNA (μg)
0.05	5:1, 3:1, 1:1, 0.5:1
0.1	5:1, 3:1, 1:1, 0.5:1
0.5	3:1

Table 2: Table presenting the nine combinations of amount of DNA and ratios of transfection reagent-to-DNA tested.

On the day of transfection, Lipofectamine® 2000 Reagent was diluted in Opti-MEM® I (1x) Reduced Serum Medium (Gibco by Life Technologies). Followingly, plasmid DNA was diluted in Opti-MEM® I (1x) Reduced Serum Medium, and 15 μl diluted DNA solution was transferred to 15 μl diluted Lipofectamine® 2000 solution, and

mixed well, but gently by pipetting. Dilutions were prepared to give the desired μg of DNA and ratios of Lipofectamine® 2000 : DNA as presented in table 2. The mix of DNA and Lipofectamine® 2000 was incubated for 5 min at room temperature. The 30 μl mix was then added to the 300 μl of culture medium in a well of cells cultured in 8-well μ-Slides. The well plate was carefully tilted back and forth for mixing. Cells were further incubated as usual at 37 °C with 5% CO_2. Successfulness of transfection was analysed 24 hours and 48 hours after transfection on a confocal microscope (Leica TCS SP8). Each transfection protocol was performed in singlet.

Real-time imaging of RGD-RHO-NE incubation with transfected cells
As an initial test experiment, real-time imaging of NE incubation was performed with one well of transfected cells. Cells were then treated as described in 3.4.2 for cells with no cell staining. This experiment was performed on cells transfected with 0.05 μg of DNA and a Lipofectamine® 2000 : plasmid DNA ratio of 0.5:1, 48 hours after transfection. RGD-RHO-NE were used for NE incubation.

3.4.4 Confocal microscopy imaging

The confocal laser scanning microscope Leica TCS SP8 was utilised for imaging in all microscopy experiments described above. The microscope was connected and run through the software LAS X. For live cells in 8-well μ-Slides, imaging was performed at 37°C and the samples were placed in a chamber which was supplemented with an air flow of 5% CO_2. Fixed cells in 8-well Nunc™ Lab-Tek™ II Chamber Slides™ sealed with a cover glass, were imaged at room temperature and without CO_2. The pinhole size was 1 airy unit for all experiments. The scan speed and frame size, as well as zoom factor if not stated as constant, varied between images and experiments. For all samples, a bright field image was captured by illuminating the sample with a laser of wavelength between 500 nm and 550 nm, and detecting the image with a photomultiplier tube in transmission mode with a bandpass filter of 500 - 550 nm in front.

Optimisation of fixation protocol, and investigation of successful transfection
Samples from the experiments of optimisation of fixation protocol and when investigating successfulness of transfection, were imaged with a 20x/0.75 dry objective. Laser intensitites, as well as detector gain and offset were adjusted for each image to achieve maximum signal with minimum saturation and background noise. For optimisation of fixation protocol, fixed samples were excited by three lasers in a sequantial scan due to overlap of excitation and emission spectra; The nuclear stain DAPI was excited with a laser at 405 nm and emission was detected at 435 - 498 nm, a white light laser (WLL) at 545 nm was used to obtain the bright field image, and RHO-NE were excited by a WLL at 560 nm and emission was detected at 585 - 650 nm. Live cells from the same experiment (imaged for comparison to fixed cells), were simultaneously illuminated by two lasers; a WLL at 508 nm was used to obtain the bright field image and a WLL at 560 nm was used to excite RHO-NE. Emission from RHO-NE was detected at 575 -

644 nm. To assess successfulness of transfection, samples were simultaneously illuminated by two lasers; a WLL at 505 nm was used to obtain the bright field image and a WLL at 480 nm was used to excite TurboGFP. TurboGFP emission was detected at 515 - 778 nm.

Real-time imaging of NE-incubation

Real-time imaging of cells incubated with NE was performed with a 63x/1.20 water objective. Images were taken every 30th second and each incubation was imaged for a total time of 30 min. To remain in the same z-position throughout the time-series, the autofocus system Adaptive Focus Control was activated. As laser exposure may cause stress to cells [87], especially when exposed for a longer period of time, the laser intensities utilised were kept constant in all similar experiments to assure the same conditions for all cells. For the same reason, the zoom factor and line average was also kept constant at repectively 0.75 and 1. Detector gain and offset were adjusted for each time series to achieve maximum signal with minimum saturation and background noise. Laser excitation wavelengths and intensities, as well as emission detection intervals for the different experiments is presented below (A - D). In some experiments, cells were imaged with a 20x/0.75 dry objective after the real-time imaging was terminated. The laser and detector settings were then the same as presented below.

A: No cell staining

For real-time imaging of 'clean' cells (cells with no cell staining) incubated with NE, a bright field image and an image of the rhodamine-PE or Nile Red 668 fluorescence was captured. For incubation with RHO-NE, a WLL at 508 nm with intensity 7.73 % was used to obtain the bright field image, and a WLL at 560 nm with intensity 11.74 % was used to excite rhodamine-PE. Rhosamine-PE emission was detected at 580 - 644 nm. The images were captured simultaneously. For incubation with NR-NE, a WLL at 525 nm with intensity 10.84 % was used both to excite Nile Red 668 and to obtain the bright field image. Nile Red 668 emission was detected at 550 - 650 nm. The frame size was 512×512 pixels and the scan speed was set to 200 Hz.

B: Cells stained with Hoechst nuclear stain and CellMask™ plasma membrane stain

For real-time imaging of cells stained with Hoechst and CellMask™, a bright field image, an image of the Hoechst fluorescence, an image of the CellMask™ fluorescence and an image of the rhodamine-PE fluorescence was captured. A laser at 405 nm with intensity 3 % was used to excite Hoechst, and emission was detected at 430 - 480 nm. A WLL at 520 nm with intensity 2.70 % was used to obtain the bright field image. A WLL at 560 nm with intensity 16.17 % was used to excite rhodamine-PE and emission was detected at 580 - 629 nm. A WLL at 649 nm was used to excite CellMask™ and emission was detected at 676 - 800 nm. All four images were captured simultaneously. The frame size was 1024×1024 pixels and the scan speed was set to 200 Hz.

C: Cells stained with Hoechst nuclear stain and Calcein AM cytoplasm stain

For real-time imaging of cells stained with Hoechst and Calcein AM, an image of the Hoechst fluorescence, an image of the Calcein AM fluorescence and an image of the rhodamine-PE fluorescence was captured. A laser at 405 nm with intensity 3 % was

used to excite Hoechst, and emission was detected at 410 - 480 nm. A WLL at 496 nm with intensity 1.21 % was used to excite Calcein AM and emission was detected at 506 - 545 nm. A WLL at 560 nm with intensity 16.20 % was used to excite rhodamine-PE and emission was detected at 580 - 700 nm. The three images were captured in a sequential scan due to excitation and emission spectra overlap. The frame size was 1024×1024 pixels and the scan speed was set to 200 Hz. The one experiment where cells were only stained with Hoechst, laser and detector settings were as described here, except the laser and detector for Calcein AM was not included.

D: Cells transfected with GFP-tagged β_3 integrin
For real-time imaging of cells transfected with GFP-tagged β_3 integrin, a bright field image, an image of the TurboGFP fluorescence and an image of the rhodamine-PE fluorescence was captured. A WLL at 480 nm with intensity 61,34% was used to excite TurboGFP and emission was detected at 510 - 652 nm. A WLL at 550 m was used to excite rhodamine-PE and to obtain the bright field image. Rhodamine-PE emission was detected at 580 - 700 nm. The images were captured in a sequential scan due to excitation and emission spectra overlap. The frame size was 1024×1024 pixels and the scan speed was set to 200 Hz. The zoom factor was increased from 0.75 in this experiment.

3.5 Data analysis

3.5.1 Flow cytometry data analysis

The data from flow cytometric measurements were analysed using Kaluza Flow Cytometry Analysis v1.2 (Beckman Coulter) software to determine the percentage of positive cells (fluorescent cells) and the relative median fluorescence intensity (MFI) for each sample. Cellular fragments, debris and agglomerations were excluded from the analysis by gating the SS versus the FS plot (illustrated in appendix A, figure 53). For the gated cells, a histogram was then created showing the cell count as a function of logarithmic fluorescence intensity. Histogram overlays including the autofluorescent sample were made, and a boundary line was set to approximately 3% positive cells in the autofluorescent sample to exclude autofluorescence from the results (illustrated in appendix A, figure 54). For the histogram as a whole and for the population of cells with higher fluorescence intensity than the set boundary line, the percentage of cells making up the population and the population's median fluorescence intensity was read out by the software. The percentage of positive cells for the relevant fluorophore was determined as the percentage of cells in the population with higher fluorescence intensity than the set boundary line. Relative MFI was determined from the data for MFI for the whole cell population. Relative values were determined by normalising the MFI for each sample towards the MFI of the autofluorescent sample. In experiments with cells of different confluency, the values for relative MFI were further normalised towards the highest value in each data series. This was to easily visualise the relative change in MFI with higher cell confluency for both surface expression of $\alpha_v\beta_3$-integrin and uptake of NE.

Values for percentage of positive cells and relative MFI are presented in line graphs made in Microsoft Excel. The number of parallels performed is stated in each figure

legend. Most experiments were performed twice (n = 2). Therefore, results are not presented as average values with standard deviations, but rather as figures showing either one representative data series, or all data series performed.

For experiments where NE fluorescence was detected, relative MFI and percentage of positive cells generally showed the same trends. Therefore, only data for relative MFI are presented (except in one experiment). Relative MFI was chosen over percentage of positive cells, because this parameter measures the amount of NE uptake, which is the parameter most interesting for these studies. Also, at some point, in experiments with high payloads of fluorophores in NE and long incubation times, 100% positive cells may be obtained for all samples, while the MFI may still differ. This was the situation for experiments detecting labelled secondary antibody fluorescence. $\sim$ 100% positive cells was generally found for all samples, and only relative MFI presented.

3.5.2 Image analysis

CLSM software
The CLSM software LAS X was used to export the images from the confocal laser scanning microscope Leica TCS SP8. The LAS X software was also used to add colour to the fluorescent signals in the images. Where several image channels were recorded, different colours were added to different channels. The colours chosen in each experiment is presented in the relevant figure legends.

Fiji / ImageJ
Fiji (Fiji is Just ImageJ, a distribution of ImageJ focused on life sciences) was used to adjust colour brightness and contrast in the images. Brightness and contrast were adjusted to make the interesting features as clear as possible, and simultaneously avoid too much noise in the images. For images presented from 30 min time series of real-time imaging of NE incubation, the brightness and contrast was first adjusted for the timeseries as a whole. Then snapshots were extracted from the time series for presentation in the report. In this manner, all images from the same time series have the same adjustments for brightness and contrast compared to the original file. Fiji was also utilised to add scalebars to the images, and to merge seperate fluorescence image channels into one image.

4 Results

4.1 Introduction to experiments with flow cytometry

An important notion when analysing results in this section, is that the *trend* of results are more interesting than the absolute values of relative MFI and percentage of positive cells. This is because there are batch-to-batch variations in cell confluency, payload of fluorophores in NE, etc. This may affect the absolute values of results, but the result for one data point compared to another in the same data series, should stay relatively similar.

4.2 Studies of fluorophore leakage

By comparing two incubation periods at 4°C, no fluorophore leakage for RAD-NE and a potential small leakage for RGD-NE was observed for both RHO- and NR-NE. For RAD-NE, both percentage of positive cells and relative MFI were very similar for 15 min and 60 min incubation. For RGD-NE, however, a small increase in both relative MFI (from 2.0 to 2.5 for NR-NE and 1.8 to 2.4 for RHO-NE) and percentage of positive cells (from 25% to 37% for NR-NE and 16% to 30% for RHO-NE) were observed. Figure 15 shows both relative MFI and percentage of positive cells for incubation with NR- and RHO-NE. Also, to visualise the cellular fluorescence intensity distributions of the samples producing the graphs of figure 15, raw data from one of the graphs are presented in figure 16.

As a comparison to the extent of potential leakage, extent of NE uptake during the same incubation periods were studied at 37°C. The relative MFI for samples incubated with RGD-NE at 37°C, increased from 3.0 to 6.5 for NR-NE, and 5.0 to 14.2 for RHO-NE. The percentage of positive cells for RGD-NE at 37°C, increased from 50% to 84% for NR-NE and from 81% to 96% for RHO-NE (data not shown).

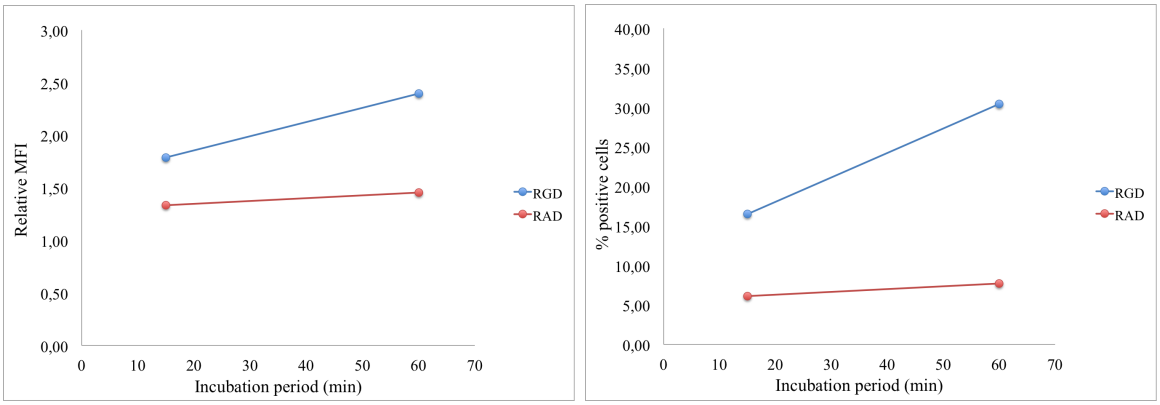

(a) RHO-NE

(b) RHO-NE

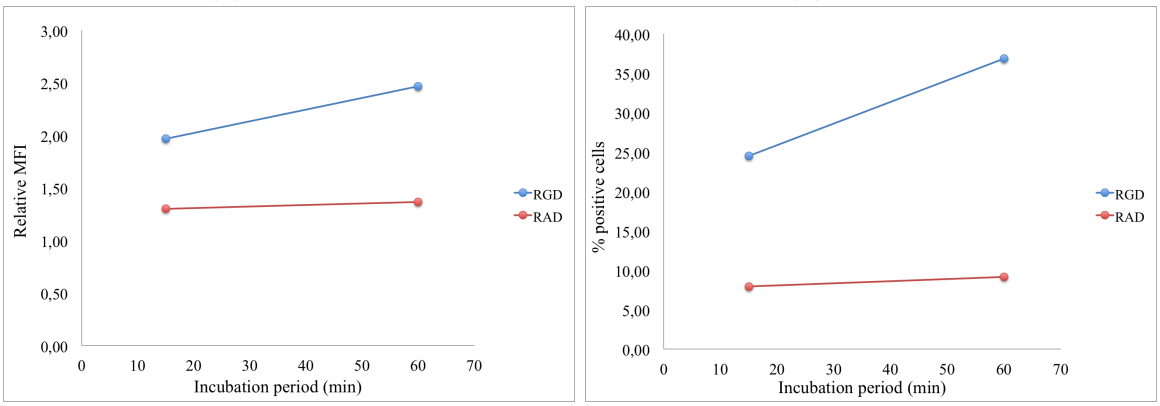

(c) NR-NE

(d) NR-NE

Figure 15: **Leakage studies** Relative MFI of rhodamine-PE or Nile Red 668-fluorescence, and percentage of positive cells, for HUVEC incubated with RHO-NE or NR-NE at 4°C, for 15 min and 60 min. NE were conjugated to targeting RGD or non-targeting RAD peptide. Each data point represent a single sample (n = 1).

From raw data to line graphs The raw data for RHO-NE at 4°C presented in figure 16, displays a histogram overlay with the results from an autofluorescent sample, in addition to NE-incubated samples. A description of how data for relative MFI and percentage of positive cells are determined from such plots, may be found in appendix A.

As seen in figure 16, the histograms for samples incubated with RAD-NE for 15 and 60 min, lie very close to each other, and sligtly right-shiftet relative to the autofluorescent sample. Samples incubated with RGD-NE, are further right-shiftet compared to RAD-samples, with incubation for 60 min giving higher intensities than 15 min. Even though shifts in fluorescence intensity for the cell populations are observed, these shifts are not very large. The percentage of cells counted as positive, was 30% at the highest.

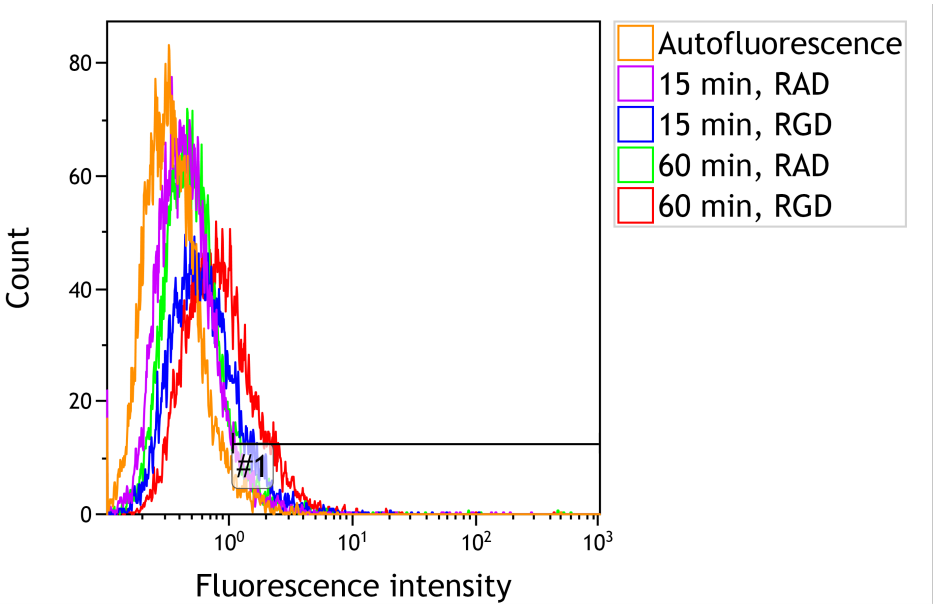

Figure 16: **Raw data** Example of a histogram overlay from flow cytometry measurements. An autofluorescent sample, and samples incubated with RGD- and RAD-RHONE for 15 and 60 min at 4°C are shown. Relative MFI and percentage of positive cells presented in figure 15a and b are extracted from these raw data.

4.3 Saturation studies of RGD-to-surface-$\alpha_v\beta_3$ binding

From experiments where cells were incubated with different concentrations of NE for 2.5 min, saturation binding was observed for concentrations above 0.1 mM for RGD-NE. The fluorescence intensity steeply increased up to 0.1 mM NE, then levelled off for all parallels performed. For RAD-NE, no saturation kinetics were observed. The fluorescence intensity in samples incubated with 1 μM - 0.1 mM RAD-NE-solutions, was no higher than the fluorescence intensity in the autofluorescent sample, causing a relative MFI equal to 1. For larger RAD-NE concentrations, a slow, linear increase in fluorescence intensity with increasing concentration of NE was observed. The results for relative MFI are presented in figure 17. The results for percentage of positive cells showed the same trend as relative MFI, and are not presented.

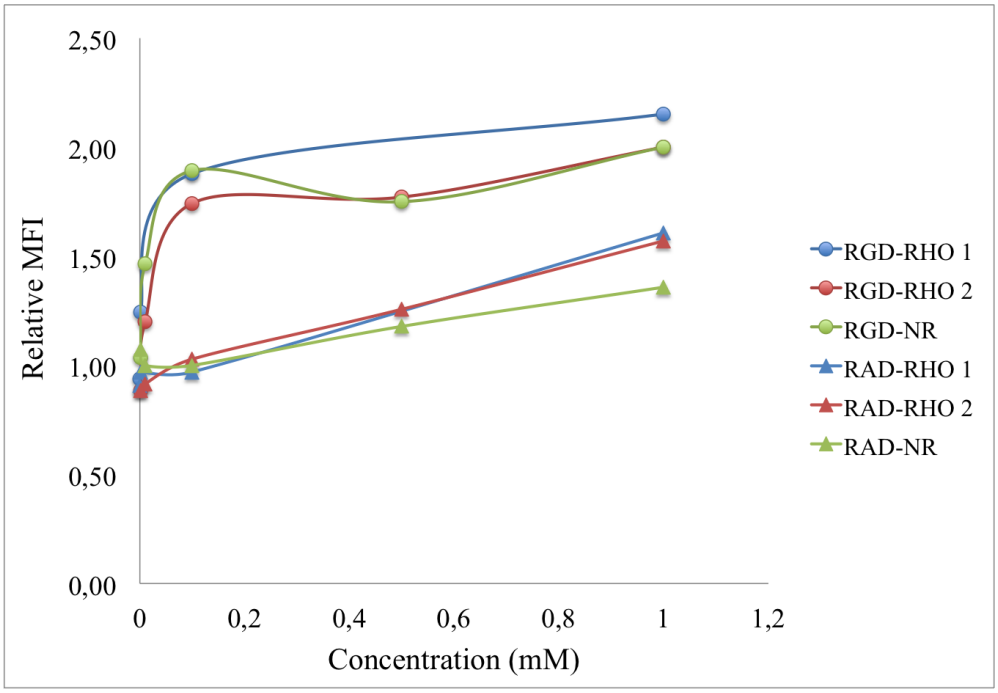

Figure 17: **Saturation studies** Relative MFI of rhodamine-PE or Nile Red 668 fluorescence as a function of NE concentration, for HUVEC incubated with RHO-NE (n = 2) or NR-NE (n = 1) for 2.5 min at 37°C. NE were conjugated to targeting RGD or non-targeting RAD peptide. All three data series are shown and each data point represent a single sample. Samples marked with the same colour (and number), were performed simultaneously. RGD- and RAD-RHO 1 were performed with one less data point than the other samples (0.5 mM NE-solution).

4.4 Incubation pause experiments

For all experiments in this section, the percentage of positive cells and relative MFI showed the same trend, thus only relative MFI is presented. Further, all parallels performed are presented for each experiment, to visualise variations. For all except experiments with 0.1 mM NR-NE, samples incubated with NE for only 4 min were included, for comparison to incubation pause samples. Samples marked with the same number in the figures, were performed simultaneously, making their values for MFI possible to compare.

4.4.1 Experiments with labelled NE in both NE-incubation periods

From experiments where cells were incubated with fluorescently labelled NE in both incubations, a small increase in fluorescence intensity with increasing incubation pause was observed for 1 mM RGD-RHO-NE. With the exception of one data point in each data series, the relative MFI increased for each increase in incubation pause length. For 1 mM RAD-RHO-NE, no clear effect of the pause length was observed (Figure 18). For 0.1 mM RHO-NE, no clear effect of the pause length was observed for either RGD- or RAD-NE, when analysing only the same data points as the other incubation pause experiments (no 0 min pause, figure 19a). When including results for 0 min pause, a small increase in RGD-NE fluorescence intensity was observed from 0 - 3 min or 0 - 6 min incubation pause for the two parallels performed (Figure 19b). For NR-NE, no clear effect of the pause length was observed for either RAD- or RGD-NE, both at concentration 0.9 mM (Figure 20) and 0.1 mM (Figure 21).

For RGD-RHO-NE at 1 mM concentration (Figure 18), the highest relative MFI observed (for cells with 15 min incubation pause), was approximately twice the relative MFI observed for 4 min incubation. Experiments with 0.1 mM RHO-NE, were the only incubation pause experiments which included samples of 0 min pause (8 min continuous NE-incubation). To easily compare results with other incubation pause experiments, as well as compare results for 4 min and 8 min incubation, results were presented in two plots - one for each purpose (Figure 19a and 19b, respectively). When comparing results for 4 min and 8 min incubation periods, it was found that cells incubated for 8 min, showed 24 - 30% higher fluorescence intensities than cells incubated for 4 min.

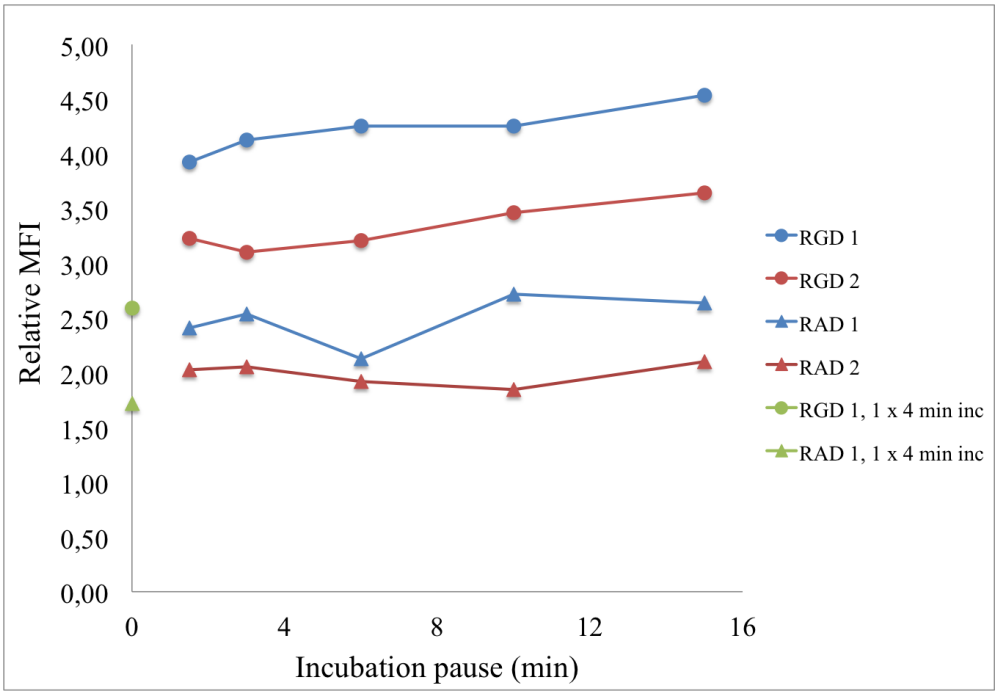

Figure 18: **RHO-NE in first and second incubation period, 1 mM** Relative MFI of rhodamine-PE fluorescence for HUVEC incubated with RHO-NE (1 mM) for two periods of 4 min, separated by an incubation pause of varying length (n = 2). Samples named 1 x 4 min inc, were incubated with NE for only 4 min (n = 1). NE were conjugated to targeting RGD or non-targeting RAD peptide. Each data point represent a single sample. Samples marked with the same number, were performed simultaneously.

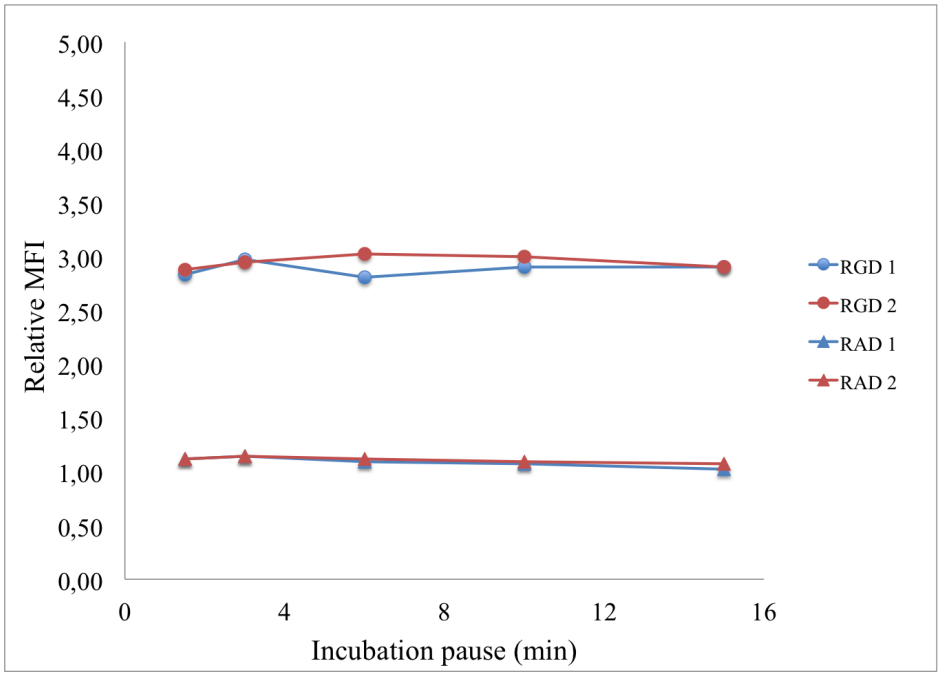

(a) Results as presented for other incubation pause experiments (without 0 min pause)

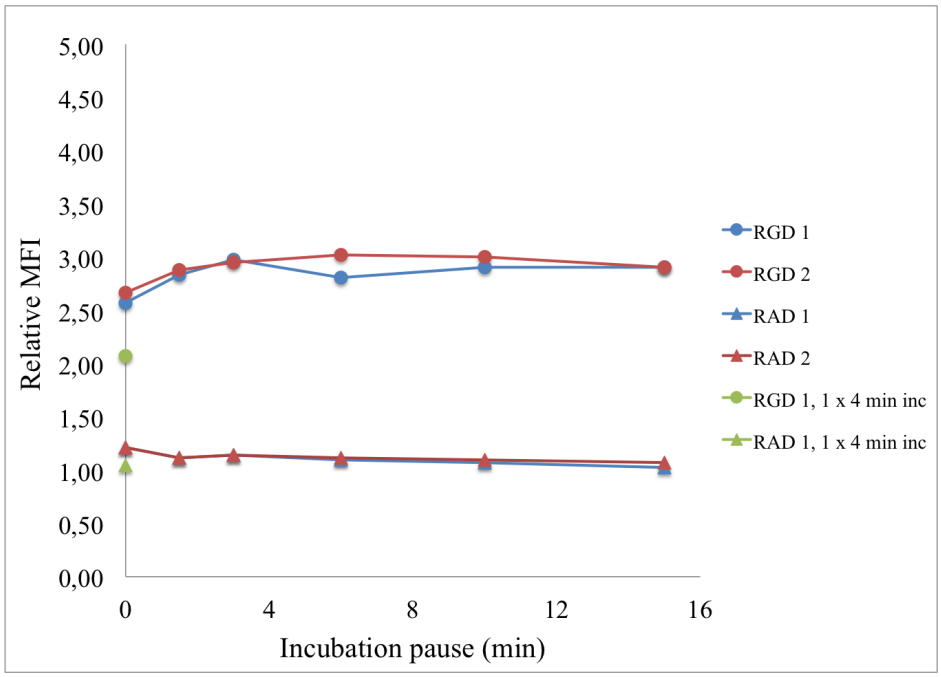

(b) Results from all samples performed

Figure 19: **RHO-NE in first and second incubation period, 0.1 mM** Relative MFI of rhodamine-PE fluorescence for HUVEC incubated with RHO-NE (0.1 mM) for two periods of 4 min, separated by an incubation pause of varying length (n = 2). Samples named 1 x 4 min inc, were incubated with NE for only 4 min (n = 1). NE were conjugated to targeting RGD or non-targeting RAD peptide. Each data point represent a single sample. Samples marked with the same number, were performed simultaneously.

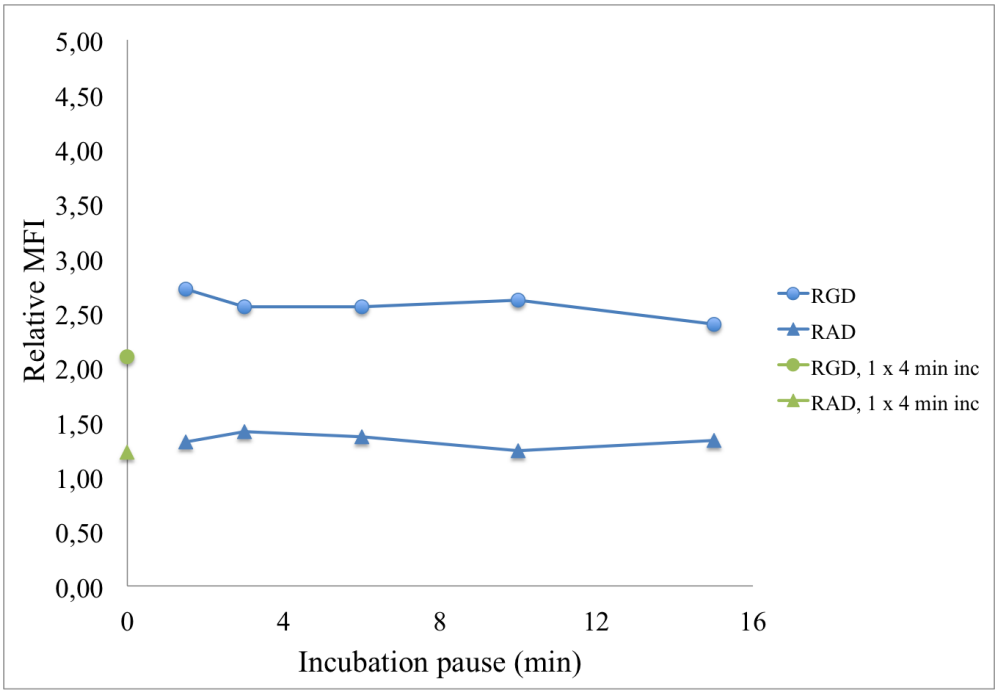

Figure 20: **NR-NE in first and second incubation period, 0.9 mM** Relative MFI of Nile Red 668-fluorescence for HUVEC incubated with NR-NE (0.9 mM) for two periods of 4 min, separated by an incubation pause of varying length (n = 1). Samples named 1 x 4 min inc, were incubated with NE for only 4 min (n = 1). NE were conjugated to targeting RGD or non-targeting RAD peptide. Each data point represent a single sample. All samples were performed simultaneously.

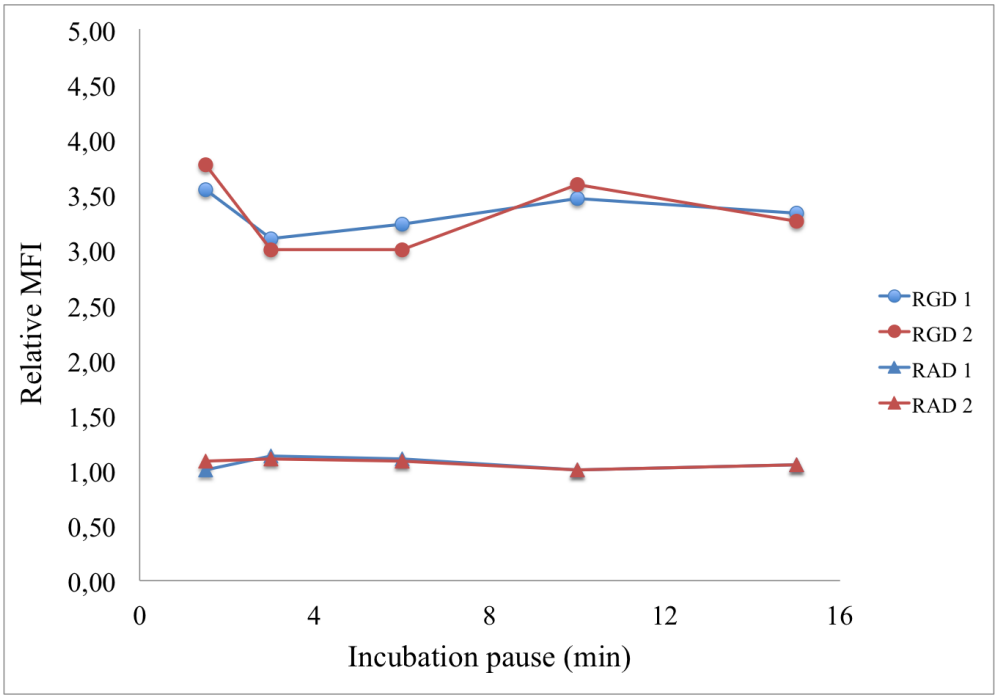

Figure 21: **NR-NE in first and second incubation period, 0.1 mM** Relative MFI of Nile Red 668-fluorescence for HUVEC incubated with NR-NE (0.1 mM) for two periods of 4 min, separated by an incubation pause of varying length (n = 2). NE were conjugated to targeting RGD or non-targeting RAD peptide. Each data point represent a single sample. Samples marked with the same number, were performed simultaneously.

4.4.2 Experiments with unlabelled NE in first and labelled NE in second NE-incubation period

From experiments with incubation with 1 mM or 0.9 mM UL-NE prior to incubation with either 1 mM RHO-NE (Figure 22) or 0.9 mM NR-NE (Figure 23), an overall small decrease in fluorescence intensity with increasing pause length was observed for RGD-NE, for all parallels performed. Also for RAD-NE, a small decrease in relative MFI with increasing pause length was observed for most samples, while 'RAD 4' in figure 22b showed very little effect of pause length. The decrease observed for RAD-NE was smaller than for RGD-NE. Samples only incubated with RHO-NE or NR-NE for 4 min, showed similar values for relative MFI as incubation pause samples.

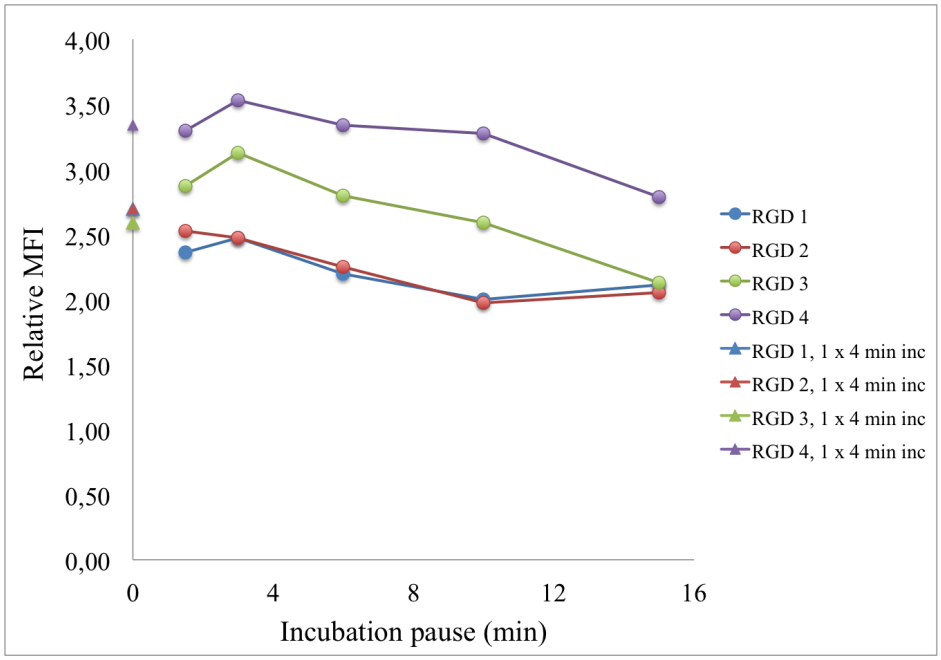

(a)

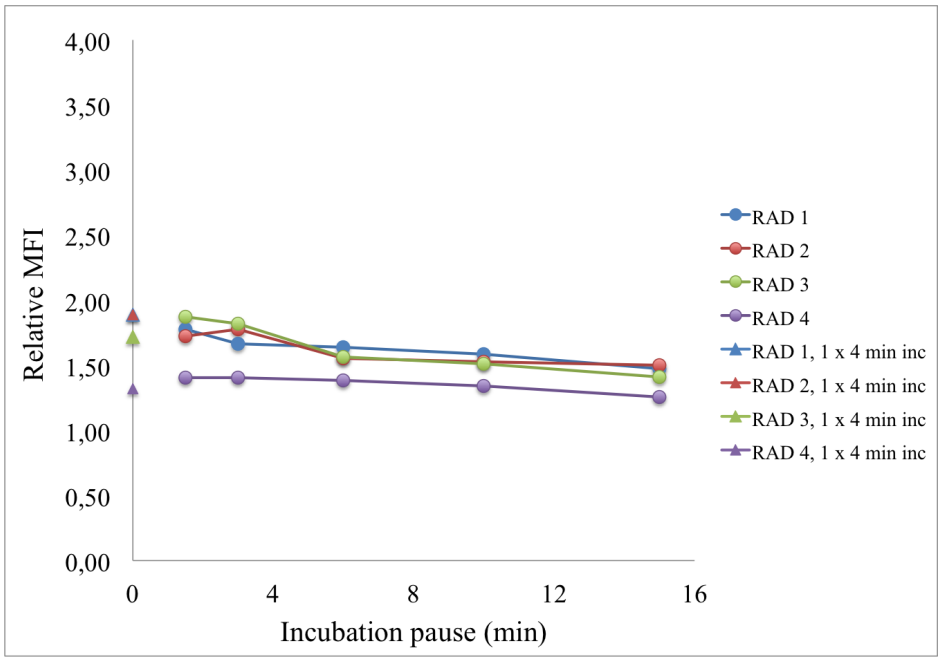

(b)

Figure 22: **UL-NE in the first and RHO-NE in the second incubation period, 1 mM** Relative MFI of rhodamine-PE fluorescence for HUVEC incubated with UL-NE (1 mM) for 4 min, then RHO-NE (1 mM) for 4 min, separated by an incubation pause of varying length (n = 4). Samples named 1 x 4 min inc, were only incubated with RHO-NE for 4 min (n = 4). NE were conjugated to (a) targeting RGD or (b) non-targeting RAD peptide. Each data point represent a single sample. Samples marked with the same colour and number, were performed simultaneously.

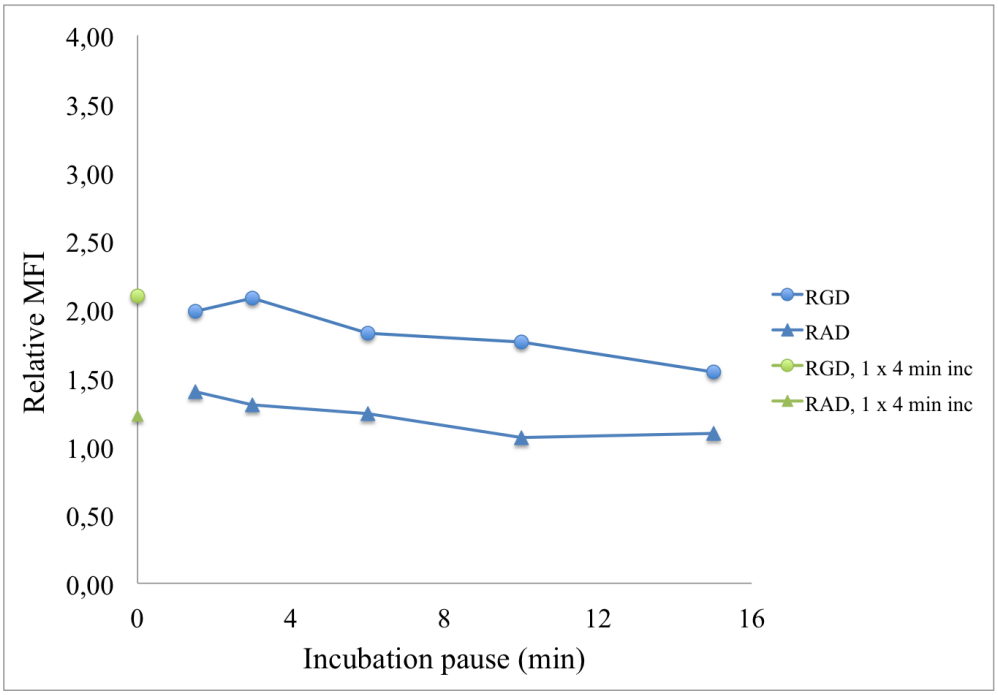

Figure 23: **UL-NE in the first and NR-NE in the second incubation period, 0.9 mM** Relative MFI of Nile Red 668-fluorescence for HUVEC incubated with UL-NE (0.9 mM) for 4 min, then NR-NE (0.9 mM) for 4 min, separated by an incubation pause of varying length (n = 1). Samples named 1 x 4 min inc, were incubated with NE for only 4 min (n = 1). NE were conjugated to targeting RGD or non-targeting RAD peptide. Each data point represent a single sample. All samples were performed simultaneously.

4.4.3 Experiments with labelled NE in first and unlabelled NE in second NE-incubation period

From experiments where samples were incubated with 1 mM RHO-NE prior to 1 mM UL-NE (Figure 24), a small increase in fluorescence intensity with increasing pause length was observed for RGD-NE. Although the difference between 1.5 min and 15 min pause is small for the parallel 'RGD 2' in figure 24, the data series show a clear trend of increase when disregarding the first data point (1.5 min pause). For RAD-NE, no clear effect of pause length was observed. For RGD-NE, samples only incubated with RHO-NE for 4 min, show higher values for relative MFI than incubation pause samples. For RAD-NE, values lie at similar relative MFI.

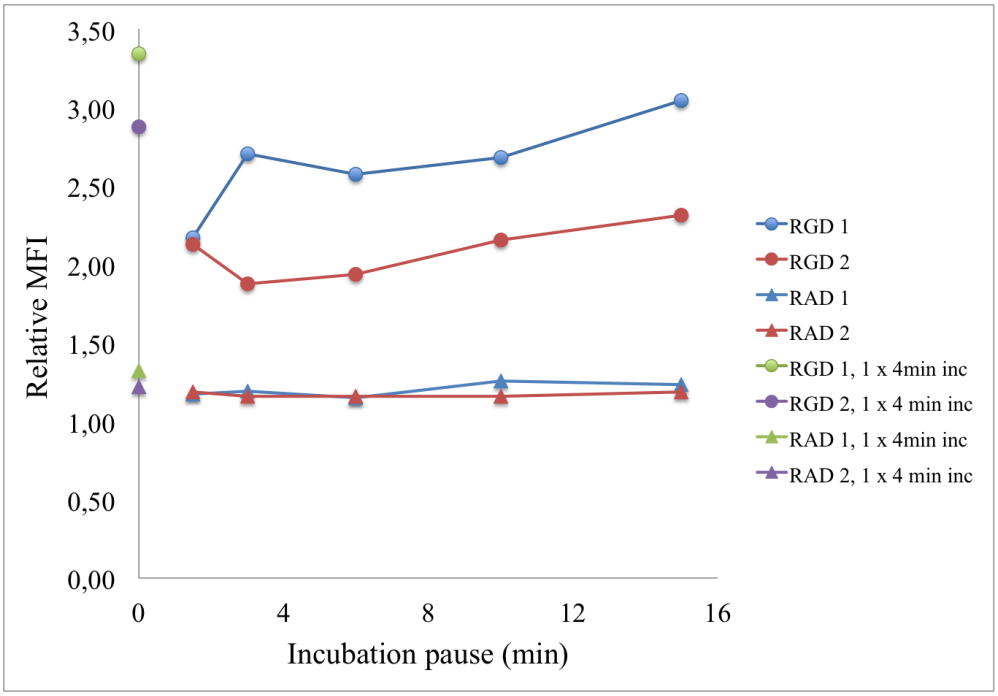

Figure 24: **RHO-NE in the first and UL-NE in the second incubation period, 1 mM** Relative MFI of rhodamine-PE fluorescence for HUVEC incubated with RHO-NE (1 mM) for 4 min, then UL-NE (1 mM) for 4 min, separated by an incubation pause of varying length (n = 2). Samples named 1 x 4 min inc, were only incubated with RHO-NE for 4 min (n = 2). NE were conjugated to targeting RGD or non-targeting RAD peptide. Each data point represent a single sample. Samples marked with the same number, were performed simultaneously.

4.5 Introductory studies for immunolabelling of surface $\alpha_v\beta_3$-integrins

The results from experiments testing three different cell detachment methods after immunolabelling of surface $\alpha_v\beta_3$-integrins, is found in figure 25. Samples detached by EDTA and trypsin showed very similar fluorescence intensity distributions. The sample detached by trypsin was slightly right-shifted compared to EDTA, with an MFI of 18.71 compared to 15.55 for EDTA. Both samples easily counted 10 000 cells within 5 minutes. On the contrary, for samples detached by scraping, the cell count was very low. In addition, the few entities counted were positioned at small forward scatter (FS) values compared to samples detached by trypsin and EDTA in the plot of FS vs. count (data not shown).

In experiments testing saturation binding of surface $\alpha_v\beta_3$-integrins, no difference in flow cytometry histograms of the cell populations incubated with 0.3μg/100μl and 1μg/100μl of primary antibody was observed (Figure 26).

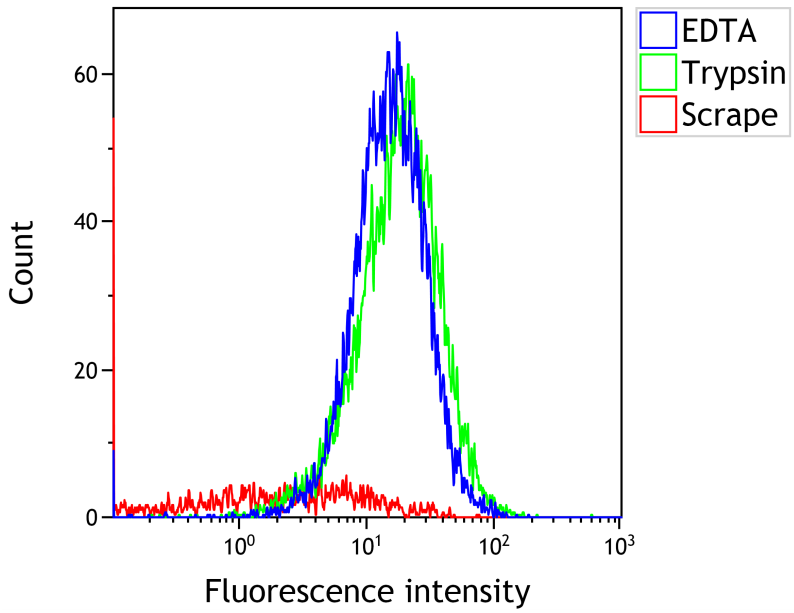

Figure 25: **Comparison of three cell detachment methods** A histogram overlay from flow cytometry measurements presenting the results for surface labelling of $\alpha_v\beta_3$-integrins after cell detachment by either EDTA, trypsin or scraping. Adherent HUVEC were immunolabelled prior to detachment, and histograms show secondary antibody fluorescence as a function of cell count. Histograms show results from one representative experiment (n=2).

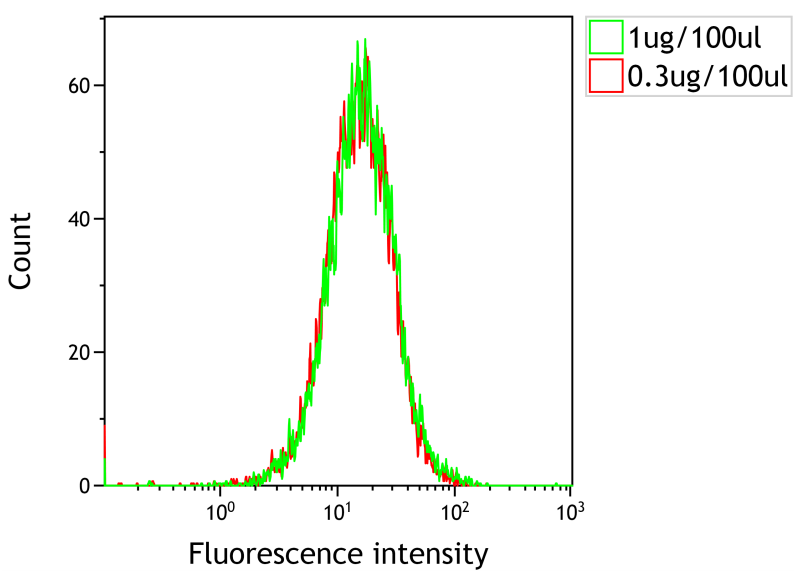

Figure 26: **Assuring saturation binding of primary antibody** A histogram overlay from flow cytometry measurements presenting the results for surface labelling of $\alpha_v\beta_3$-integrins when two different concentrations of primary antibody were utilised. The histograms show secondary antibody fluorescence as a function of cell count. Histograms show results from one representative experiment (n=2).

4.6 Expression of surface $\alpha_v\beta_3$-integrins after incubation with nanoemulsions

In these experiments, all samples showed approximately 100% positive cells, and values for relative MFI are presented. Experiments in figure 27b were performed simultaneously with the same cell densitites and NE batches, making their values for relative MFI possible to compare.

From experiments where cells were immunolabelled immediately after NE-incubation (Figure 27a), the surface expression of $\alpha_v\beta_3$-integrins in HUVEC showed a decrease with increasing incubation period for RGD-NE. For 30 min incubation period, 15 - 25% decrease in $\alpha_v\beta_3$-surface expression was observed. For RAD-NE, varying, but not an overall reducing $\alpha_v\beta_3$ surface expression was observed for one parallel ('RAD 1'). For the other parallel ('RAD 2'), a reduction in surface expression of 11% (compared to 25% for 'RGD 2') was observed with increasing incubation period. Interestingly, for both parallels, the surface expression of $\alpha_v\beta_3$ after 5 min NE incubation, was similar for incubation with RGD- and RAD-NE.

From experiments where cells were immunolabelled 20 min after NE-incubation, the surface expression of $\alpha_v\beta_3$-integrins was surprisingly lower than immediately after incubation. This was observed for both incubation with RAD- and RGD-NE. Labelling immediately after and 20 min after NE-incubation performed the same day, are plotted together in figure 27b for comparison. 20 min after NE-incubation, both RAD- and RGD-NE show a trend of fast reduction in surface expression from 0 - 5 min incubation. For longer incubation periods, by disregarding the data point at 10 min RAD-NE incubation, the reduction in $\alpha_v\beta_3$ surface expression tend to level off.

Control samples Control samples to test unspecific binding of secondary antibodies and to test possible bleedthrough of rhodamine emission in the detection of secondary antibody fluorescence, both showed very similar fluorescence intensity distributions as the autofluorescent sample.

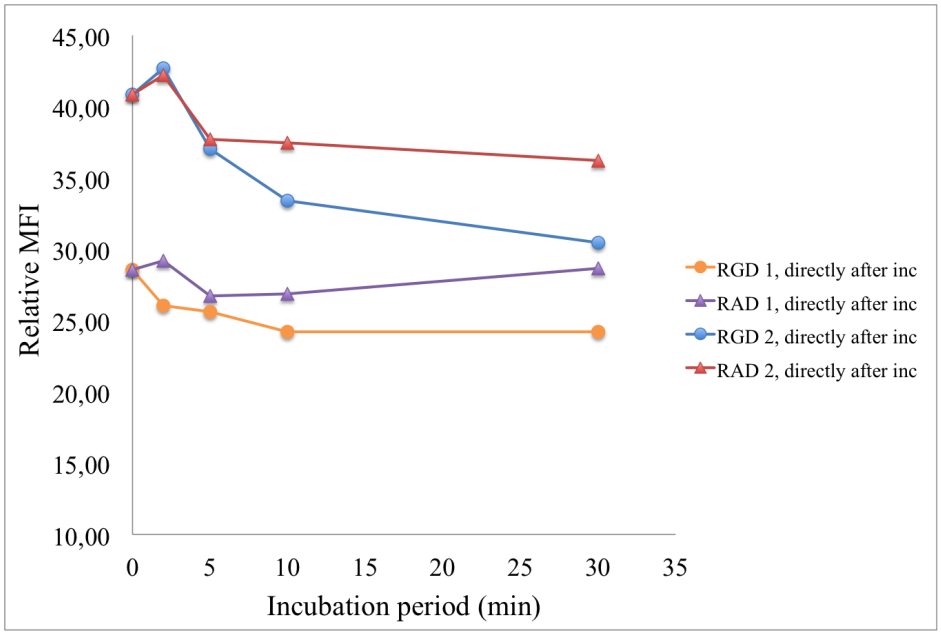

(a) $\alpha_v\beta_3$ surface expression immediately after NE-incubation

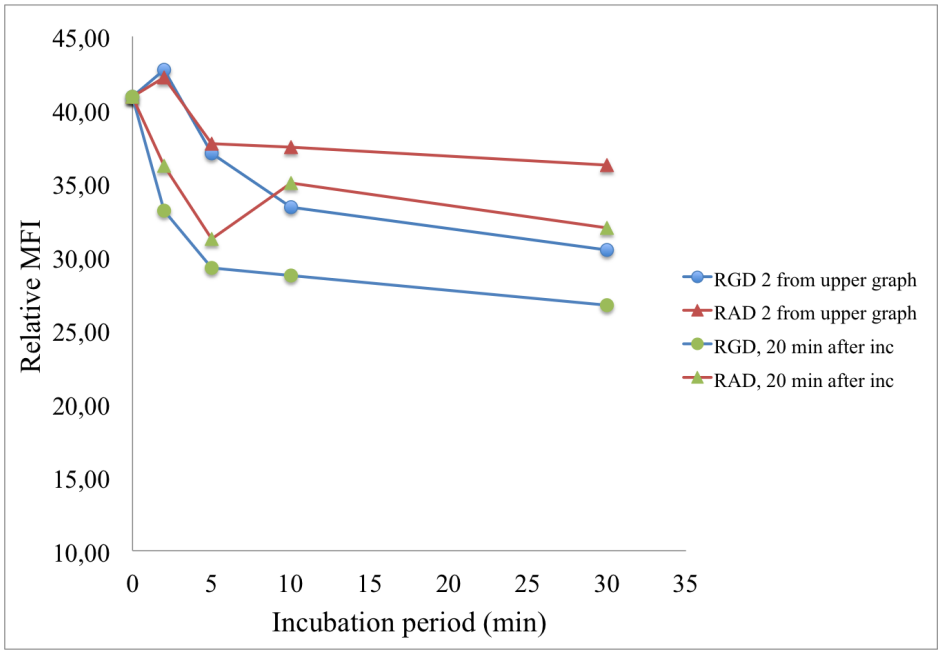

(b) Comparison of $\alpha_v\beta_3$ surface expression immediately and 20 min after NE-incubation

Figure 27: **Expression of surface $\alpha_v\beta_3$-integrin after incubation with nanoemulsions** Relative MFI of secondary antibody fluorescence for HUVEC incubated with RHO-NE (1 mM) for different periods, prior to immunolabelling of surface $\alpha_v\beta_3$-integrins. Cells were either labelled immediately (n = 2) or 20 min (n = 1) after NE-incubation. NE were conjugated to targeting RGD or non-targeting RAD peptide. RGD 2 and RAD 2 in (a) are plotted again in (b) for comparison to labelling 20 min after NE-incubation.

4.7 Experiments with cells of different confluency

4.7.1 Expression of surface $\alpha_v\beta_3$-integrins on cells of different confluency

From immunolabelling experiments, a clear trend of reduction in surface expression of $\alpha_v\beta_3$-integrins was observed with increasing cell confluency. Relative MFI and percentage of positive cells for samples seeded at cell density 10 000 - 80 000 and 10 000 - 100 000 cells/well, 3 and 4 days after seeding, are presented in figure 28. Values are normalised towards the highest value in each data series. From lowest to highest cell confluency, relative MFI decreased 24% and 27%, 3 and 4 days after seeding, respectively. 3 days after seeding, $\sim$ 100% positive cells were found for all samples, while 4 days after seeding, percentage of positive cells gradually decreased from 100% to 93% from the lowest to the highest cell confluency.

Control samples to test unspecific binding of the secondary antibody, showed very similar fluorescence intensity distributions as the autofluorescent sample.

4.7.2 Uptake of nanoemulsions in cells of different confluency

From experiments with NE-incubation of cells of different confluency, a reduction in NE uptake was observed with increasing cell confluency for incubation with RGD-NE, while no effect of confluency was observed on uptake of RAD-NE. Figure 29 shows the uptake of NE in samples seeded at cell density 10 000 - 100 000 cells/well, 4 days after seeding. Results are shown as relative MFI, and values are normalised towards the highest value of the data series. Percentage of positive cells showed the same trends as relative MFI, and is not presented. For RGD-NE, the relative decrease in uptake of NE with increasing confluency, was highly similar to the relative decrease in $\alpha_v\beta_3$ surface expression for the same cell confluencies (4 days after seeding), presented in figure 28a.

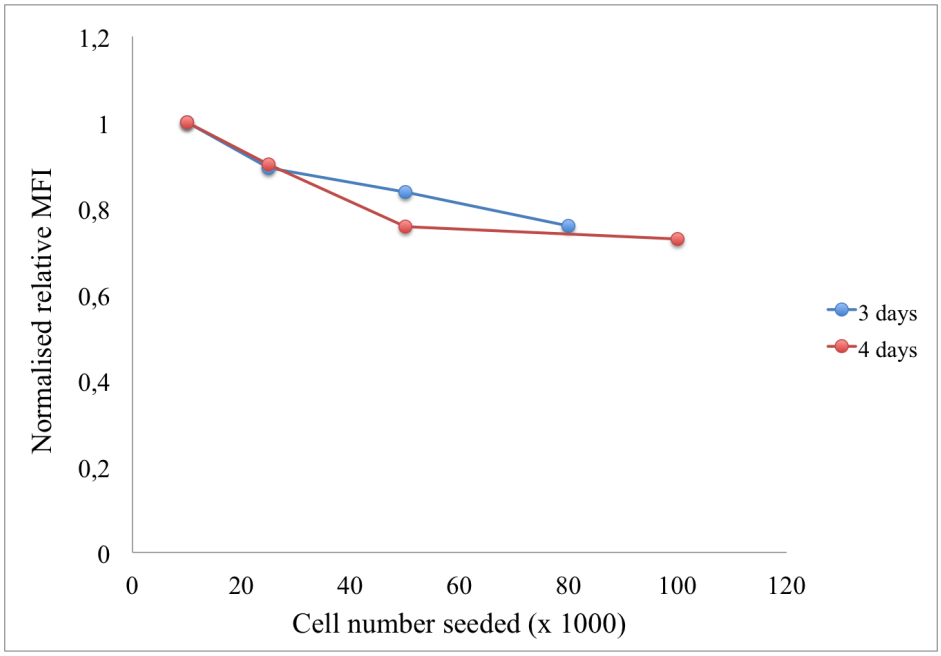

(a)

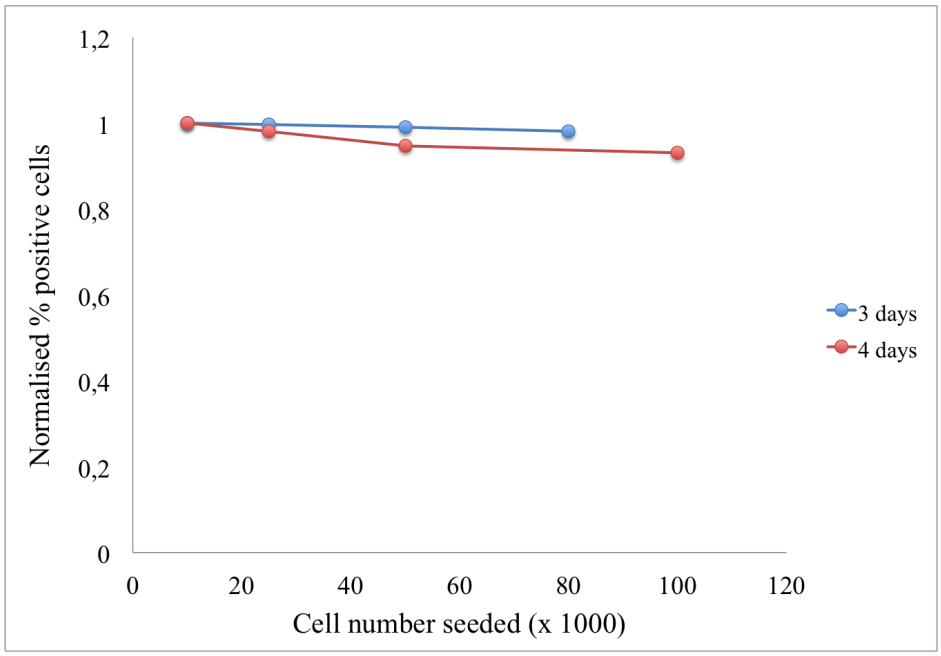

(b)

Figure 28: **Expression of surface $\alpha_v\beta_3$-integrin on cells of different confluency** (a) Relative MFI of secondary antibody fluorescence and (b) percentage of positive cells for HUVEC immunolabelled on ice for detection of surface $\alpha_v\beta_3$-integrins. Cells were seeded at different cell densities, 3 or 4 days prior to immunolabelling. One representative data series is presented for each experiment (n = 2).

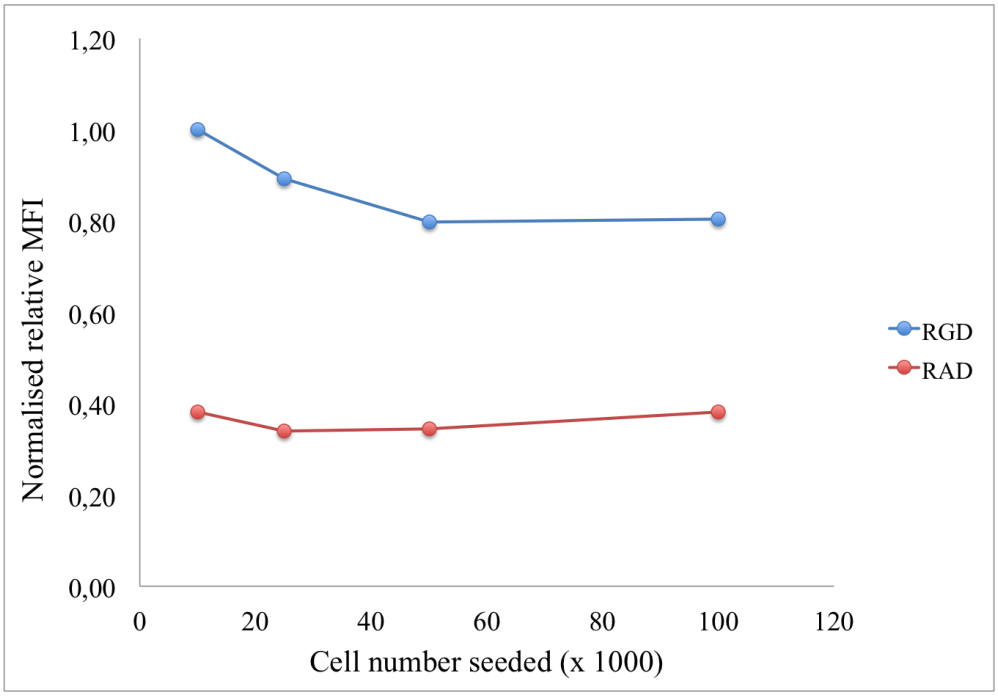

Figure 29: **Uptake of NE in cells of different confluency** Relative MFI of rhodamine-PE fluorescence for samples of HUVEC incubated with RHO-NE (1 mM) for 15 min at 37°C. NE were conjugated to targeting RGD or non-targeting RAD peptide. Cells were seeded at different cell densities 4 days prior to immunolabelling. One representative data series is presented for each experiment (n = 2).

4.8 Introduction to microscopy experiments

For all images from experiments performed with CLSM, the brightness and contrast have been more or less increased, to display the interesting features of each image as clear as possible. As such, no quantitative information may be extracted from the images presented in this thesis. As colours and image presentation may be altered by printing, some features which are visible in the digital version may be poorly visible in the printed version. If this should be the case, the reader is kindly asked to address the digital version of this thesis to view the microscopy images.

4.9 Optimisation of fixation protocol

Cells were incubated with NE for 20 min, and either directly imaged as live cells or fixed with 12 different fixation protocols, to find a suitable fixation protocol for our experiments. For live cells, uptake and/or surface binding of both RGD- and RAD-NE in HUVEC were visible after 20 min incubation, and NE were visible as fluorescent spots within each cell area (Figure 30). The bright field images in figure 30 clearly show the position and shape of the cells, while the rhodamine-PE images show the location of internalised or surface bound NE. For RAD-NE, the rhodamine-PE fluroescence signal was much weaker than for RGD-NE with the same microscope settings. To achieve resembling images, laser intensity and detector gain were increased during

imaging of RAD-NE samples, compared to RGD-NE samples. The same applies for the fixed cell samples presented below.

For fixed samples, a few fixation protocols produced satisfactory results (resembling live cell samples), while most protocols did not. The reproducibility of satisfactory results (for cells within the same sample) was highest for fixation with 4% PFA in PBS for 15 minutes at room temperature, hence this was selected as the best fixation protocol.

In general, samples fixed at room temperature (22°C) with 4% PFA, gave satisfactory results. The majority of cells in each sample showed fluorescence signals from rhodamine-PE in seperate spots within the cells, resembling the live cell samples. Samples fixed at 37°C with 4% PFA generally gave good results in a few cells, but not satisfactory results in most cells, for cells in the same sample. None of the samples fixed with 2% PFA gave good results. Furthermore, samples fixed for 15 min generally gave a better result than samples fixed for 10 min. All samples fixed on ice also gave non-satisfactory results. Common for all these samples with non-satisfactory results, was that instead of being visible in seperate, high-intensity spots within each cell, the fluorescence signals from rhodamine-PE were spread out in a diffuse signal. The diffuse fluorescence intensity was either mainly within the region of a cell, but sometimes also spread throughout the imaged area.

An illustration of satisfactory and non-satisfactory results from fixation protocols, is found in figure 31, showing samples fixed with 4% PFA in PBS for 15 min either at room temperature or on ice.

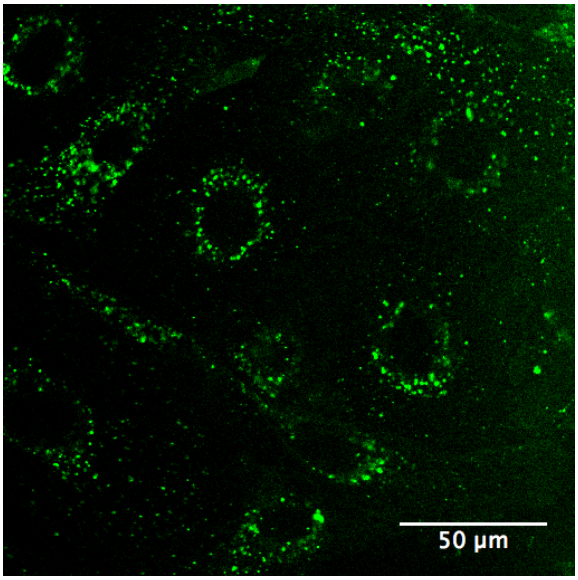

(a) Rhodamine-PE fluorescence channel. RGD-NE.

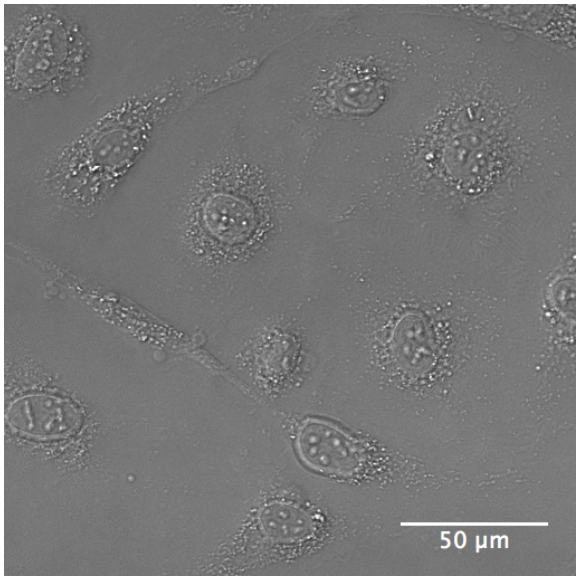

(b) Bright field image of the cells to the left. RGD-NE.

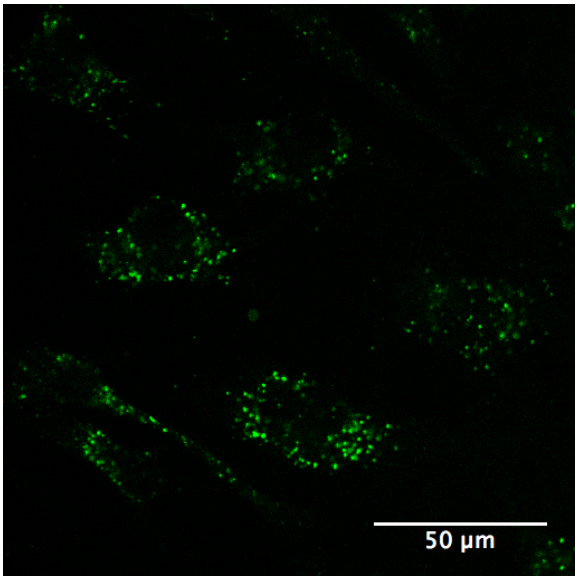

(c) Rhodamine-PE fluorescence channel. RAD-NE.

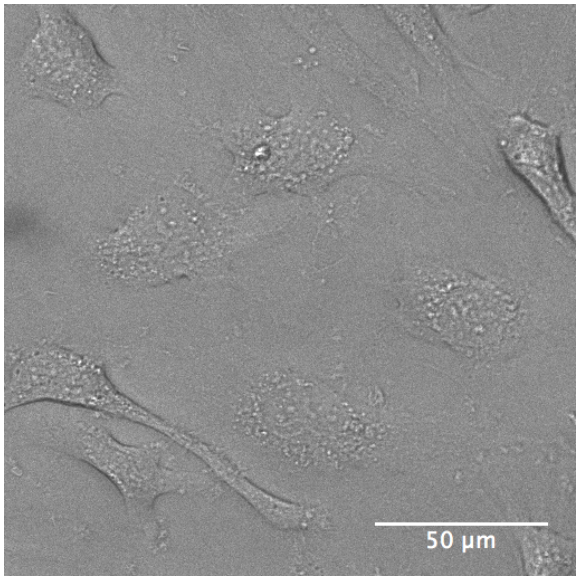

(d) Bright field image of the cells to the left. RAD-NE.

Figure 30: **Live cells** Images of live cells incubated with RHO-NE for 20 min, washed and immediately imaged on a confocal microscope. NE were conjugated to targeting RGD or non-targeting RAD peptide. Laser intensity and detector gain were increased during imaging of RAD-NE samples, compared to RGD-NE. n = 2 wells for each of RGD- and RAD-NE. Representative images are shown.

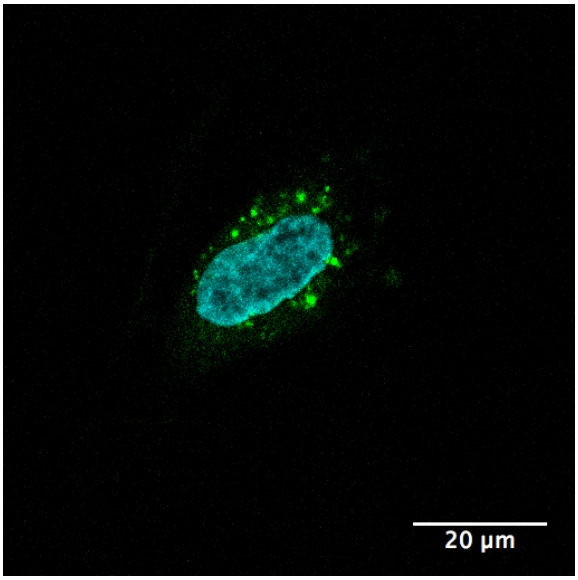

(a) Room temperature. RAD-NE.

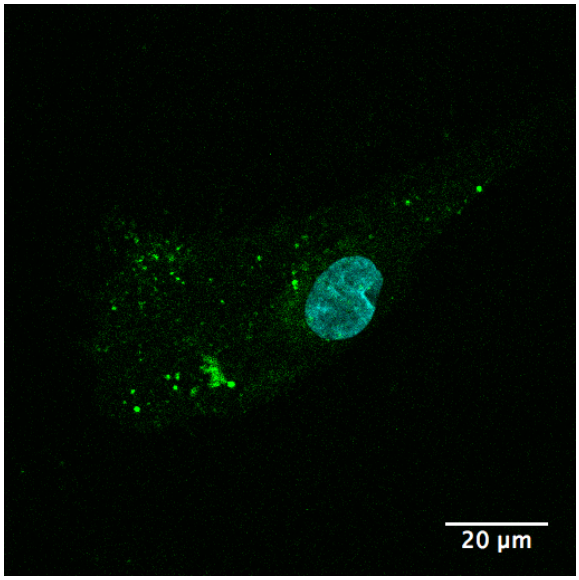

(b) Room temperature. RGD-NE.

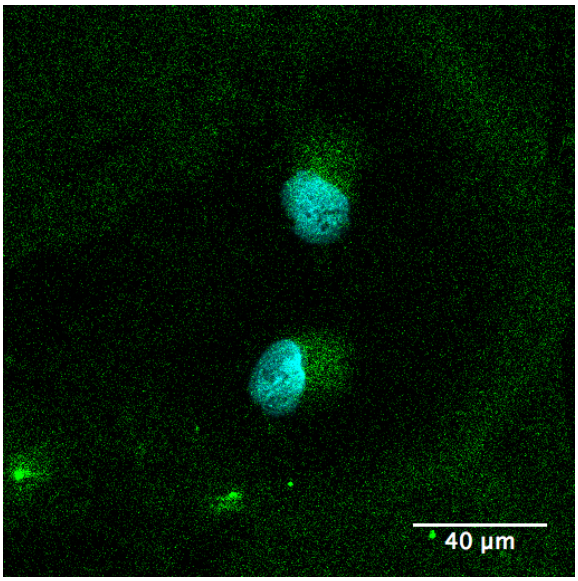

(c) Ice. RAD-NE.

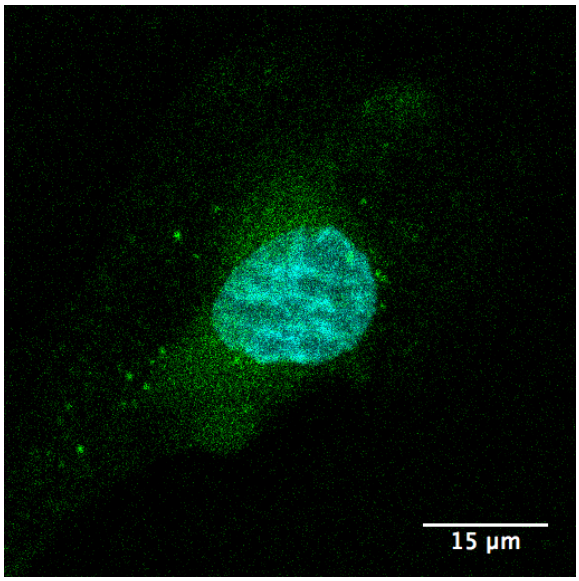

(d) Ice. RGD-NE.

Figure 31: **Fixed cells** Images of cells incubated with RHO-NE for 20 min and fixed with 4% PFA in PBS for 15 minutes at room temperature (22°C) or on ice. NE were conjugated to targeting RGD or non-targeting RAD peptide. Laser intensity and detector gain were increased during imaging of RAD-NE samples, compared to RGD-NE. The images show a merge of the rhodamine-PE and DAPI (nuclear stain) fluorescence channels, visualised in green and blue, respectively. n = 1 well per protocol. Representative images are shown.

4.10 Real-time imaging of NE incubation - optimisation for automated data analysis

A significant amount of experiments were performed in this experimental section. Therefore, the results for each of the three staining protocols are presented in two parts below. Firstly, results mainly presenting the findings for NE uptake are presented. Secondly, in section 4.10.4, results examplifying each protocol's suitability for automated data analysis are presented.

4.10.1 No cell staining

For cells with no cell staining, uptake of RGD-NE was clearly visible during the 30 min time series. For RAD-NE however, not much uptake was observed. Images showing the rhodamine-PE or Nile Red 668 fluorescence signal from 30 min time series of RGD- and RAD-NE-incubation, are presented in figure 32 - 35. Bright field images were captured, but are not presented, as they poorly visualise the cells in this focal plane. An example is however, found in section 4.10.4, figure 44a .

In all figures, the first image of the time series clearly shows the areas covered by cells (black areas) and the areas filled with NE-solution (green areas) in the focal plane. Uptake of NE with time was visible as spots of fluorescence signals which appeared within the black areas. After a time varying from 10 - 15 min for RGD-NE, all time series showed fluorescence from NE in spots within at least some of the cells, as seen in figure 32 and 33. The fluorescent spots visibly moved within the cells and tended to gather in the area around the nuclei. After approximately 20 min, at least some fluorescent spots started making formations around the nuclei in all parallels, as visible in figure 32 and 33.

The images from incubation with RGD-RHO-NE seemingly show a clearer uptake in more cells after 30 min (Figure 32d), than for RGD-NR-NE (Figure 33d). However, although not clearly visible in the images at this size, a closer investigation of the images reveal that approximately the same amount of cells show uptake of NE for NR- as RHO-NE.

In general, very little or no uptake of NE was visible during the 30 min time series for RAD-NE for all parallels performed. In some samples, weak fluorescence signals (compared to samples incubated with RGD-NE) appeared in intracellular regions, like seen in figure 34d. However, this occured at a later time point than for RGD-NE.

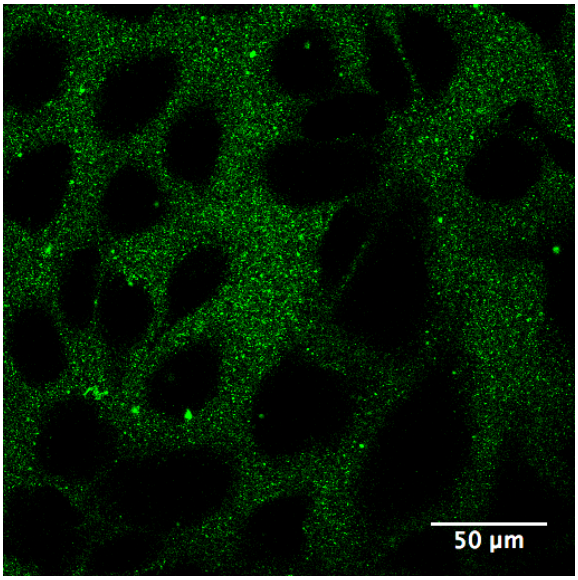

(a) First image of the time series, ∼ 2 minutes after addition of NE

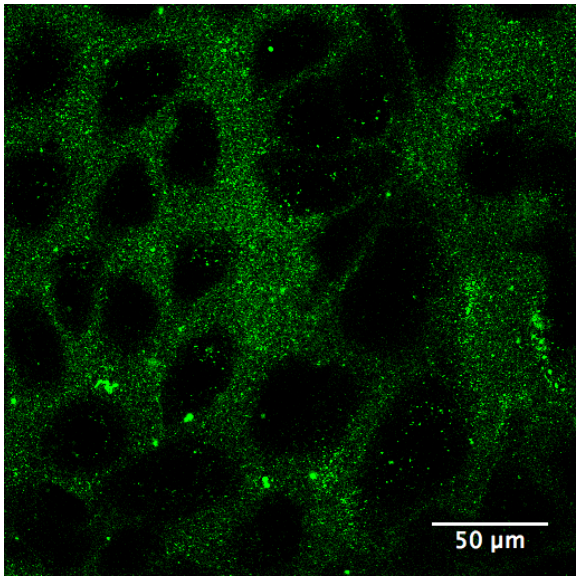

(b) 10 minutes after initiation of the time series

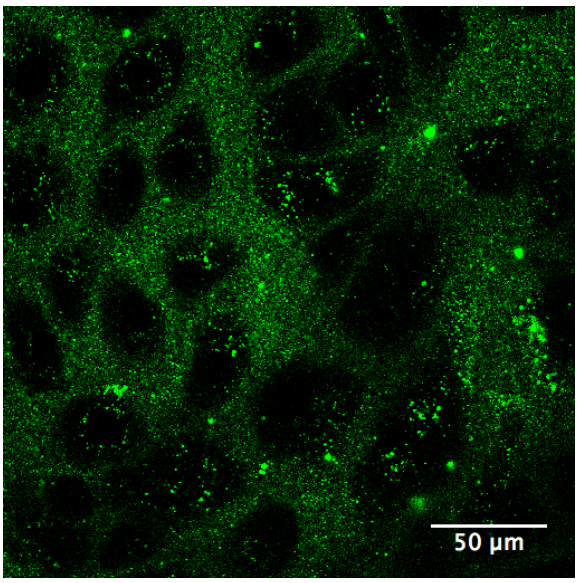

(c) 20 minutes after initiation of the time series

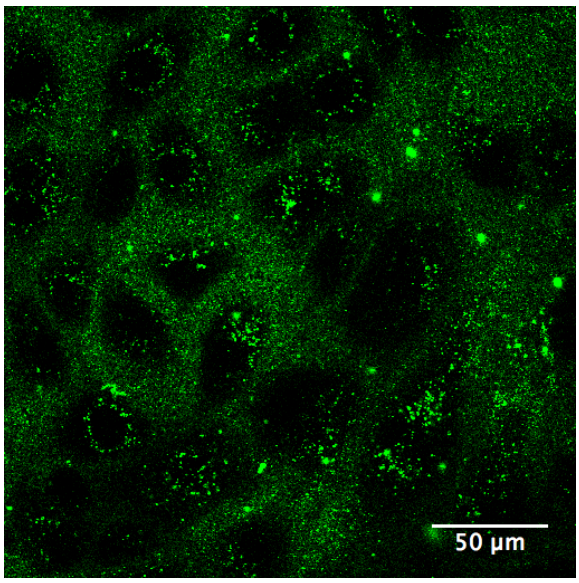

(d) 30 minutes after initiation of the time series

Figure 32: **Incubation with RGD-RHO-NE, No cell staining** Four snapshots from a 30 min time series of HUVEC incubated with 1 mM RGD-RHO-NE captured on a confocal microscope. Cells were not stained with any cell staining prior to incubation. The images show the rhodamine-PE fluorescence channel visualised in green. The black areas represent cells. n = 3.

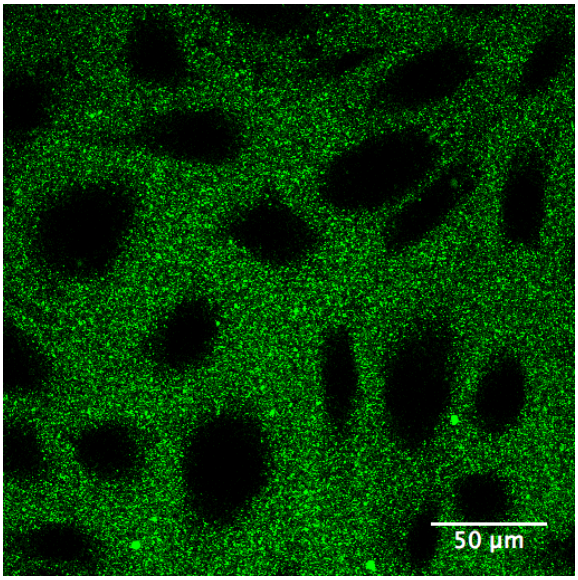

(a) First image of the time series, ∼ 2 minutes after addition of NE

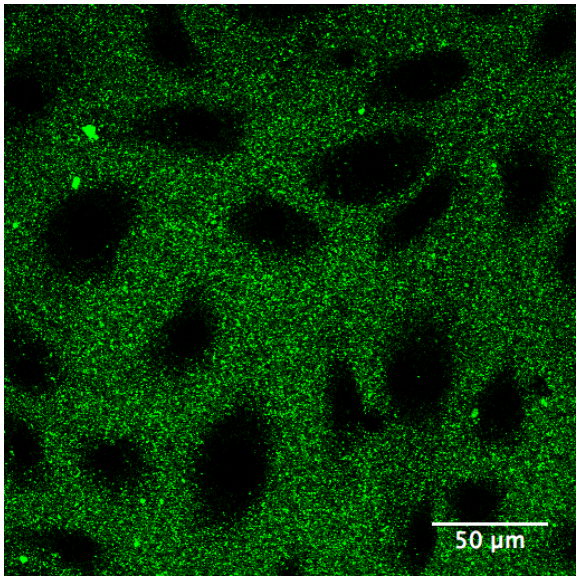

(b) 10 minutes after initiation of the time series

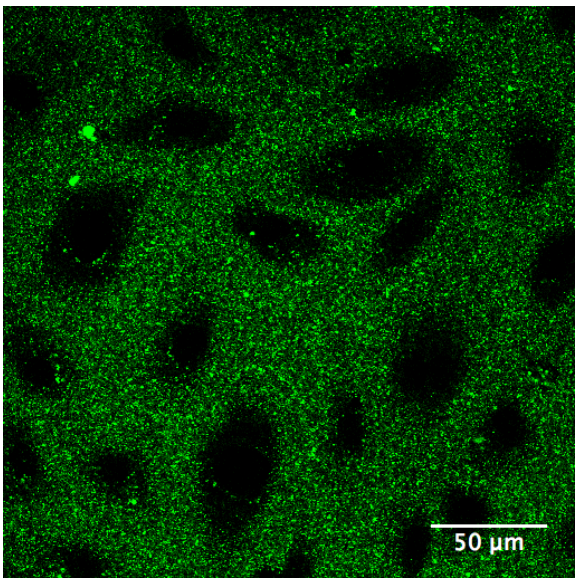

(c) 20 minutes after initiation of the time series

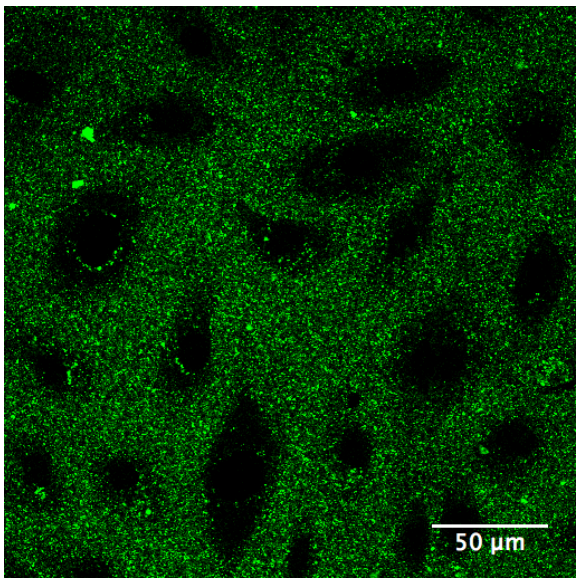

(d) 30 minutes after initiation of the time series

Figure 33: **Incubation with RGD-NR-NE, No cell staining** Four snapshots from a 30 min time series of HUVEC incubated with 1 mM RGD-NR-NE captured on a confocal microscope. Cells were not stained with any cell staining prior to incubation. The images show the Nile Red 668 fluorescence channel visualised in green. The black areas represent cells. n = 3.

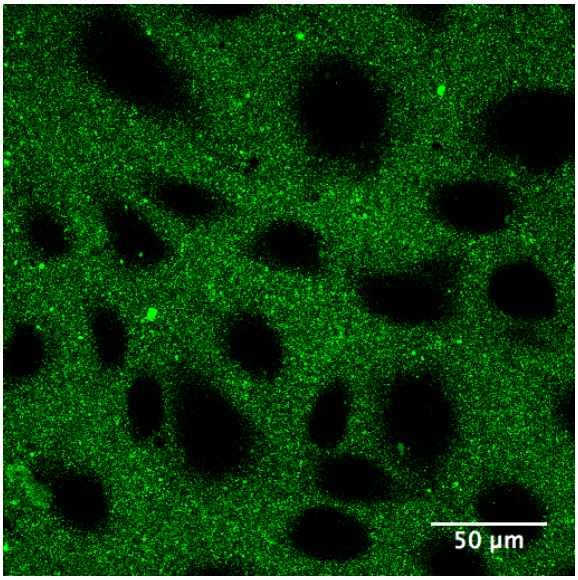

(a) First image of the time series, ∼ 2 minutes after addition of NE

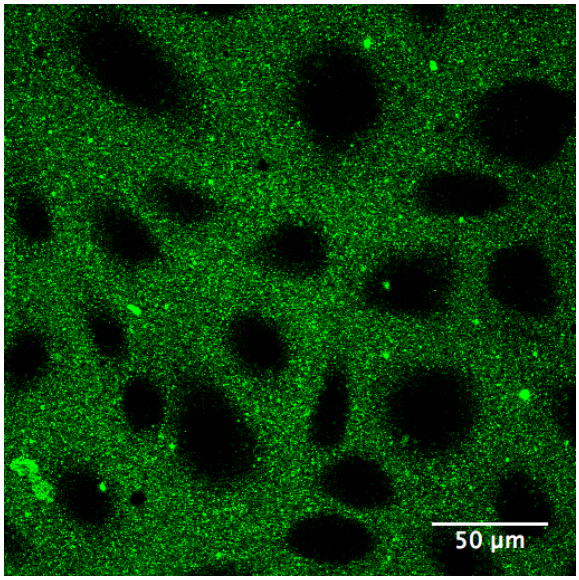

(b) 10 minutes after initiation of the time series

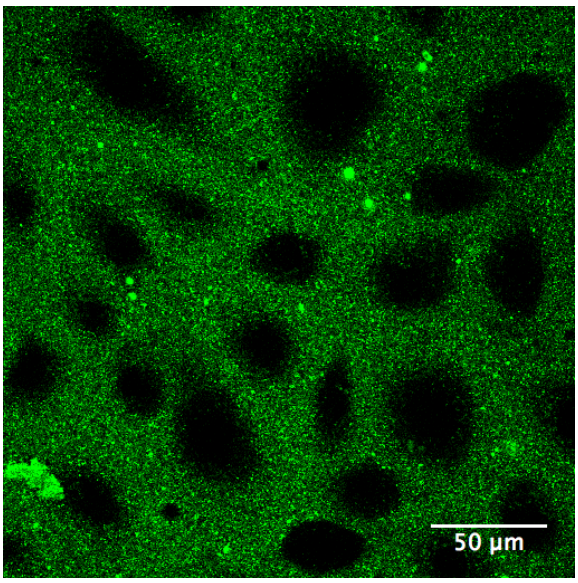

(c) 20 minutes after initiation of the time series

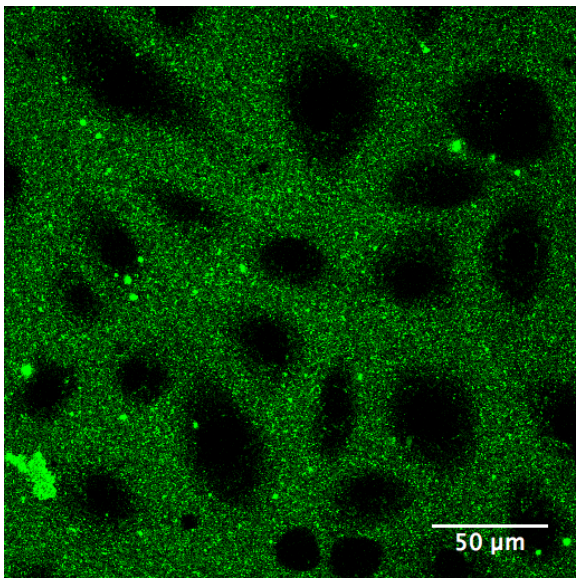

(d) 30 minutes after initiation of the time series

Figure 34: **Incubation with RAD-RHO-NE, No cell staining** Four snapshots from a 30 min time series of HUVEC incubated with 1 mM RAD-RHO-NE captured on a confocal microscope. Cells were not stained with any cell staining prior to incubation. The images show the rhodamine-PE fluorescence channel visualised in green. The black areas represent cells. n = 2.

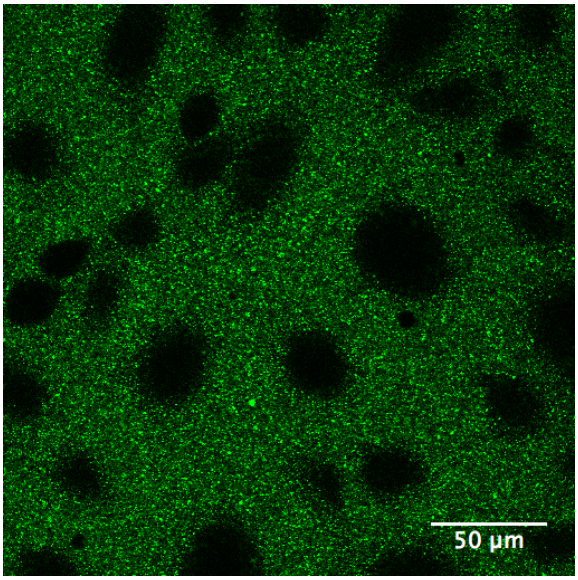

(a) First image of the time series, ∼ 2 minutes after addition of NE

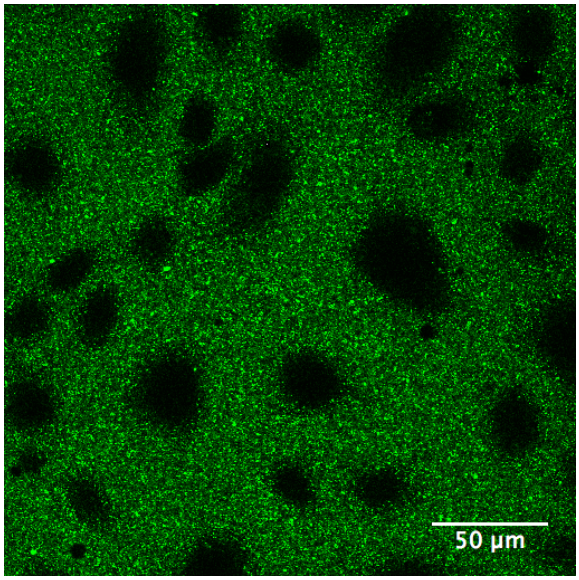

(b) 10 minutes after initiation of the time series

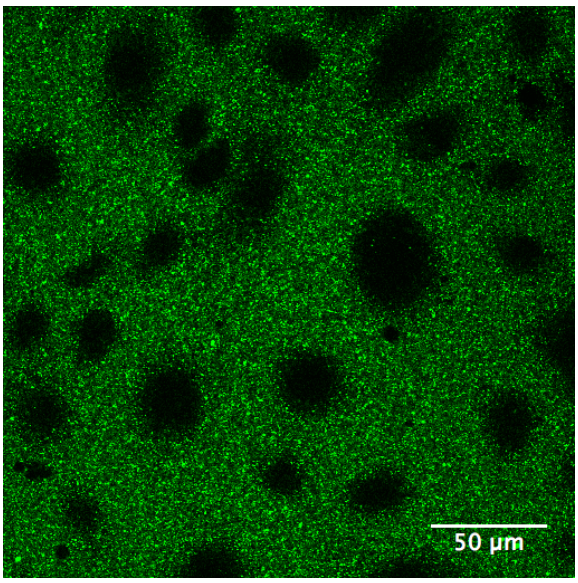

(c) 20 minutes after initiation of the time series

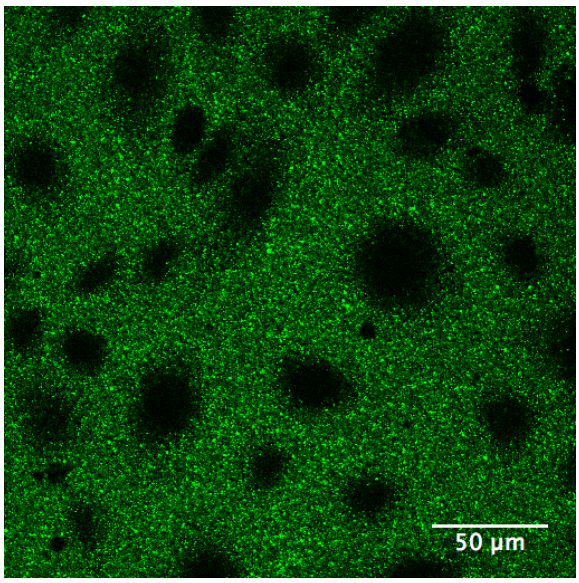

(d) 30 minutes after initiation of the time series

Figure 35: **Incubation with RAD-NR-NE, No cell staining** Four snapshots from a 30 min time series of HUVEC incubated with 1 mM RAD-NR-NE captured on a confocal microscope. Cells were not stained with any cell staining prior to incubation. The images show the Nile Red 668 fluorescence channel visualised in green. The black areas represent cells. n = 3

4.10.2 Cells stained with Hoechst nuclear stain and CellMask™ plasma membrane stain

For cells stained with Hoechst and CellMask™, uptake of RGD-NE was clearly visible in only certain regions of each imaged area. Incubation with RAD-NE showed little uptake in general. Only RHO-NE was utilised. Images showing the rhodamine-PE and CellMask™ fluorescence signal from a 30 min time series of RGD-RHO-NE-incubation, are presented in figure 36 and 37, respectively. The two channels are visualised separately, because features in the CellMask™-channel becomes poorly visible otherwise. An image of the Hoechst stain is presented in section 4.10.4, figure 45.

In the rhodamine-PE fluorescence image in figure 36d, significant uptake of NE is seen around the nuclei (similar to the samples with no cell stain) after 30 min, mainly in cells in the upper and right regions of the imaged area. Cells in other regions, show much less or no uptake of NE. In these regions, few and weak, or no, fluorescence spots appear inside the cells during the 30 min of imaging.

Images of the CellMask™-channel show interesting features which may in fact account for the observed variations in NE uptake. In the first image of the time series (Figure 37a), most cells look relatively healthy with normal cell-to-cell contacts. During the 30 min time series, cells in the region where no NE uptake is observed in the rhodamine-PE fluorescence image, gradually contract, lose cell-to-cell contact, and start looking unhealthy. When seeing the whole time series, the contracting movement appears smooth and even, and it looks like the cells are on their way to detach from the surface. The cells in the regions where NE uptake is observed in the rhodamine-PE fluorescence images, do not shrink and start looking unhealthy in the same manner. Similar observations were made for all parallels performed with RGD-RHO-NE. An additional illustration of this is presented in appendix B, figure 55 and 56.

For samples incubated with RAD-NE, generally very little or no uptake of NE was observed. Results were similar to results for no cell staining incubated with RAD-NE, except even fewer cells showed intracellular fluorescence signals. In the CellMask™ fluorescence images, it was also here, as for samples incubated with RGD-NE, observed that cells in certain regions did shrink and started appearing unhealthy, while cells in other regions did not.

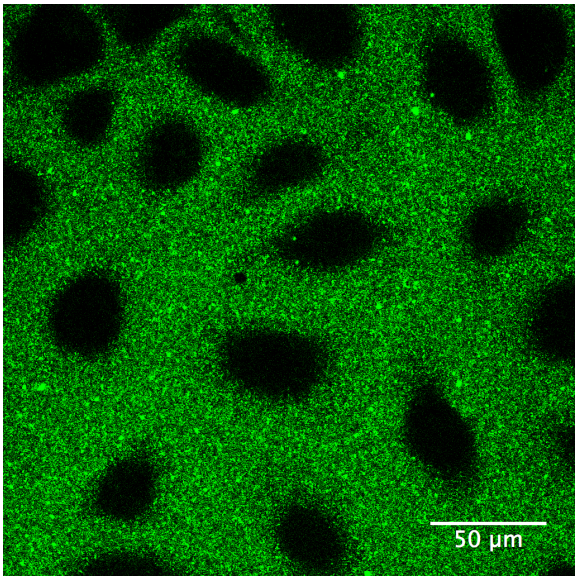

(a) First image of the time series, ∼ 2 minutes after addition of NE

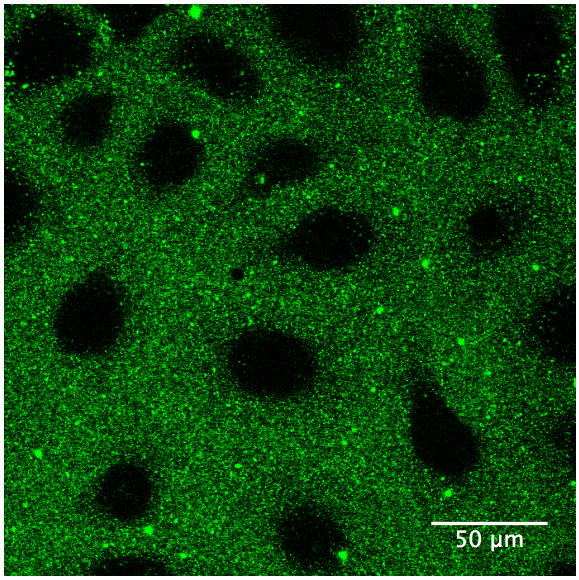

(b) 10 minutes after initiation of the time series

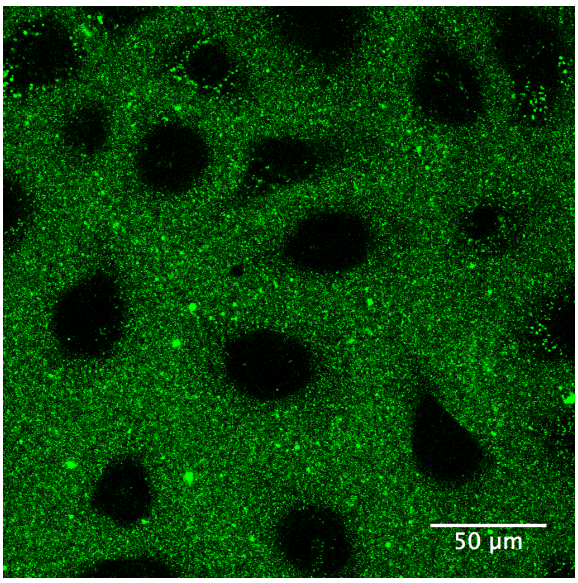

(c) 20 minutes after initiation of the time series

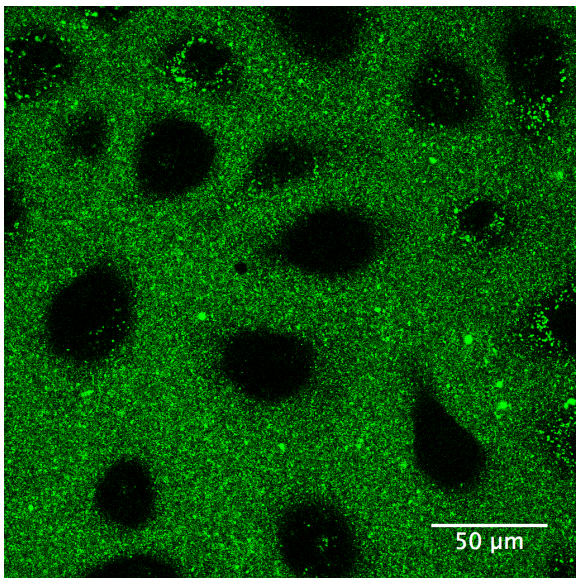

(d) 30 minutes after initiation of the time series

Figure 36: **Incubation with RGD-RHO-NE, Hoechst and CellMask™ staining** Four snapshots from a 30 min time series of HUVEC incubated with 1 mM RGD-RHO-NE captured on a confocal microscope. Cells were stained with Hoechst and CellMask™ prior to incubation. The images show the rhodamine-PE fluorescence channel visualised in green. The black areas represent cells. n = 3.

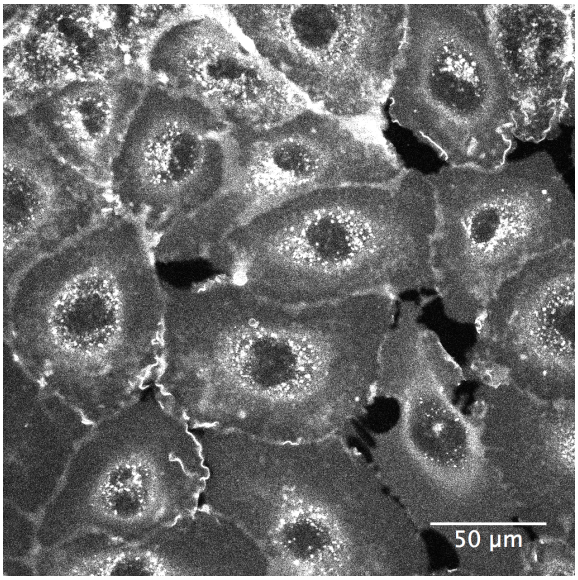

(a) First image of the time series, ~ 2 minutes after addition of NE

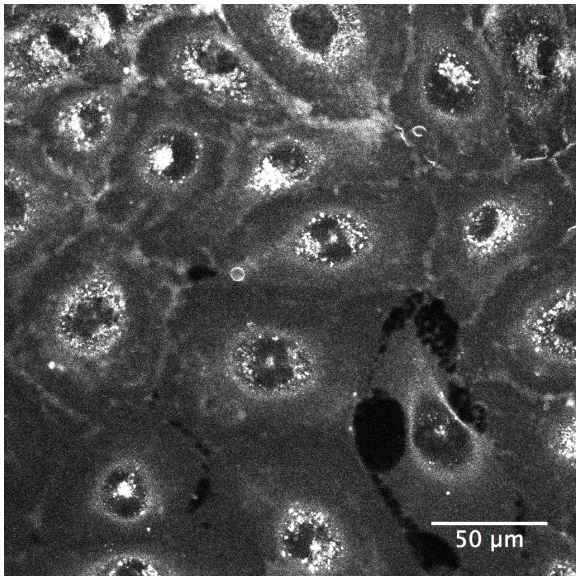

(b) 10 minutes after initiation of the time series

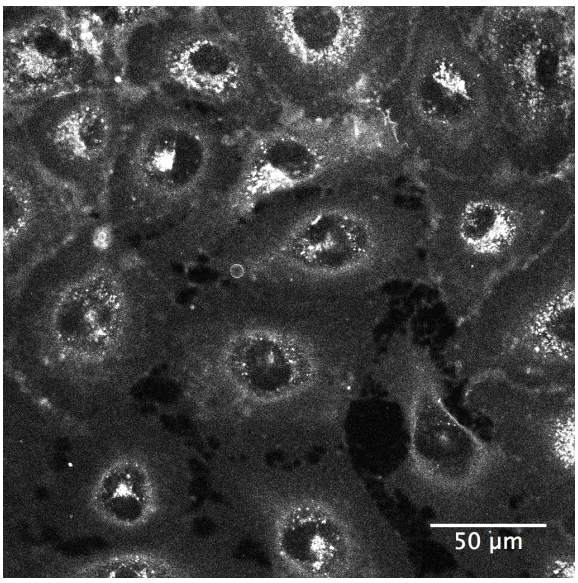

(c) 20 minutes after initiation of the time series

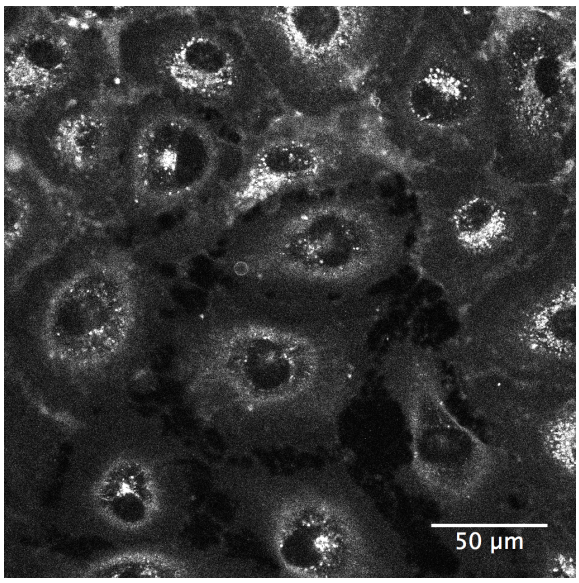

(d) 30 minutes after initiation of the time series

Figure 37: **Incubation with RGD-RHO-NE, Hoechst and CellMask™ staining** Four snapshots from the same 30 min time series of HUVEC incubated with 1 mM RGD-RHO-NE as in figure 36. Cells were stained with Hoechst and CellMask™ prior to incubation. The images show the CellMask™ fluorescence channel, visualised in white. n = 3.

4.10.3 Cells stained with Hoechst nuclear stain and Calcein AM cytoplasm stain

For cells stained with Hoechst and Calcein AM, very little or no uptake of both RGD- and RAD-NE were observed for all parallels performed. Only RHO-NE was utilised, and experiments were performed with both five weeks old and freshly made NE. The first and last rhodamine-PE fluorescence image from a 30 min time series of RGD-RHO-NE-incubation, are presented in figure 38. Images of Calcein AM and Hoechst stains are presented in section 4.10.4, figure 46. Comparing figures 38a and 38b, it is evident that no fluorescent spots become visible within the black areas during the time series.

As no uptake of NE was observed, the sample wells were closely examined after termination of the 30 min time series. The area imaged in the time series was examined in higher and lower focal planes, but no fluorescent spots within the black areas (cells) were observed. However, when other areas of the well were imaged, uptake of NE was clearly visible in most of them. Not all cells in all imaged areas showed uptake, but most areas showed at least some cells with clearly visible intracellular fluorescent spots (Figure 39a).

To get a better view of the area of cells imaged in the time series, compared to surrounding cells, images were taken at lower magnification. Figure 39b shows an image where the area imaged in the time series is marked with a white box. Here, a dilation of the area imaged in the time series, show cells as black areas, while surrounding cells have clearly internalised NE. For this imaging, it was difficult to get the whole imaged area in focus simultaneously. Hence, the lower and left side of the image is out of focus. However, cells in these regions looked similar to cells at the top and right side of the image. The entire well was examined step by step, and all other areas than the one imaged in the time series, showed cells with uptake of NE similar to this. The same observation was made during examination of other wells after termination of the time series.

An experiment was performed to test if bleaching of internalised NE could be a cause of no visible NE internalisation in cells stained with Hoechst and Calcein AM. In a sample well where a 30 min time series *had already been captured*, a region of cells clearly showing uptake of NE was selected, and imaged in a new 30 min time series (Figure 40). No reduction in intracellular fluorescence signal intensity was observed during the time series. Rather, an increase in intracellular fluorescence intensity was observed.

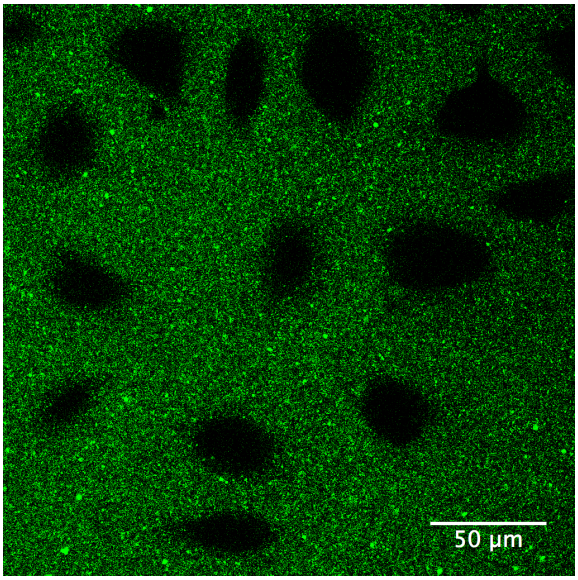

(a) First image of the time series, ∼ 2 minutes after addition of NE.

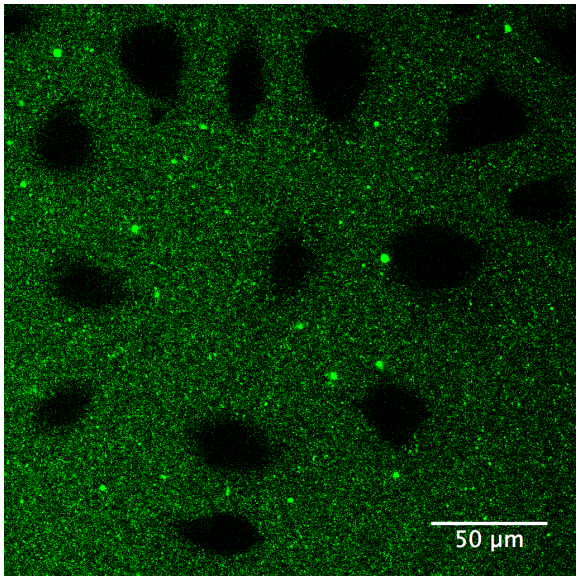

(b) 30 minutes after initiation of the time series.

Figure 38: **Incubation with RGD-RHO-NE, Hoechst and Calcein AM staining** Two snapshots from a 30 min time series of HUVEC incubated with 1 mM RGD-RHO-NE captured on a confocal microscope. Cells were stained with Hoechst and Calcein AM prior to incubation. The images show the rhodamine-PE fluorescence channel visualised in green. n = 5.

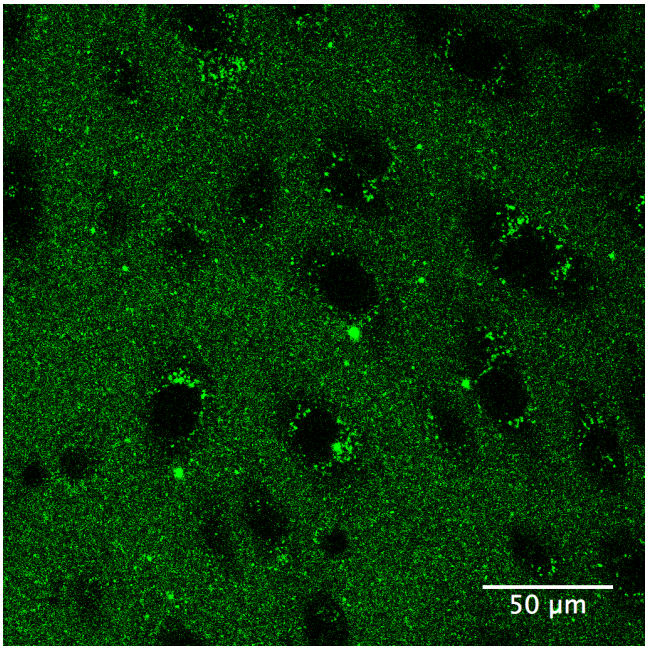

(a) An area of the sample well not imaged in the 30 min time series. Image taken immediately after termination of the 30 min time series.

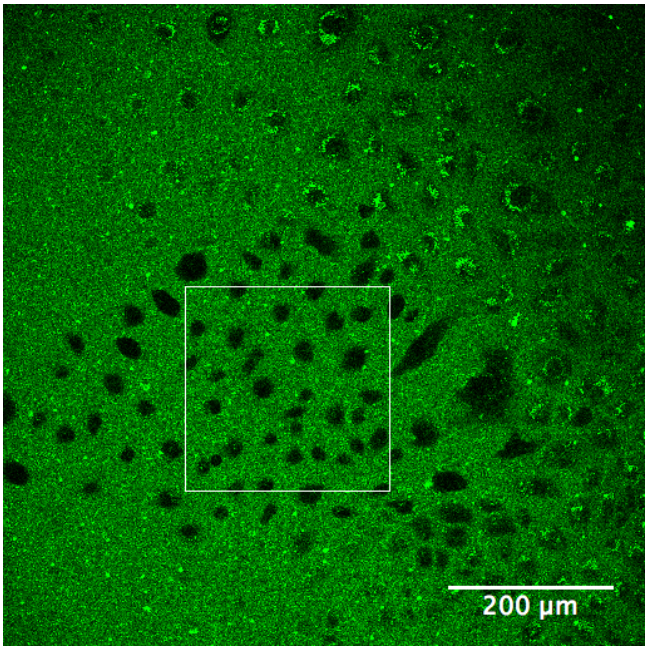

(b) Image taken at lower magnification than the time series. The area imaged in the time series is marked with a white box. Image taken several minutes after termination of the time series.

Figure 39: **Uptake of NE in surrounding areas, Incubation with RGD-RHO-NE, Hoechst and Calcein AM staining** Images of cells after termination of a 30 min time series of HUVEC incubated with 1 mM RGD-RHO-NE. Cells were stained with Hoechst and Calcein AM prior to incubation. The images show the rhodamine-PE fluorescence channel visualised in green.

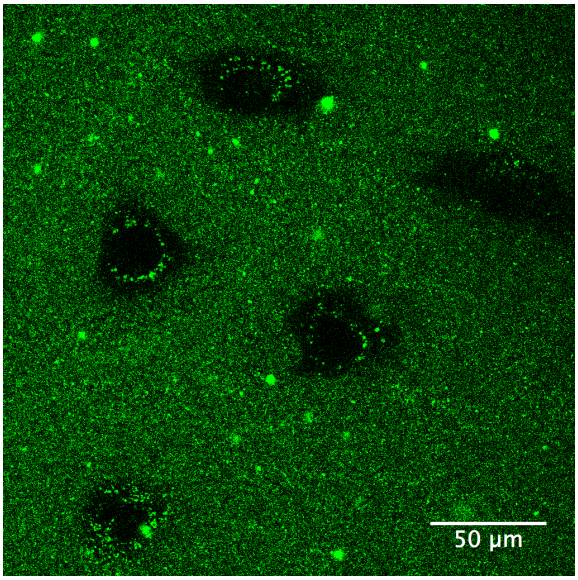

(a)
First image of the time series.

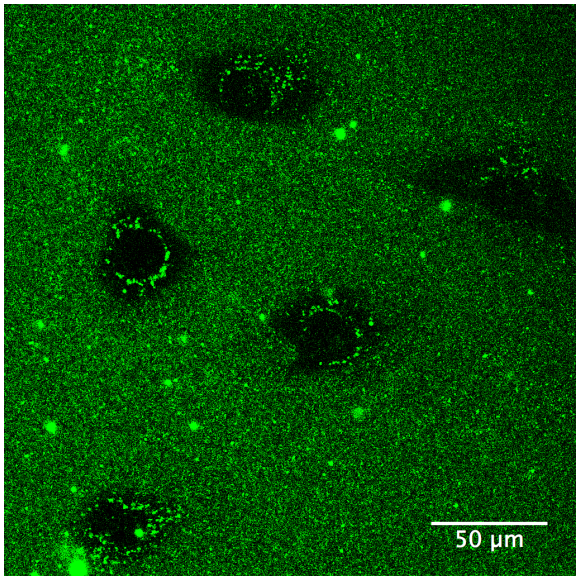

(b) 30 minutes after initiation of the time series.

Figure 40: **Test of bleaching, Incubation with RGD-RHO-NE, Hoechst and Calcein AM staining** Two snapshots from a 30 min time series of HUVEC incubated with 1 mM RGD-RHO-NE captured on a confocal microscope. The time series was taken after another 30 min time series, in the same well, but another area. Cells were stained with Hoechst and Calcein AM prior to incubation. The images show the rhodamine-PE fluorescence channel visualised in green. n = 1.

Closer study of time series in image analysis software In the search for an explanation of no NE uptake with Hoechst and Calcein AM staining, images were closely studied in image analysis softwares. By significantly increasing the brightness and contrast in Calcein fluorescence images, important information was uncovered (Figure 41). Although the image quality becomes poor by increasing the brightness and contrast, a larger area of each cell becomes visible. The additional cell areas visible, have weak fluorescence intensities because of the shape of the cells, which is thick at the cell centre and thin at the cell periphery.

From figure 41, it is clearly visible that, as for experiments with CellMask^{TM}, cells contract and lose cell-to-cell contact during the time series. When seeing the whole time series, the contracting movement of the cell cytoplasm towards the cell center was similar as in experiments with CellMask^{TM}. From the even and smooth contracting movement, it looks like the cells are on their way to detach from the surface, rather than e.g. be moving out of the focal plane.

Closer studies of the rhodamine-PE fluorescence images revealed that the contracting movement was also visible in these images. Figure 42 shows a merge of the rhodamine-PE and Hoechst fluorescence images from the same time series as in figure 41. Different time points are presented, as interesting features in the rhodamine-PE fluorescence images appeared at a later time point. The brightness of the rhodamine-PE signal is quite low, because the interesting features are not visible when the brightness is further increased. Although the cell areas become less visible in the rhodamine-PE fluorescence

image by this, cellular positions are clearly visible from the Hoechst nuclear stain.

When examining the whole time series illustrated in figure 42, it is clearly visible that after approximately 20 min, a fluorescent signal in the rhodamine-PE image gathers around the cells and then evenly moves towards the cell centres, in a movement resembling the ones observed in the Calcein and CellMask^{TM} fluorescence images. By this, the fluorescent signals associated with the cells do not at all look like internalised NE in previous experiments (section 4.10.1), where fluorescence spots randomly move around inside the cells. The described movement towards the cell centres may be difficult to see in figure 42. The arrrows pointing at the cells where the described features were observed, are placed at the same position in each of the four images. This hopefully makes it easier to observe the moving position of the fluorescence intensity 'front'.

Cells stained with Hoechst only As cells were observed to behave differently with and without stainings, an experiment was performed where only Hoechst staining was utilised in stead of two stainings simultaneously (Figure 43). As in figure 42, the brightness of the images in figure 43 is quite low because the interesting features are not visible when the brightness is increased. In the images at higher brightness (not shown), no uptake of NE was observed also in this experiment.

Interestingly, the same features as observed in the rhodamine-PE images in figure 42 (cells stained with Hoechst and Calcein AM), were observed in the rhodamine-PE images in these experiments. After approximately 10 minutes, a fluorescent signal gathers around the cells and then evenly moves towards the cell centres. In figure 43 as in figure 42, the cells where the described features are visible, are marked by an arrow which is positioned at the same place in all four images.

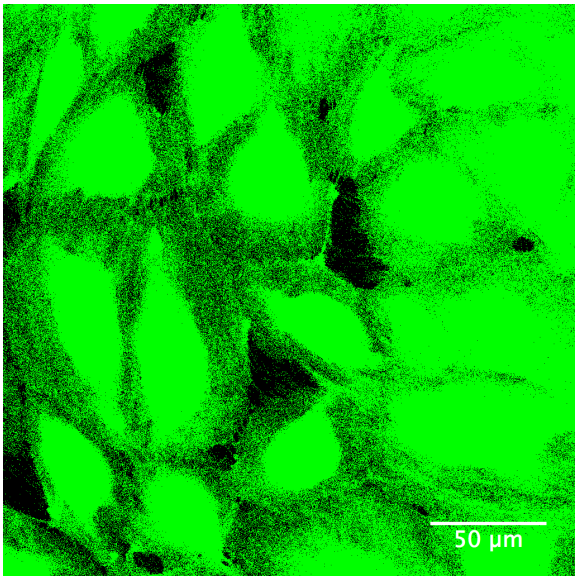

(a) First image of the time series, $\sim$ 2 minutes after addition of NE.

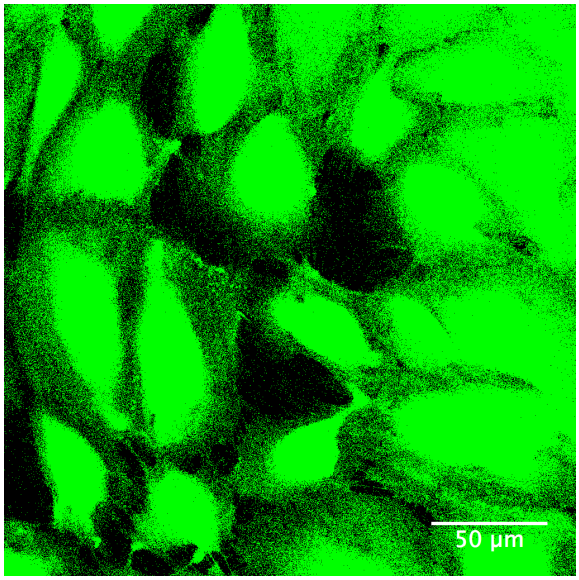

(b) 10 minutes after initiation of the time series.

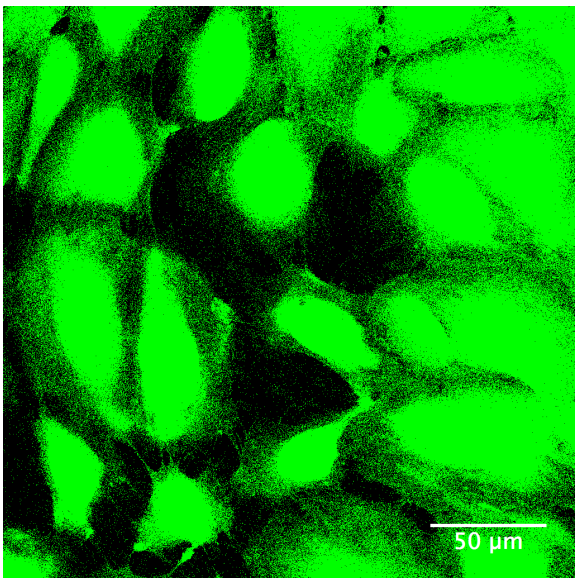

(c) 20 minutes after initiation of the time series.

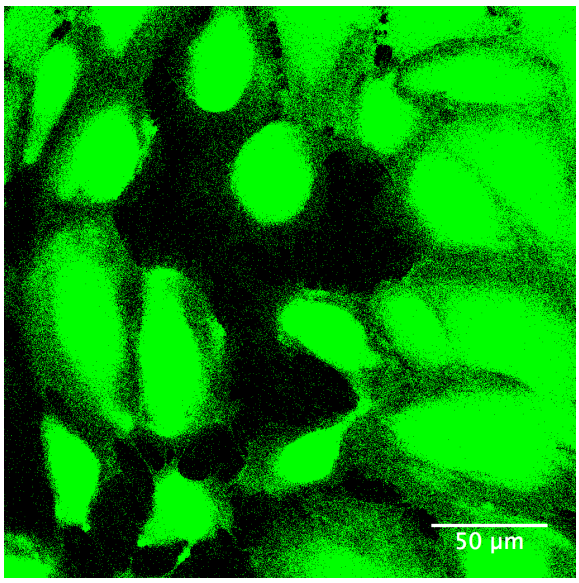

(d) 30 minutes after initiation of the time series.

Figure 41: **Incubation with RGD-RHO-NE, Hoechst and Calcein AM staining** Four snapshots from a 30 min time series of HUVEC incubated with 1 mM RGD-RHO-NE captured on a confocal microscope. Cells were stained with Hoechst and Calcein AM prior to incubation. The images show the Calcein fluorescence channel (with extensively increased brightness), visualised in green. n = 5.

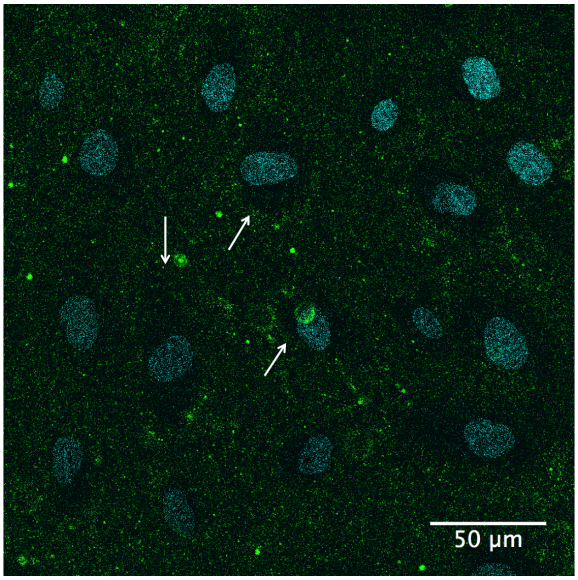

(a) 20 minutes after initiation of the time series.

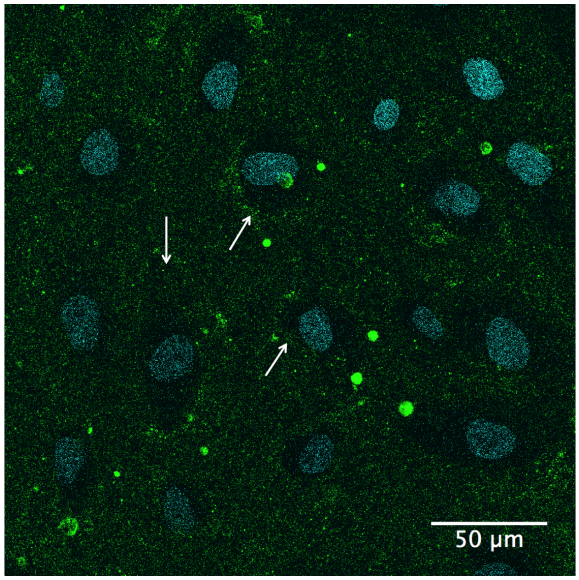

(b) 25 minutes after initiation of the time series.

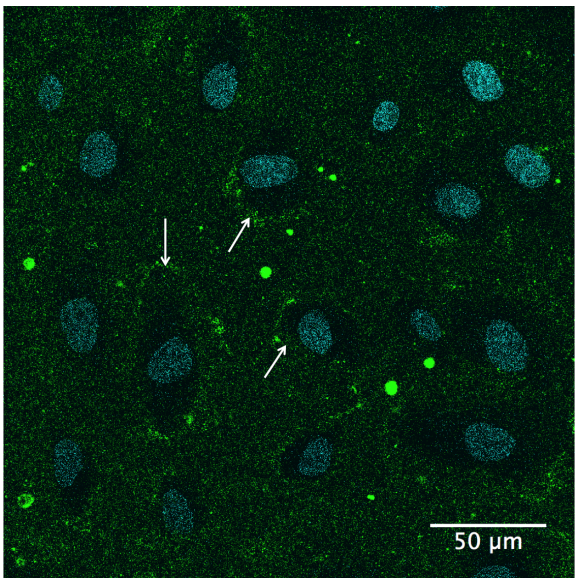

(c) 27.5 minutes after initiation of the time series.

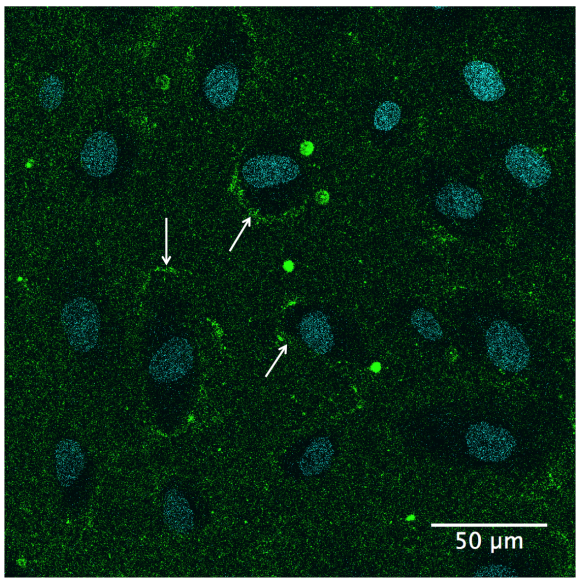

(d) 30 minutes after initiation of the time series.

Figure 42: **Incubation with RGD-RHO-NE, Hoechst and Calcein AM staining** Four snapshots from the same 30 min time series of HUVEC incubated with 1 mM RGD-RHO-NE as in figure 41. Cells were stained with Hoechst and Calcein AM prior to incubation. The images show a merge of the rhodamine-PE and Hoechst fluorescence channels, which are visualised in green and blue respectively. n = 5.

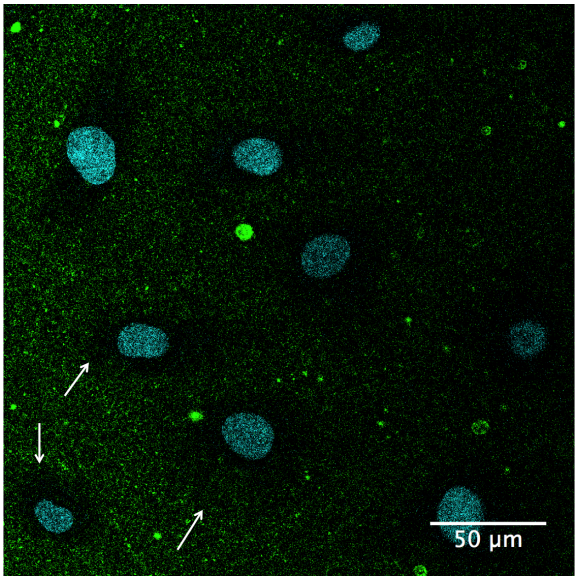

(a) 9 mintues after initiation of the time series.

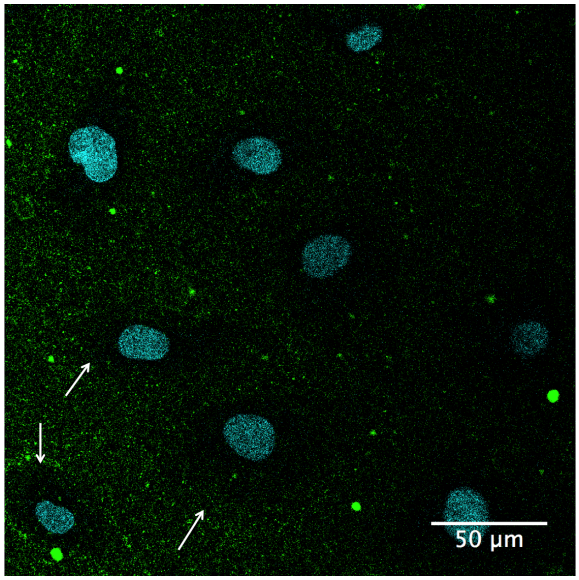

(b) 16 mintues after initiation of the time series.

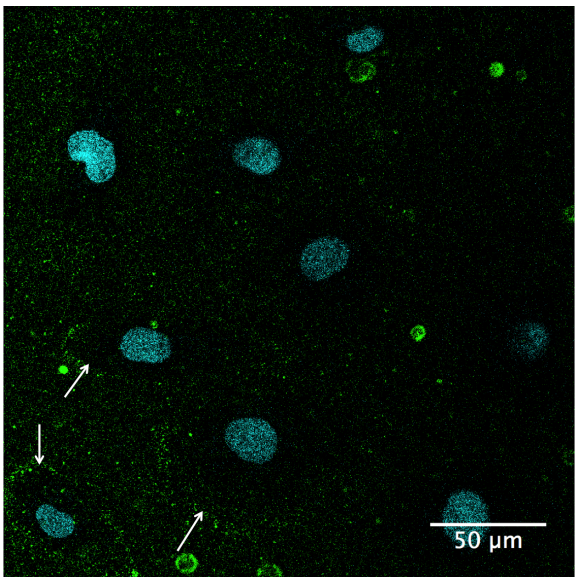

(c) 23 mintues after initiation of the time series.

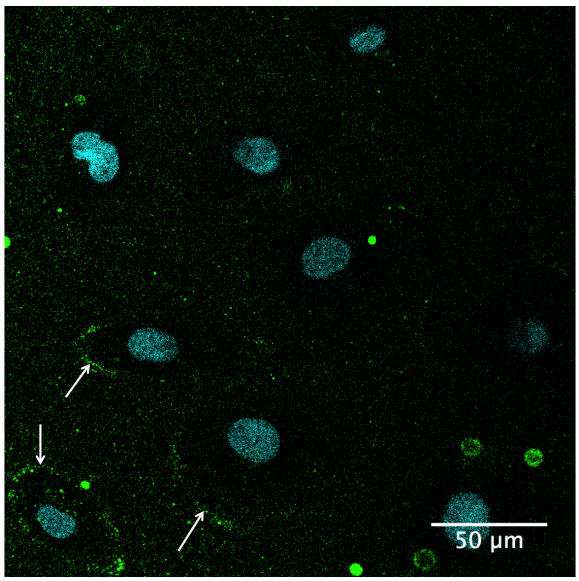

(d) 30 mintues after initiation of the time series.

Figure 43: **Incubation with RGD-RHO-NE, Hoechst staining** Four snapshots from a 30 min time series of HUVEC incubated with 1 mM RGD-RHO-NE captured on a confocal microscope. Cells were only stained with Hoechst prior to incubation. The images show a merge of the rhodamine-PE and Hoechst fluorescence channels, which are visualised in green and blue respectively. n = 1.

4.10.4 Suitability for automated data analysis

No cell staining

For cells with no staining, only bright field and NE fluorescence images were available for performing image analysis. In the NE fluroescence images, the cells were clearly moving and changing shape throughout the time series. Due to the uptake of NE, the cell circumferences also often became vague with time. As mentioned previously, the bright field images poorly visualised the cells in this focal plane, as illustrated in figure 44.

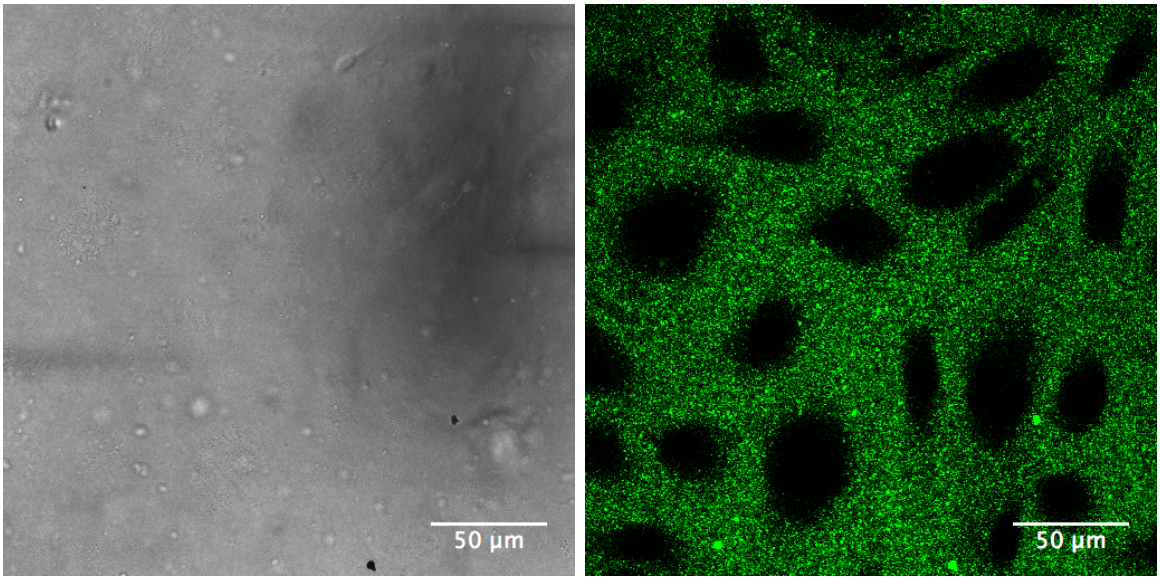

(a) Bright field image (b) Nile Red 668 fluorescence image

Figure 44: **No cell staining** The first image of a 30 min time series of HUVECs incubated with 1 mM RGD-NR-NE captured on a confocal microscope. Cells were not stained with any cell staining prior to incubation. n = 3.

Cells stained with Hoechst nuclear stain and CellMask™ plasma membrane stain

Figure 45 shows the first image of a time series with cells stained with Hoechst and CellMask™ prior to NE-incubation. All three fluorescence images Hoechst, CellMask™ and rhodamine-PE are presented seperately, and in a merge of the three.

The Hoechst nuclear stain (Figure 45a) showed a clear staining of the nuclei, and the staining was stable throughout the time series. The CellMask™ (Figure 45b) rapidly internalised (the first images were taken only minutes after staining) as it is brightly visible in vesicles around the nuclei. Fluorescence signals from the CellMask™ visualised a larger area than the dark regions representing the cells in the rhodamine-PE fluorescence images. Also, the fluorescence signal from the CellMask™ was significantly changing with time and bright fluorescent areas were often found at cell-to-cell contacts.

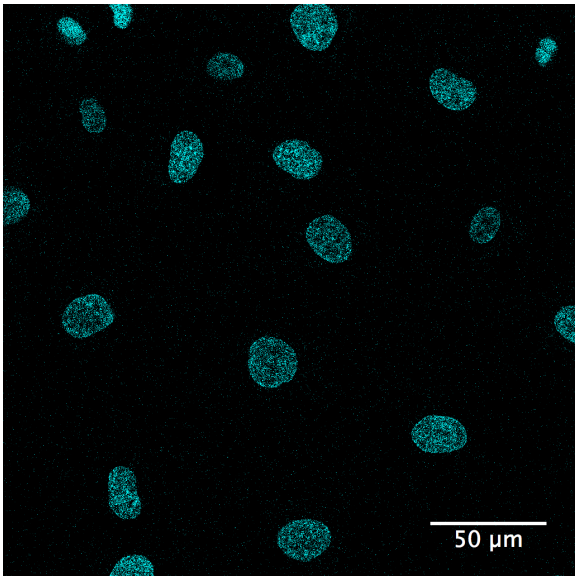

(a) Hoechst fluorescence channel (nuclear stain)

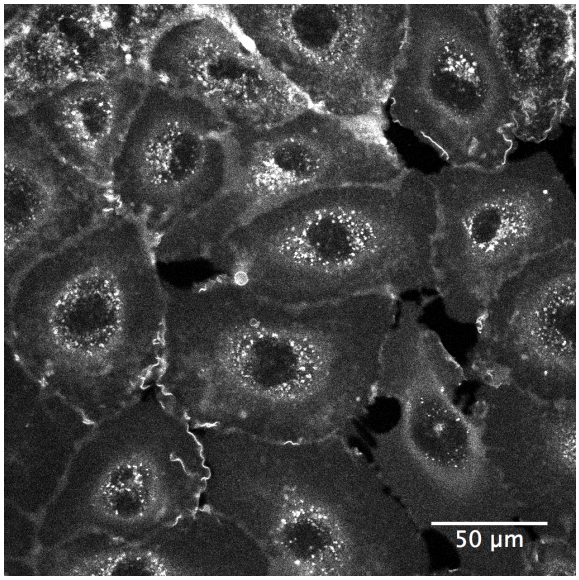

(b) CellMask^{TM} fluorescence channel (plasma membrane stain)

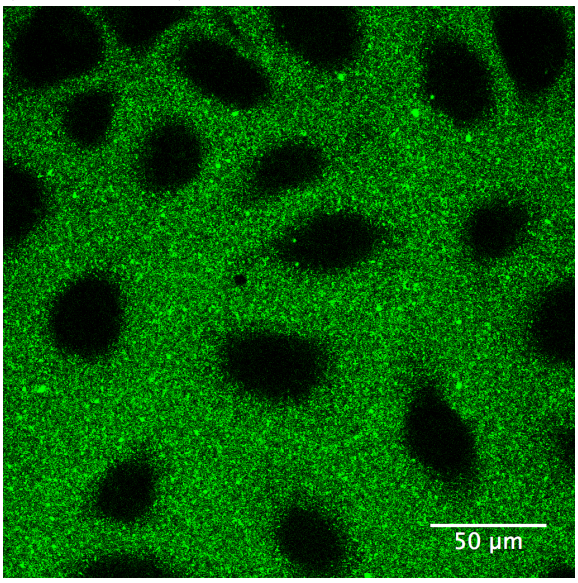

(c) Rhodamine-PE fluorescence channel.

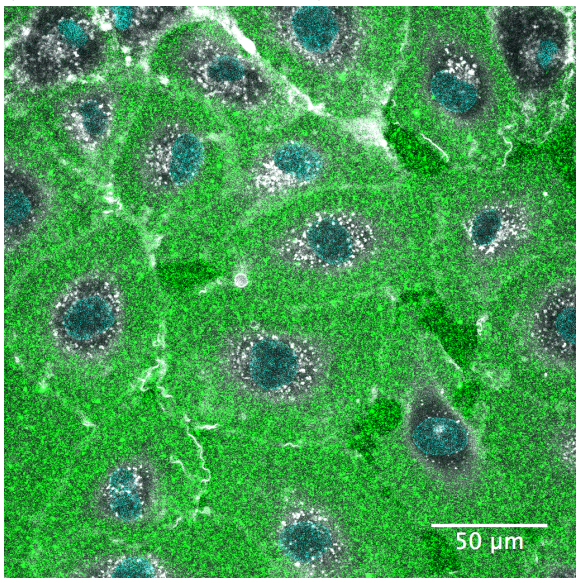

(d) A merge of the three channels.

Figure 45: **Hoechst and CellMask^{TM} staining** The first image of a 30 min time series of HUVECs incubated with 1 mM RGD-RHO-NE captured on a confocal microscope. Cells were stained with Hoechst and CellMask^{TM} prior to incubation. n = 3.

Cells stained with Hoechst nuclear stain and Calcein AM cytoplasm stain

Figure 46 shows the first image of a time series of cells stained with Hoechst and Calcein AM prior to NE-incubation. All three fluorescence images Hoechst, Calcein and rhodamine-PE are presented seperately, and in a merge of the three.

As previously, the Hoechst staining showed a clear, and stable staining of the nuclei. The Calcein fluorescence image also showed a clear visualisation of the cell cytosol which remained stable throughout the time series. The areas of Calcein fluorescence in

the focal plane, showed an almost perfect match with the black areas in the rhodamine-PE fluroescence images. The match between these fluorescent images remained stable throughut the time series.

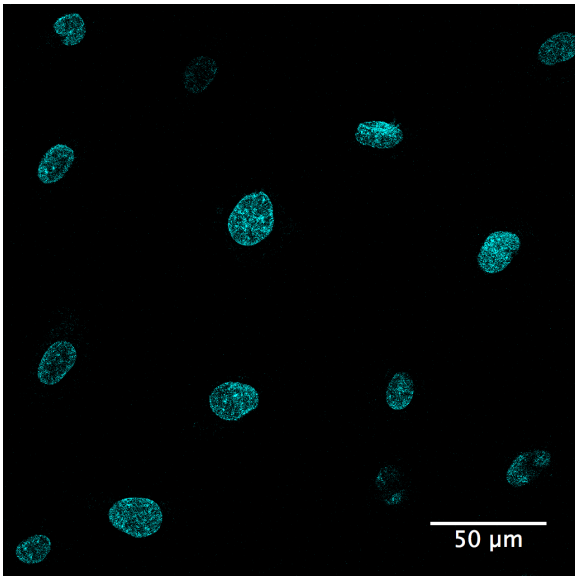

(a) Image of the Hoechst channel (nuclear stain).

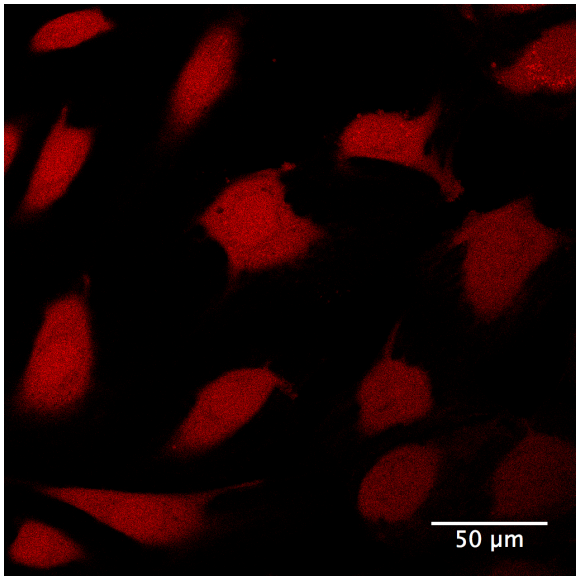

(b) Image of the Calcein AM channel (cytoplasm stain).

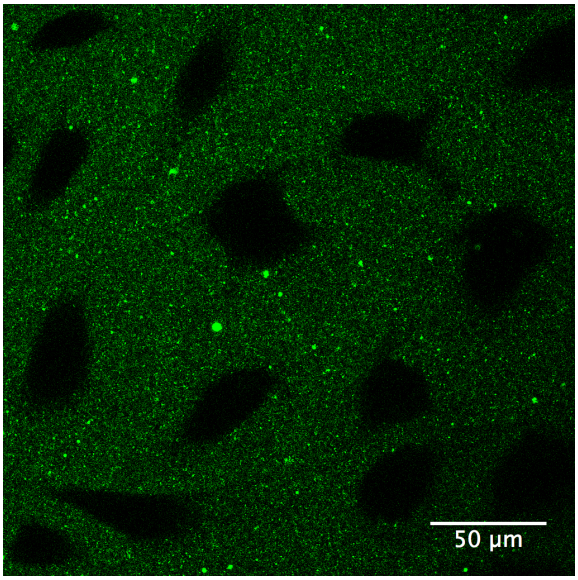

(c) Image of the rhodamine-PE channel.

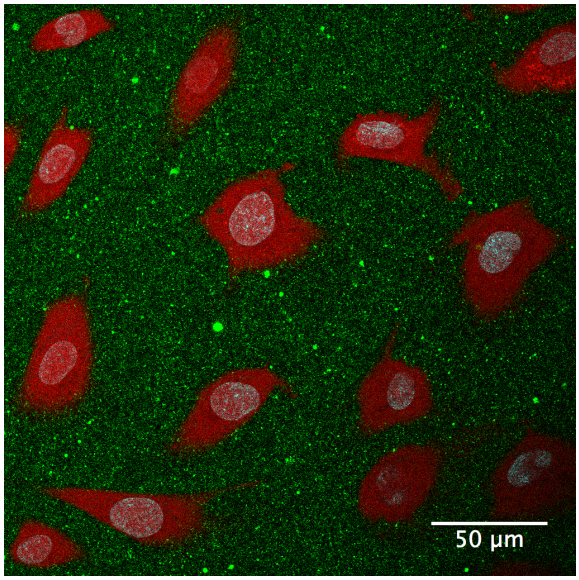

(d) A merge of the three channels.

Figure 46: **Hoechst and Calcein AM staining** The first image of a 30 min time series of HUVECs incubated with 1 mM RAD-RHO-NE captured on a confocal microscope. Cells were stained with Hoechst and Calcein AM prior to incubation. n = 3.

4.11 Introductory studies with transfection of GFP-tagged β_3-integrin

4.11.1 Successfulness of transfection

Nine different transfection protocols were tested for transfection of a vector encoding a GFP-tagged human β_3-integrin in HUVEC. The evaluation of transfection successfulness was based on the extent of GFP fluorescence combined with how healthy the cells appeared in each sample. In the following text, results 24 h after transfection, then 48 h after transfection, will be presented.

24 hours after transfection

24 hours after transfection, no successful transfection was observed for either of the nine protocols tested. Why the various protocols were found unsuccessful, varied between them and is presented below.

For 0.5μg DNA, ratio 3:1 of Lipofectamine® 2000 : DNA (Figure 47), GFP fluorescence signals were detected in most regions of the well. However, bright field images revealed that cells did not appear healthy, and species which were most likely cellular debris, were visible throughout the well.

For 0.1μg and 0.05μg DNA, ratios 1:1 and 0.5:1 of Lipofectamine® 2000 : DNA, results were very similar 24 hours after transfection (Figure 48). No GFP fluorescence signals were detected in any regions of any of the four sample wells. Also, cells looked normal and healthy in all regions of the sample wells.

For 0.1μg and 0.05μg DNA, ratios 5:1 and 3:1 of Lipofectamine® 2000 : DNA, results were also very similar 24 hours after transfection (Figure 49). GFP fluorescence signals were detected in a few regions of each sample well, while the majority of each sample well did not show any fluorescence signal. Where GFP fluorescence signals were detected, the cells did not look healthy (Figure 49a and 49b). Where no GFP fluorescence signals were detected, cells did look relatively normal and healthy (Figure 49c and 49d). However, the cells in figure 49d did not look as healthy as in figure 48b.

48 hours after transfection

48 hours after transfection, successful results were observed for all six combinations 0.05μg DNA, ratios 3:1 and 0.5:1 of Lipofectamine® 2000 : DNA, and 0.1μg DNA, ratios 5:1, 3:1, 1:1 and 0.5:1 of Lipofectamine® 2000 : DNA (Figure 50). GFP fluorescence signals were detected in most areas of each well, and cells looked relatively healthy in all regions of the wells.

For 0.05μg DNA, ratio 1:1 of Lipofectamine® 2000 : DNA, GFP fluroescence signals and healthy cells were observed, but very rarely. The majority of cells were still non-fluorescent. For 0.05μg DNA, ratio 5:1 of Lipofectamine® 2000 : DNA, results were similar as 24 hours after transfection and as presented in figure 49. For 0.5μg DNA, ratio 3:1 of Lipofectamine® 2000 : DNA, GFP fluorescence signals were now only detected in a few regions, compared to 24 h after transfection, when GFP fluorescence signals were detected in most regions of the well. Furthermore, cells did still look as unhealthy as 24 h after transfection (which is shown in figure 47b), if not worse.

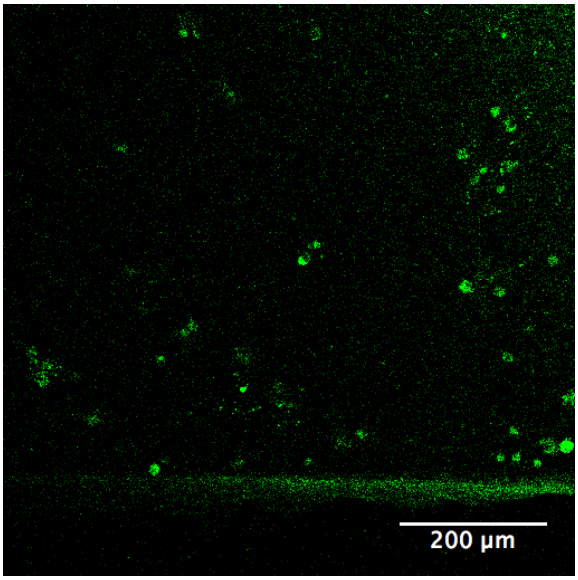

(a) GFP fluorescence image.

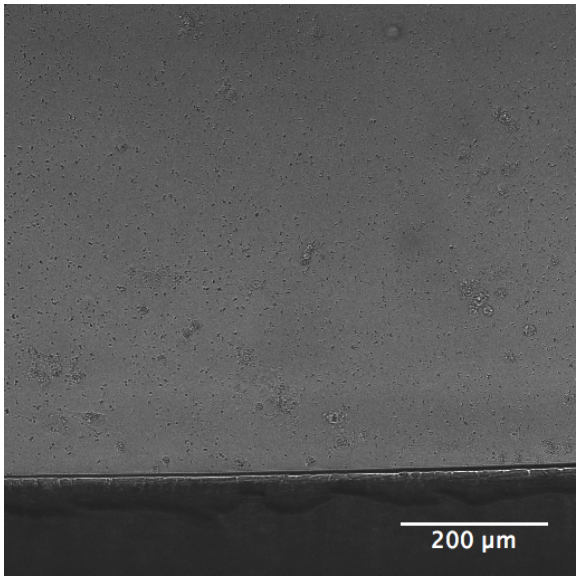

(b) Bright field image of the cells to the left.

Figure 47: **24h; GFP fluorescence, but unhealthy cells** Images of cells transfected with 0.5μg DNA (GFP-tagged human β_3-integrin), ratio 3:1 of Lipofectamine® 2000 : DNA, 24 h after transfection (n = 1).

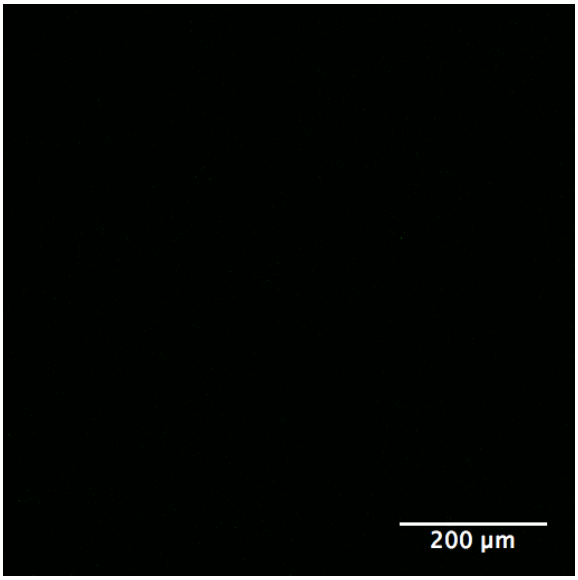

(a) No GFP fluorescence signal detected.

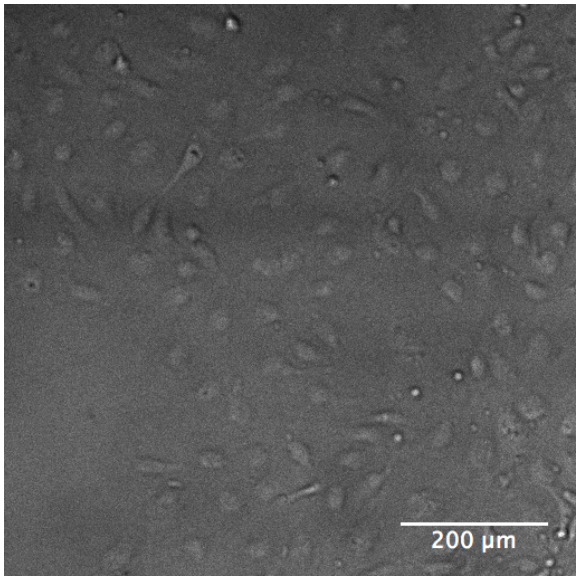

(b) Bright field image of the cells to the left.

Figure 48: **24h; no GFP fluorescence and healthy cells** Images of cells transfected with 0.1μg DNA (GFP-tagged human β_3-integrin), ratio 1:1 of Lipofectamine® 2000 : DNA, 24 h after transfection (n = 1). The images represent the result found for all four combinations of 0.1μg and 0.05μg DNA, ratios 1:1 and 0.5:1 of Lipofectamine® 2000 : DNA.

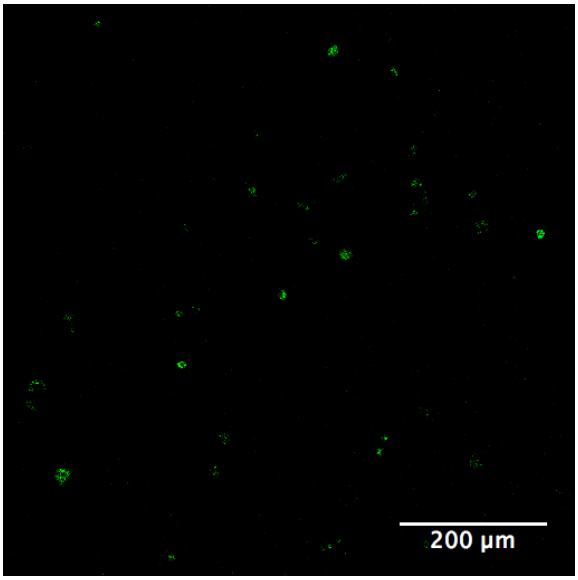

(a) GFP fluorescence signals were detected in a few regions of the well.

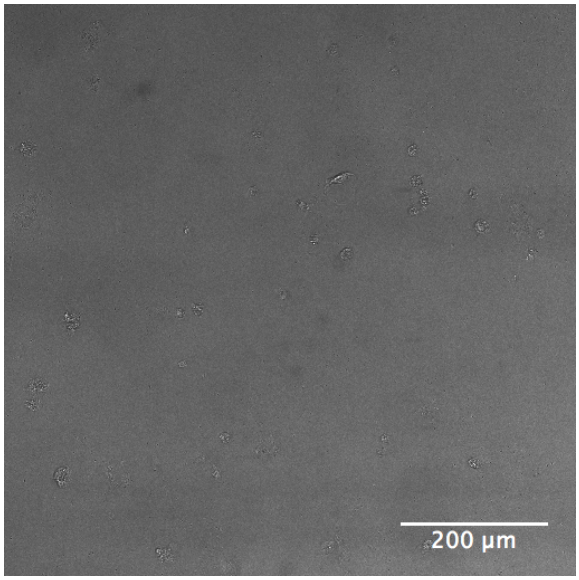

(b) Bright field image of the cells to the left. GFP-positive cells did not look too healthy.

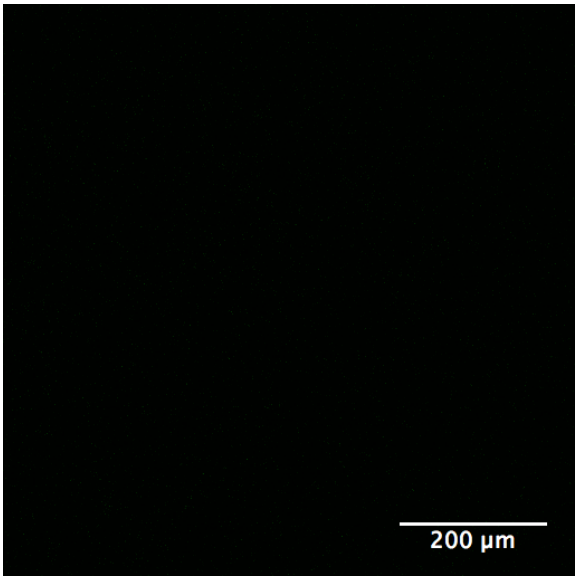

(c) No GFP fluorescence signals were detected in most regions of the well.

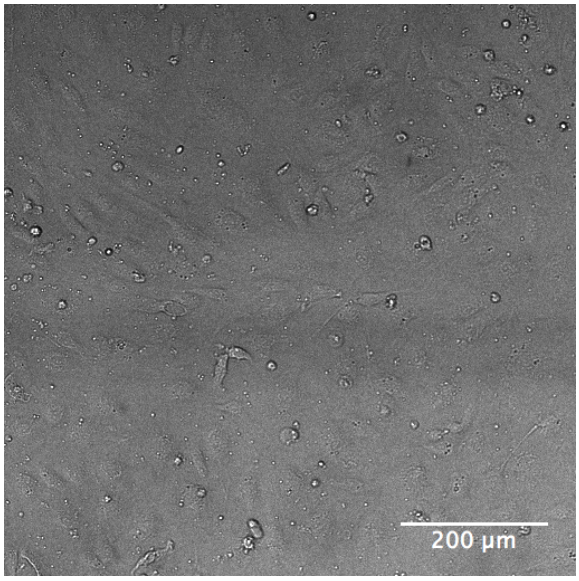

(d) Bright field image of the cells to the left. GFP-negative cells looked relatively healthy.

Figure 49: **24h; GFP fluorescence and unhealthy cells, or no GFP fluorescence and healthy cells** Images of cells transfected with 0.1μg DNA (GFP-tagged human β_3-integrin), ratio 3:1 of Lipofectamine® 2000 : DNA, 24 h after transfection (n = 1). The images represent the result found for all four combinations of 0.1μg and 0.05μg DNA, ratios 3:1 and 5:1 of Lipofectamine® 2000 : DNA.

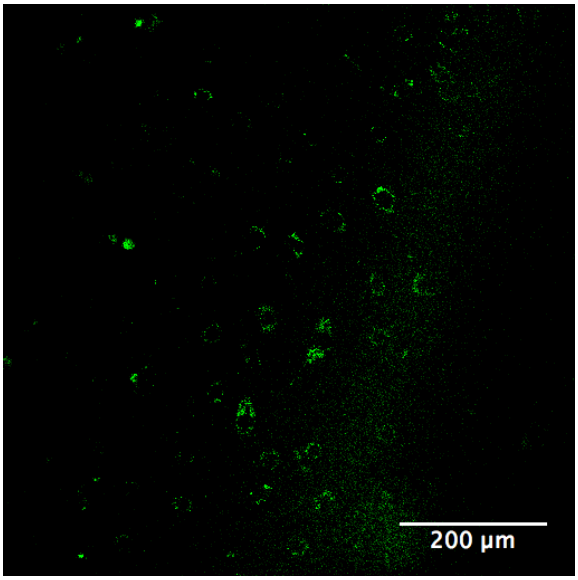

(a) GFP fluorescence signal was detected in most regions of the well.

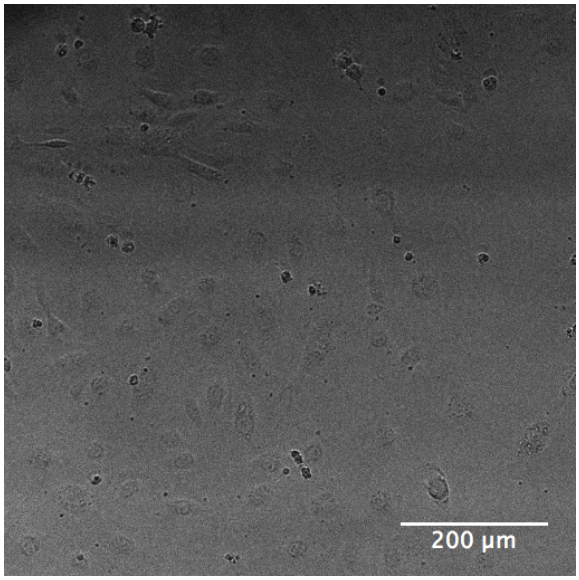

(b) Bright field image of the cells to the left. GFP-positive cells look realtively healthy.

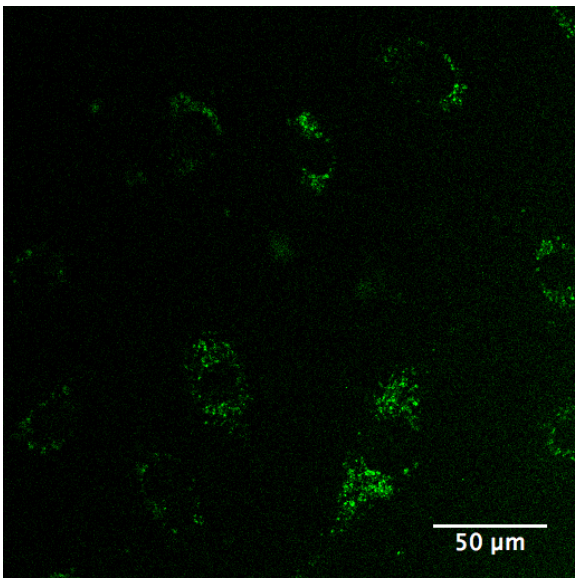

(c) GFP fluorescence signal imaged with a higher zoom factor.

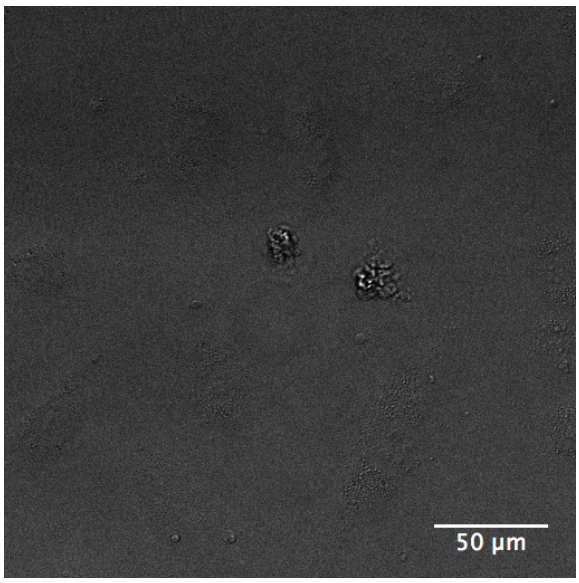

(d) Bright field image of the cells to the left. The cells are poorly visible at this zoom actor.

Figure 50: **48h; GFP fluorescence and healthy cells** Images of cells transfected with 0.05μg DNA (GFP-tagged human β_3-integrin), ratio 3:1 of Lipofectamine® 2000 : DNA, 48 h after transfection (n = 1). The images represent the result found for all six combinations 0.05μg DNA, ratio 3:1 and 0.5:1, and 0.1μg DNA, ratio 5:1, 3:1, 1:1 and 0.5:1 of Lipofectamine® 2000 : DNA.

4.11.2 Real-time imaging of NE incubation of transfected cells

After examining the successfulness of the nine transfection protocols 48 h after transfection, an initial test experiment of real-time imaging of NE incubation of transfected cells was performed. In this test experiment, uptake of NE in transfected cells seemed to occur in similar manners as for cells with no cell staining (presented in section 4.10.1). However, GFP-tagged β_3-integrins appeared to be expressed mainly intracellularly.

Images showing a merge of the rhodamine-PE (green) and GFP (red) fluorescence signals from the 30 min time series, are presented in figure 51. Where the fluorescent signals overlap, the colour is yellow. The images from each fluorophore separately, are presented in appendix C. Capturing of the time series was initiated 15 min after addition of NE. Therefore, this time series shows images from later time points of NE-incubation than previous time series. The focal plane for imaging was chosen where the GFP fluorescence signals were brightest. This plane was closer to the substrate than in previous time series presented, hence the cells are not as clearly visualised in the rhodamine-PE fluorescence images here as previously. However, in this focal plane, the bright field images clearly visualised the cells, and are presented in figure 52.

The 30 min time series was captured with an objective with a larger magnification than when assessing the successfulness of transfection for the nine different protocols. When observing the GFP fluorescence signal at a larger magnification and over time, the actual cellular position of the GFP-tagged β_3-integrins became clearer. The GFP fluorescence signals were visible in fluorescent spots which moved around within the cell areas, and were very similar to fluorescent spots representing NE, observed both in this and in previously described experiments. Also, in the merge in figure 51, several of the fluorescent spots are yellow, hence both GFP-tagged β_3-integrin and RHO-NE were positioned at these locations. The cell circumferences in the focal plane were clearly visible in the bright field images, but the GFP fluorescence signals did not clearly mark these circumferences. A similar pattern of GFP fluorescence was observed prior to addition of NE.

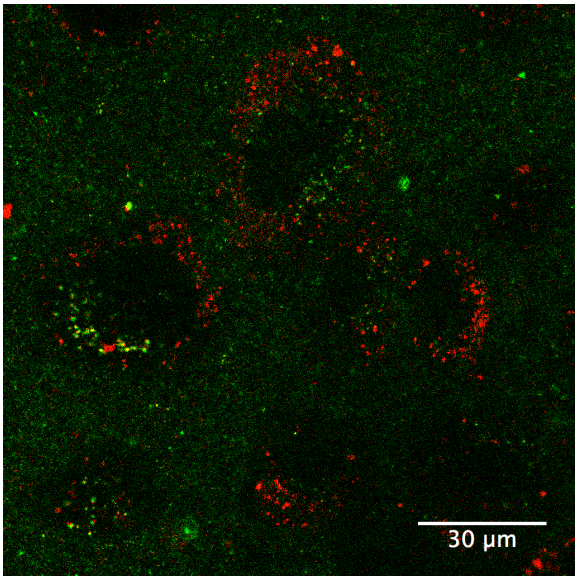

(a) First image of the timeseries, ∼ 15 minutes after addition of NE

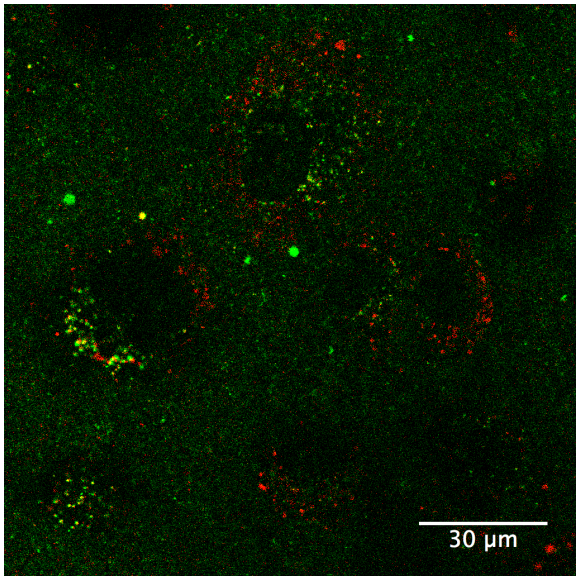

(b) 10 minutes after initiation of the timeseries. 25 minutes after addition of NE.

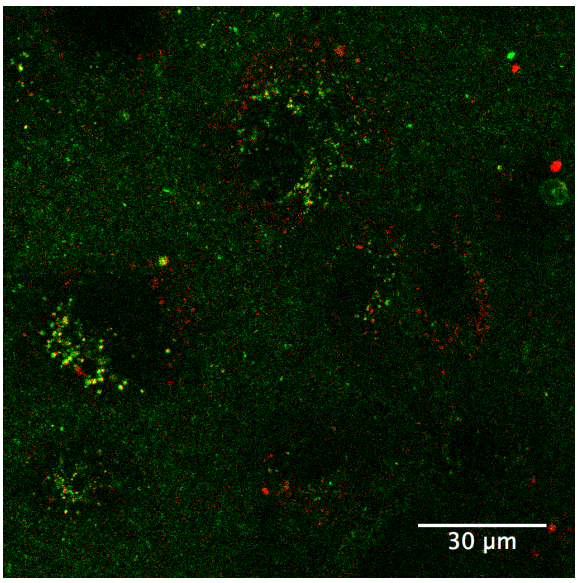

(c) 20 minutes after initiation of the timeseries. 35 minutes after addition of NE.

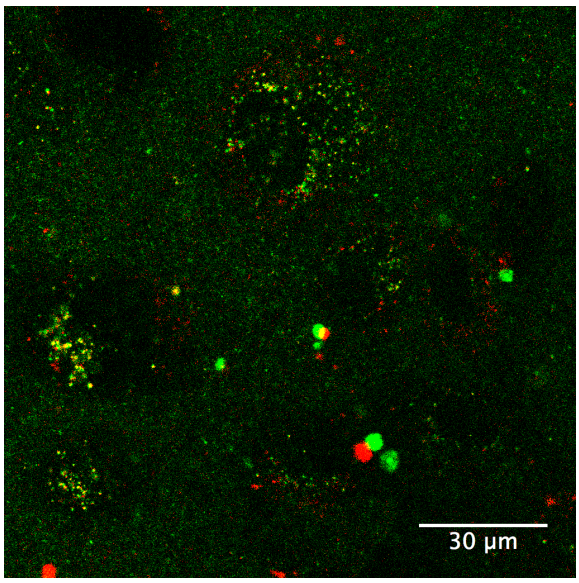

(d) 30 minutes after initiation of the timeseries. 45 minutes after addition of NE.

Figure 51: **Incubation of transfected cells with RGD-RHO-NE** Four snapshots from a 30 min time series of HUVEC incubated with 1 mM RGD-RHO-NE captured on a confocal microscope. Cells were transfected with 0.05 μg of DNA (GFP-tagged human β_3-integrin), ratio 0.5:1 of Lipofectamine® 2000 : DNA 48 h prior to incubation. The images show a merge of the rhodamine-PE (green) and GFP (red) fluorescence channels. Where the red and green fluorescence signals overlap, the colour is yellow. n = 1.

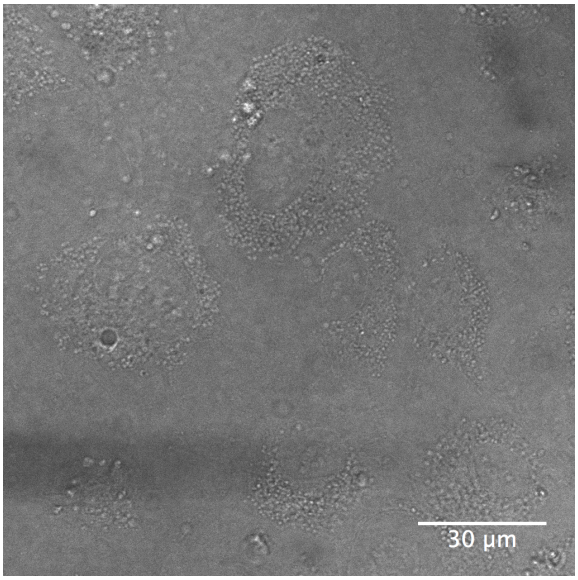

(a) First image of the timeseries, $\sim$ 15 minutes after addition of NE

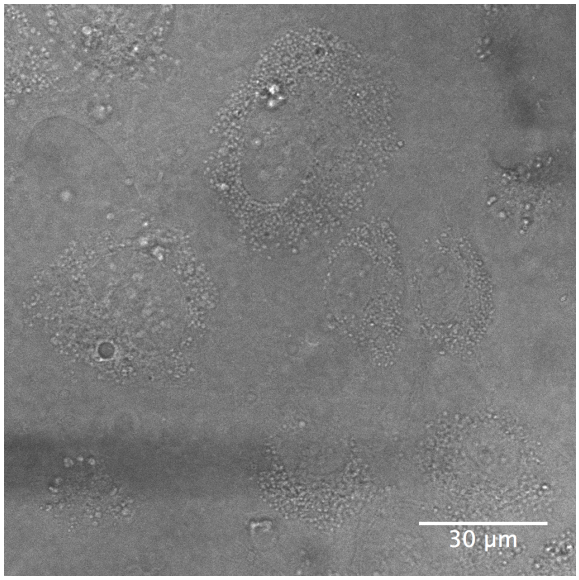

(b) 10 minutes after initiation of the timeseries. 25 minutes after addition of NE.

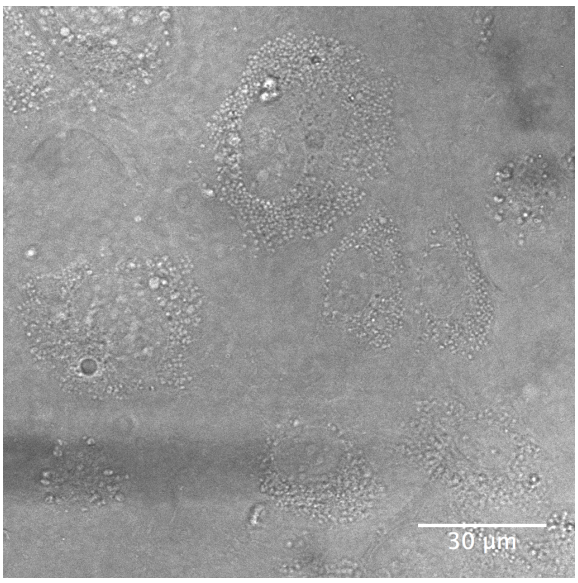

(c) 20 minutes after initiation of the timeseries. 35 minutes after addition of NE.

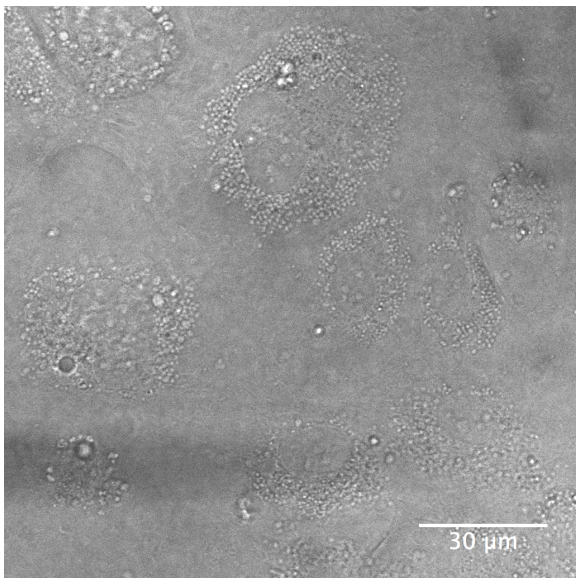

(d) 30 minutes after initiation of the timeseries. 45 minutes after addition of NE.

Figure 52: **Incubation of transfected cells with RGD-RHO-NE** Four snapshots from a 30 min time series of HUVEC incubated with 1 mM RGD-RHO-NE captured on a confocal microscope. Cells were transfected with 0.05 μg of DNA (GFP-tagged human β_3-integrin), ratio 0.5:1 of Lipofectamine® 2000 : DNA 48 h prior to incubation. The images show bright field images. n = 1.

5 Discussion

5.1 Introductory studies for FCM experiments

5.1.1 Interpretation of flow cytomteric data

Raw data from the leakage studies were presented to provide a better understanding of results from flow cytometry experiments in general. In the raw data, the shift of histograms representing NE-incubated samples compared to the autofluorecent sample, was small. It may be discussed if these small shifts significantly differ from the autofluorescent sample, and thereby if an effect of NE-incubation may be concluded. However, with more fluorophores incorporated per NE, the fluorescence intensity per cell would also increase, and the histograms for NE-incubated samples would shift further to the right. Thereby, both percentage of positive cells and MFI would increase, and it would be easier to make a conclusion about the effect of NE-incubation. For further experiments, it could therefore be benefitial to incorporate more fluoropohores per NE.

As presented in section 3.3.8, the cell count varied between 4 000 and 10 000 cells per sample. Different cell counts produce different cellular fluorescence intensity distributions. A higher count gives a more representative distribution, and thereby more reliable read-out values. This, in combination with the relatively small shifts in histograms compared to autofluorescence, makes it necessary to avoid interpreting too much into small variations in data values. Therefore, interpretation of results from flow cytometry experiments in this thesis will mainly be based on the overall trends observed in the data series, and not focus on data points deviating from the trend. As presented in section 4.1, absolute values of results will not be emphasised either, as there will always be batch-to-batch variations in payload of fluorophores in NE, cell confluency on the day of experiments, etc.

5.1.2 Studies of fluorophore leakage

Uptake and surface binding of NE was in this thesis studied by fluorescently labelled NE. An important source of error in such experiments, would be leakage of fluorescent labels from NE to cells [88]. In the study of fluorophore leakage, no leakage was observed for RAD-NE for either of the two fluorescent labels utilised (rhodamine-PE and Nile Red 668). For RGD-NE, possibly a small leakage of fluorophores was detected.

The occurence of leakage was studied at 4°C. As endocytosis is an energy-dependant process [89, 85], it is strongly inhibited at 4°C. This hinders uptake of NE and only allow increase in cellular fluorescence intensities due to surface binding of NE or leakage of fluorophores. In the conduction of experiments, it was assumed that saturation binding of surface $\alpha_v\beta_3$-integrins would occur within 15 min at 4°C. Under this assumption, the increase in relative MFI and percentage of positive cells from 15 to 60 min incubation for RGD-NE, should not represent surface binding and thereby indicate leakage of fluorophores. Leakage for RGD-NE, but not RAD-NE is likely to occur, as

RGD-NE bind to $\alpha_v\beta_3$ on the cell surface. RAD-NE may bind unspecifically, but more RGD-NE are likely kept close to the cell membrane at any time. Contact is needed for transfer of lipids (rhodamine-PE) and hydrophobic molecules (Nile Red 668) to the cell membrane [88], hence more leakage for RGD-NE is likely. If the assumption of saturation binding of surface $\alpha_v\beta_3$-integrins within 15 min, is not correct, the increase in fluorescence intensity from 15 to 60 min is most likely caused by additional surface binding of RGD-NE, indicating no leakage.

The contribution from fluoropohore leakage and additional NE surface binding to increased fluorescence intensitites from 15 to 60 min, may not be determined from current experiments. However, the potential small leakage of RGD-NE observed was significantly lower than the uptake of RGD-NE (studied at 37°C) observed in the same time frame for both RHO- and NR-NE. This, together with the fact that further experiments will be performed with shorter incubation periods, led to the conclusion that the small potential leakage of fluorophores from RGD-NE to cells, will not pose a problem in further experiments.

5.1.3 Introductory studies for immunolabelling of surface $\alpha_v\beta_3$-integrin

In this project, we wanted to determine $\alpha_v\beta_3$ surface expression after NE-incubation and on cells of different confluency. $\alpha_v\beta_3$ surface expression was determined by immunolabelling. Immunolabelling was performed on ice to inhibit endocytosis [89, 85], and thereby only label surface $\alpha_v\beta_3$-integrins. To be able to label surface $\alpha_v\beta_3$-integrins immediately after NE-incubation in coming experiments, immunolabelling was performed on adherent cells, and cell detachment was performed after labelling. After labelling, it would be preferable to avoid increasing the temperature or adding reagents to the samples, as this could alter the labelling signal. Higher temperatures could e.g. allow more detachment of surface-bound antibodies than on ice, due to higher thermal energy. Trypsin, which is often used to detach adherent cells, is an enzyme which causes cell detachment by degrading adherent surface molecules [90]. Due to protein degradation, addition of trypsin may significantly affect the integrity of antibodies and $\alpha_v\beta_3$-integrins. Another detachment chemical EDTA, on the other hand, cause cell detachment due to its chelating properties. EDTA bind Ca^{2+}-ions, and thereby prevent cell-adhesion by calcium-dependant cell-adhesion molecules [91]. Thereby, no protein degradation should occur with EDTA, but longer incubation at elevated temperatures is typically needed.

Cell detachment by scraping, trypsination and EDTA were compared to find the most suitable method for our experiments. Scraping may be performed without both temperature rising and reagents, and would be the preferable detachment method. However, scraping produced a negligable cell population, indicating few detached cells. Also, small FS (forward scatter) values were detected, indicating cellular debris, hence cellular disruption due to scraping. This method was therefore found not suitable.

Results were similar for detachment by EDTA and trypsin (37°C). This indicates that trypsin does not degrade proteins which affect the results for secondary antibody fluorescence. Based on this, EDTA and trypsin becomes equally suitable for detachment in our experiments. As detachment by EDTA required 25 min at 37°C, while trypsin

only required 2-3 min, trypsination was selected as the most suitable method, to reduce the time period at higher temperatures. The fluorescence intensity histogram for trypsin was slightly right-shifted compared to EDTA. This may represent random variations. However, as both parallels showed the same result, this may also indicate that it could be caused by release of antibodies during the long period at 37°C, for EDTA samples.

From the comparison of immunolablling with concentrations 0.3μg/100μl and 1μg/100μl of primary antibody, no difference in secondary antibody fluorescence was found. This indicates that the lowest concentration is adequate to saturate surface $\alpha_v\beta_3$-integrins, and this concentration was utilised in further experiments.

5.1.4 Correlation between cell confluency, $\alpha_v\beta_3$ surface expression and NE uptake

As presented in section 2.8, non-proliferating endothelial cells *in vitro* have significantly reduced expression of $\alpha_v\beta_3$-integrins compared to proliferating endothelial cells [73]. Also, cells reduce or stop proliferating in the plateau-phase of cell culturing where they reach 100% confluency [72]. Therefore, cells at different confluency were here used to study the correlation between cell confluency, $\alpha_v\beta_3$ surface expression and uptake of NE.

A reduction in surface expression of $\alpha_v\beta_3$ was observed with increasing cell confluency, both 3 and 4 days after seeding. However, samples which appeared $\sim 100\%$ confluent on the day of experiments, only showed a reduction in relative MFI of $\sim 25\%$ compared to cells at lowest cell density. This might indicate that most cells were developing towards non-proliferation with initiating reduction in $\alpha_v\beta_3$ expression, but very few cells had actually reached the actual non-proliferating state. This might also indicate that samples evaluated by us to be $\sim 100\%$ confluent, did in fact still have remaining space for the cells to occupy.

In accordance with this, 4 days, but not 3 days after seeding, the reduction in $\alpha_v\beta_3$ surface expression became slightly visible in the value for percentage of positive cells. Hence, 4 days after seeding, a few cells in the samples of highest confluency, expressed so low levels of $\alpha_v\beta_3$ that they were regarded non-positive. This indicates that these few cells have reached the fully non-proliferating state with very low $\alpha_v\beta_3$ expression. This also indicates that a greater extent of non-proliferating cells may most likely be obtained by culturing cells even longer.

Further, to study the correlation between $\alpha_v\beta_3$ expression and NE uptake, cells of the same density used to determine $\alpha_v\beta_3$ surface expression, were incubated with NE (4 days after seeding). Incubation with targeting RGD-NE showed a relative decrease in NE uptake with increasing confluency, which was very similar to the relative decrease in $\alpha_v\beta_3$ surface expression for cells of the same confluencies. In accordance with [9, 41, 85], this is a strong confirmation that RGD-NE uptake is highly dependant on the surface expression of $\alpha_v\beta_3$. As confluency affects RGD-NE uptake, this emphasises the importance of cell confluency when performing uptake studies and that caution is needed when comparing quantitative values of uptake between experiments.

For non-targeting RAD-NE, no effect of $\alpha_v\beta_3$ expression was observed. This confirms that RAD-NE is a strong negative control when investigating interactions between $\alpha_v\beta_3$ and RGD peptide, in accordance with [9, 41, 85]. This statement is also supported by the fact that uptake of RAD-NE was significantly lower than RGD-NE throughout the experiments performed in this project.

5.2 Investigating the recycling hypothesis

The overall aim of this part of the project was to investigate *in vitro* if the hypothesis proposed by Hak et al. [9], concerning receptor recycling kinetics as a cause of observed *in vivo* targeting kinetics of RGD-conjugated NE, may in fact be correct. This hypothesis is presented in section 2.4.2, and illustrated in figure 6 in the same section.

5.2.1 Saturation studies of RGD-to-surface-$\alpha_v\beta_3$ binding

In their hypothesis, Hak et al. [9] suggested the majority of $\alpha_v\beta_3$-integrins would be bound and internalised within minutes upon RGD-NE exposure. Saturation experiments were performed to verify that saturation binding of surface $\alpha_v\beta_3$-integrins occurs fast. As the formation of vesicles for endocytosis takes time (e.g. the formation of a clathrin coated vesicle typically takes up to 2 min [92]), and surface binding has to precede this, we assumed mainly surface binding of RGD-NE would occur in the selected time frame of incubation.

Within 2.5 min, saturation binding was observed for RGD-NE of concentrations above 0.1 mM. Although the exact time of saturation for each concentration may not be established, we may conclude that for concentrations above 0.1 mM, saturation binding occurs in 2.5 min or less, in accordance with [9]. Also in accordance with [9], no saturation was observed for RAD-NE. However, above 0.1 mM, a small linear increase in fluorescence intensity was observed. This may have different causes, e.g. unspecific surface binding or actual uptake of NE even at this short time frame. Both suggestions will be more extensive with more NE available, and could thereby explain the increase with concentration.

Although we in this experiment assumed mainly surface binding, it is important to note for flow cytometry experiments in general, that actual NE uptake and surface-bound NE may not be distinguished. For these exact experiments, however, the appearance of the results and native differences between the process of surface binding and endocytosis indicate mainly surface binding of NE. Little NE uptake at this time frame is also supported by CLSM experiments with real-time imaging of NE-incubation, discussed in 5.3.2.

5.2.2 Incubation pause experiments

After fast saturation binding of surface $\alpha_v\beta_3$-integrins, Hak et al. [9] hypothesised that the majority of $\alpha_v\beta_3$-integrins would internalise within minutes upon RGD-NE exposure. Further, they hypothesised that the majority of these integrins would reappear on the cell surface at a similar time point post RGD-NE exposure. *In vitro* incubation pause experiments performed by Hak et al. support this hypothesis. We developed these incubation pause experiment further, to understand more about the underlying events of the observations.

Experiments by Hak et al. were successfully reproduced From experiments where we reproduced the exact *in vitro* experiments performed by Hak et al. (1 mM

RHO-NE), results were in compliance with Hak et al.'s results. Increasing fluroescence intensity was observed with increasing pause length for RGD-NE, while no clear effect of pause length was observed for RAD-NE. As presented by Hak et al. [9], this may be explained by binding and initiation of $\alpha_v\beta_3$-integrin internalisation during the first incubation period, followed by receptor recycling, before the second NE-incubation period. Longer pause, allows more receptors to recycle to the cell membrane, and become available for RGD-NE binding and internalisation in the second incubation period. RAD-NE do not interact with $\alpha_v\beta_3$-integrins. It is therefore expected that their uptake is not affected by $\alpha_v\beta_3$ surface expression.

Samples with the maximum florescence intensity observed (for a pause of 15 min) for RGD-NE, showed approximately twice the intensity observed for only 4 min incubation. This fits with the hypothesis, indicating 'all' internalised $\alpha_v\beta_3$ recycled back to the cell membrane during the 15 min pause, and were thereby ready to bind as many RGD-NE in the second incubation period as the first [9]. Except that Hak et al. used 12 min in stead of 15 min pause length, all observations made for 1 mM RHO-NE, were similar to the observations by Hak et al. This indicates that the experiment was successfully reproduced. This is an important finding prior to further development of the experimental setup, to eliminate sources of error.

0.9 mM NR-NE results are most likely non-representative Surprisingly, in experiments with 0.9 mM NR-NE, no increase in RGD-NE fluorescence intensity was observed with increasing pause length as for 1 mM RHO-NE. RHO-NE have the fluorophore on the surface, while NR-NE have it in the oil lumen of NE. As surface properties of nanoparticles may be crucial for biological interactions [14, 16, 20], RHO-NE and NR-NE may interact differently with HUVEC and produce different results. However, previous studies by Postdoc Sjoerd Hak (not published) have shown similar results for 1 mM RHO-NE and NR-NE. As experiments with 0.9 mM NR-NE was only performed once, it was therefore concluded that the observed results are most likely non-representative. An alternative explanation could be that a NE concentration of 0.9 mM is not adequate to induce the same effects on $\alpha_v\beta_3$-behaviour as 1 mM NE.

0.1 mM RHO- and NR-NE do not provide the same results as 1 mM RHO-NE When only analysing the same data points as included in all incubation pause experiments, results for 0.1 mM RHO-NE show no effect of pause length on fluorescence intensity of either RGD- or RAD-NE. The same was observed for 0.1 mM NR-NE. Previously, we found saturation binding of surface $\alpha_v\beta_3$-integrins to occur within 2.5 min for both 0.1 and 1 mM RGD-NE. By this, both concentrations should cause saturation binding before the first incubation period is ended (4 min), and according to the hypothesis, initiate internalisation of $\alpha_v\beta_3$-integrins, which later recycle back to the cell membrane [9].

As 0.1 and 1 mM RGD-NE produce different results, this might indicate that although saturation binding occurs for both during the first incubation period, the processes initiated by $\alpha_v\beta_3$-RGD-NE interactions, are concentration dependant. In accordance with this, the increase in fluorescence intensity from 4 min to 8 min incubation was found to be 50% for 1 mM RHO-NE by Hak et al. [9], while we found a 24 - 30%

increase for 0.1 mM. Different effects on $\alpha_v\beta_3$-function by different concentrations of RGD peptide, is also reported in the literature [48]. Differences between high and low concentrations of RGD peptide has even been shown to induce such opposing effects as antagonistic versus agonistic effects on $\alpha_v\beta_3$-integrin [48, 49]. This emphasises that multiple unknown factors and signalling pathways are participating in processes involving $\alpha_v\beta_3$-RGD interactions, which remain to be uncovered [44].

Increase in NE uptake with increasing pause does not seem to originate in the second incubation period In the hypothesis by Hak et al., the increase in NE internalisation with increasing pause, originates in the second incubation period due to higher numbers of recycled $\alpha_v\beta_3$-integrins [9]. To verify if this was in fact the cause of the observed increase, we performed incubation pause experiments with UL-NE in the first and RHO- or NR-NE in the second incubation period (UL + RHO/NR). By this, only internalised and surface-bound NE caused by the second NE-incubation period, were detectable.

Inconsistent with the recycling hypothesis [9], the NE fluorescence intensity obtained in the second incubation period was found to decrease with increasing pause length for RGD-NE, both for NR-NE (0.9 mM) and RHO-NE (1 mM). This could indicate that the increase in fluorescence intensity with increasing pause, is not caused by the second NE-incubation period, and that the hypothesis by Hak et al. is not correct. However, an interesting finding in these experiments was that the fluorescence intensity for RAD-NE also decreased with increasing pause lenght, in at least some of the parallels performed. This might indicate that the decrease in fluorescence intensity for RGD-NE with increasing pause, is not (at least not only) a result of interactions between $\alpha_v\beta_3$-integrins and RGD-NE. This highlights the fact that there are several ongoing processes that are not fully understood.

An alternative explanation for the unexpected results could be, as suggested previosuly, that NE interactions with HUVEC differ between types of NE due to different surface properties [14, 16, 20]. If UL-NE do not induce the same effects on $\alpha_v\beta_3$-behaviour (receptor activation, internalisation, etc.) as RHO- or NR-NE, experiments with UL-NE may not be used to elaborate on the processes taking place with the same type of NE in both incubation periods.

In experiments where cells were incubated with RHO-NE in the first and UL-NE in the second incubation period (1 mM, RHO + UL), only uptake and surface-binding of NE caused by the first incubation were detectable. Here, an increase in fluorescence intensity for RGD-NE with increasing pause was observed. No effect of pause length was observed for RAD-NE. Interestingly, this suggest that an increase in fluorescence intensity for RGD-RHO-NE with increasing pause may be caused solely by the first NE-incubation.

For these experiments (RHO + UL), as for UL + RHO/NR, the results are not in line with the hypothesis by Hak et al. Nevertheless, the fact that an increase in fluorescence intensity is observed for RHO + UL, and a decrease is observed for UL + RHO, could be combined to provide an overall increase in fluorescence intensity as observed for RHO + RHO. From this, one could argument that the different types of NE most likely do interact similarily with HUVEC, and that experiments with UL-NE may be

used to study the uptake and surface binding due to each incubation period separately. In the further discussion, this is assumed.

Wrong time frame of the hypothesis? Due to limited time, RHO-NE at concentration 1 mM was the only NE type and concentration where uptake caused by both incubation periods together, and by the first and second incubation periods separately, were studied. As experiments were mostly performed in duplicates, no conclusions may be drawn from this. However, if the observed data are representative, they would indicate that the increase in fluorescence intensity of RGD-NE observed for RHO + RHO, is caused by the first incubation period. The first 4 min of NE-incubation should proceed similarily for all samples. Hence, the differences in observed fluorescence intensities, most likely occur during the time of the varying pause (and the second incubation), but occurs *due to* the first incubation period. Further, uptake and surface binding due to the second incubation period, for some reason decrease with increasing pause.

The fact that results from experiments with UL-NE are not in compliance with the hypothesis proposed by Hak et al., could indicate that receptor recycling is not the cause (at least not the only cause) of observed *in vivo* targeting kinetics. Alternatively, it could indicate that these *in vitro* studies are not representative for the processes taking place *in vivo*. Results obtained *in vitro* have numerous times been shown non-applicable for *in vivo* studies [93].

In total, the incubation pause experiments have provided many results which are difficult to explain. An especially peculiar observation, was that for RGD-RHO-NE (1 mM), incubation with RHO-NE for only 4 min provided higher fluorescence intensities than incubation with RHO-NE (4 min), varying pause, and incubation with UL-NE (4 min) toghether (incubation pause samples). This appears strange, as all incubation pause samples should seemingly have similar relative MFI as the sample only incubated 4 min, after their RHO-NE incubation. Thereafter, relative MFI would need to decrease during the pause and incubation with UL-NE, to end up at lower relative MFI.

One highly relevant explanation for the unexpected results in incubation pause experiments, could be that processes initiated by interactions between $\alpha_v\beta_3$-integrins and RGD-NE may proceed at different time frames than according to the hypothesis. The incubation pause experiments are highly dependant on the correct timing. Hence, a misconception of the time frame of processes may easily provide contrasting results.

A misconception of the time frame of $\alpha_v\beta_3$ internalisation could e.g. explain the peculiar results for RHO + UL samples compared to 4 min RHO-NE incubation. If $\alpha_v\beta_3$ internalisation occurs slower than expected from the hypothesis, RGD-RHO-NE bound to surface $\alpha_v\beta_3$-integrins from the first incubation period may not all be internalised when the second incubation starts. This could cause competitive binding of $\alpha_v\beta_3$-integrins by RHO-NE and UL-NE, and some of the surface-bound RHO-NE could be exchanged with UL-NE, decreasing the overall fluorescence intensity of the cells. With increasing pause length, increasing number of surface-bound RHO-NE would have time to internalise, and 'protect' itself from competitive binding, hence preserving more of the RHO-NE fluorescence from the first incubation period.

If $\alpha_v\beta_3$ internalisation occurs slower than expected from the hypothesis, the increase in fluorescence intensity due to the first incubation period could also be partially explained. If surface-bound RGD-NE do not all internalise during the first incubation period, remaining surface-bound RGD-NE could somehow cause the variations in results during the pause and second incubation.

The suggestion of a wrong time frame is not unlikely. The time frame of receptor binding, internalisation and recycling suggested in the hypothesis by Hak et al., was based on *in vivo* experimental observations, together with findings of recycling half-life of $\alpha_v\beta_3$-integrins determined in *in vitro* experiments reported in the literature (3 min for 'short-loop' and 10 min for 'long-loop' recycling pathways [44, 54]). Determination of $\alpha_v\beta_3$ recycling half-life reported in the literature, are obtained under certain experimental conditions. Study of recycling pathways of $\alpha_v\beta_3$-integrins are for example, often reported to be performed in serum-starved cells [94, 95, 96]. Serum starvation is a debated technique, which is used by many to reduce basal activity of cells. However, others use serum starvation to study cellular stress response, autophagy and apoptosis, or to stimulate particular pathological conditions. Serum starvation is by this, an event which may trigger various divergent responses, and therefore has great potential to interfere with experimental results [97]. Other specific experimental conditions may also sigificantly affect the results obtained in different studies, and recycling half-lifes of $\alpha_v\beta_3$ presented in the literature, do not need to apply in our experiments. In addition, recycling pathways of $\alpha_v\beta_3$ may be affected by binding and (co-)internalisation of RGD-NE [44, 54, 98]. Also, the hypothesis by Hak et al. suggests that the majority of internalised $\alpha_v\beta_3$-integrins return to the plasma membrane as a pool. This implies that the majority of internalised $\alpha_v\beta_3$ are recycled through the same pathway, which does not need to be the case [44, 54, 98].

An important assumption in the hypothesis by Hak et al. is that binding of RGD-NE induce rapid internalisation of the majority of $\alpha_v\beta_3$-integrins. However, this was not tested. As presented in section 2.4.3, several monovalent RGD peptides have been shown to bind $\alpha_v\beta_3$-integrins without inducing $\alpha_v\beta_3$ internalisation [58, 99]. Hence, the assumption of internalisation within minutes upon NE exposure may be wrong. Even if RGD-NE *do* induce $\alpha_v\beta_3$ internalisation, this process may take longer than 4 min as assumed in incubation pause experiments, and all $\alpha_v\beta_3$-integrins do not necessarily internalise simultaneously as a pool.

5.2.3 Expression of surface $\alpha_v\beta_3$-integrins after incubation with nanoemulsions

To investigate the assumption of rapid $\alpha_v\beta_3$ internalisation induced by RGD-NE binding in the hypothesis by Hak et al., the surface expression of $\alpha_v\beta_3$ after incubation with NE for varying periods, was studied.

Reliability of the method The quantification of $\alpha_v\beta_3$ surface expression in these experiments, was performed by immunolabelling with primary and secondary antibodies. The fact that both RGD-NE and primary antibodies were to bind $\alpha_v\beta_3$-integrins, may pose a problem in these experiments, as immunolabelling may be inhibited by

bound RGD-NE. As presented in section 3.1, the primary antibody does not interact immediately with the RGD binding site, but rather serve as an allosteric inhibitor [77]. This indicates that the primary antibody could get access to its binding site although the RGD binding site was occupied. As it is highly likely that the binding affinity of the antibody is higher than the RGD peptide [85], it is most likely that the antibody managed to 'take over' $\alpha_v\beta_3$ binding. If so, this surface quantification protocol is not problematic. However, as we may not be certain of this, other methods to quantify $\alpha_v\beta_3$ surface expression should be developed for further work. In the following discussion, it is assumed that primary antibodies bind all surface $\alpha_v\beta_3$-integrins during the period of labelling, disregarding their RGD-occupancy state before immunolabelling.

Do RGD-NE affect $\alpha_v\beta_3$ internalisation? The surface expression of $\alpha_v\beta_3$-integrins immediately after NE-incubation, was found to decrease with increasing NE-incubation period for RGD-NE, but maximally a 25% decrease was found. This extent of decrease indicate that the assumption of rapid internalisation of the *majority* of surface $\alpha_v\beta_3$-integrins in the hypothesis by Hak et al., is likely not correct. For RAD-NE, no clear effect or a smaller reduction in surface expression was found. Interestingly, in both parallels performed, $\alpha_v\beta_3$ surface expression first clearly differed between RAD- and RGD-NE incubation, in cells incubated for 10 min or longer. This indicates that the binding of RGD-NE to $\alpha_v\beta_3$-integrins may induce internalisation of integrins, but seemingly only after more than 10 min incubation time. By assuming co-internalisation, this is in compliance with results from real-time imaging of NE-incubation, where NE uptake was first visible after 10 - 15 min.

The fact that the surface expression of $\alpha_v\beta_3$ was similar after 5 min incubation with RAD- and RGD-NE, have important implications for the incubation pause experiments. Seemingly, during a time frame of 5 min, binding of RGD-NE to $\alpha_v\beta_3$-integrins do not promote $\alpha_v\beta_3$ internalisation, to any greater extent than incubation with non-binding RAD-NE. From this, the assumption that the majority of $\alpha_v\beta_3$ will be bound and internalised within the first incubation period of 4 min, is highly unlikely. Surface-bound RGD-NE may continue affecting $\alpha_v\beta_3$-behaviour in the incubation pause, and thereby induce $\alpha_v\beta_3$ internalisation during this time. However, depending on the time frame again, significant parts of or the whole incubation pause will in this case be used for inducing internalisation, in stead of allowing time for recycling of $\alpha_v\beta_3$-integrins. Naturally, this will cause different results than predicted from the hypothesis.

Once, $\alpha_v\beta_3$ surface expression was tested both immediately after and 20 min after NE-incubation. The surface expression of $\alpha_v\beta_3$ was found to be lower 20 min after, compared to immediately after NE-incubation. Based on the starting hypothesis of rapid internalisation of the majority of surface $\alpha_v\beta_3$, followed by a recycling time with a half-life of 3 or 10 min [9, 44, 54], the $\alpha_v\beta_3$ surface expression was expected to increase during the 20 min 'recovery time'. As the opposite was observed, this further suggests that the starting hypothesis is not correct.

The reduction in $\alpha_v\beta_3$ surface expression 20 min after RGD-NE-incubation compared to immediately after, is in compliance with the suggestion of a different time frame of $\alpha_v\beta_3$ internalisation than originally thought. After 5 min NE-incubation, the surface expression is altered only slightly, but 20 min later, signalling processes causing $\alpha_v\beta_3$-

internalisation have had sufficient time to occur. However, the decrease in surface expression of $\alpha_v\beta_3$ 20 min after, compared to immediately after NE-incubation, was similar for RGD- and RAD-NE. This suggest that this decrease is not caused by specific interactions between $\alpha_v\beta_3$ and RGD-NE.

From the number of experiments performed, it is not possible to conclude on the effect of RGD-NE binding on $\alpha_v\beta_3$-function. From the current results, the two most likely suggestions are that RGD-NE binding does not affect $\alpha_v\beta_3$ internalisation, or RGD-NE binding does affect $\alpha_v\beta_3$ internalisation, but slower than originally hypothesised.

A possible explanation of no effect of RGD-NE binding on $\alpha_v\beta_3$ internalisation, is that the NE are conjugated to monovalent RGD peptides. As presented in section 2.4.3, $\alpha_v\beta_3$-integrins tend to cluster upon ligand binding [55, 58]. Also, from the information presented in section 2.4.3, it appears that species presenting several RGD peptides in a distance suitable for binding several clustered $\alpha_v\beta_3$-integrins, are both more efficiently taken up into the cell, and tend to induce increased internalisation of $\alpha_v\beta_3$-integrins, while monovalent RGD does not [56, 50, 58, 55]. An example of this is the multivalent RAFT(c[-RGDfK-])$_4$ developed by Boturyn et al. [57], which was shown to increase $\alpha_v\beta_3$ internalisation, while the monovalent c[-RGDfK-] internalised without modifying $\alpha_v\beta_3$ internalisation in HEK293(β_3) cells [58]. In fact, the RGD peptide conjugated to NE in our studies, is also c[-RGDfK-] (equipped with a thioacetyl group for conjugation), further strengthening the credibility of this explanation.

In spite of this, the possibility that RGD-NE *do* induce $\alpha_v\beta_3$ internalisation, but slower than originally hypothesised is still present. c[-RGDfK-] was shown to internalise without modifying $\alpha_v\beta_3$ internalisation in HEK293(β_3). However, with the diversity of cellular processes and signalling pathways integrins participate in and are affected by [7, 48, 44, 54, 98], the response may vary between cell types, and c[-RGDfK-] conjugated to NE does not necessarily induce the same response as non-conjugated c[-RGDfK-].

To the knowledge of the author, not much has been published on the time frame of $\alpha_v\beta_3$ internalisation upon ligand binding, for ligands which manage to induce such internalisation. Therefore, if the suggested time frame of internalisation in the hypothesis by Hak et al. lies at a probable order of magnitude, is difficult to state. If the suggested time frame *does* lie at 'normal' internalisation rates (if such exist) for e.g. multivalent RGD peptides which has been shown to induce $\alpha_v\beta_3$ internalisation, an explanation of why RGD-NE do not induce internalisation as fast as expected, could again be found in RGD multivalency. As RGD peptides are conjugated to lipids in the NE membrane, these RGD peptides are free to diffuse throughout the NE membrane. If one RGD peptide bind to an $\alpha_v\beta_3$-integrin, diffusion could coincidently with time transport another RGD peptide close to this interaction point. If $\alpha_v\beta_3$ have started clustering due to the activation from initial ligand binding [55], the second RGD could bind to another of the clustered $\alpha_v\beta_3$. By this, binding of several clustered $\alpha_v\beta_3$ by RGD peptides on RGD-NE is possible, and may induce the same effects as other multivalent RGD species [55, 56, 58]. However, as it requires diffusion of RGD peptides, it may take longer time.

In the studies by Guo et al. [55], liposomes were conjugated both to monovalent RGD (moRGD-LP) and divalent RGD with proper RGD-distance to bind two clustered $\alpha_v\beta_3$

simultaneously (P-diRGD-LP). Here, the targeting efficiency in B16-tumor bearing mice, was about 2.4-fold better for P-diRGD-LP than moRGD-LP at 3h. $\alpha_v\beta_3$-integrin internalisation was not studied in these experiments, so no direct implications may be made. However, the resembling nature of lipid-based nanoparticles suggest that diffusion of RGD peptide should be equally likely in liposomes in these experiments, as in NE in our experiments. As the targeting efficiency was better for P-diRGD-LP at 3 h, this suggest that if diffusion of monovalent RGD causes binding of $\alpha_v\beta_3$ clusters, it does not occur as extensively as cluster binding by multivalent RGD peptides.

5.2.4 Concluding remarks and further work for the recycling hypothesis

In this work, we have shown that, in compliance with the hypothesis by Hak et al. [9], saturation binding of surface $\alpha_v\beta_3$-integrins by RGD-NE, occurs within minutes upon exposure to NE. However, results from both incubation pause experiments and determination of $\alpha_v\beta_3$-surface expression after NE-incubation, indicate that either RGD-NE induce $\alpha_v\beta_3$ internalisation at a longer time frame and less extensive than proposed by Hak et al., or RGD-NE do not induce $\alpha_v\beta_3$ internalisation at all. This is not in compliance with the hypothesis. Concerning recycling time for $\alpha_v\beta_3$-integrins in these experiments, not much may be said.

From the results in this thesis, conclusions concerning each step of the hypothesis may not be made. However, especially through the incubation pause experiments, it may be suggested that the *overall time frame* of the three components of $\alpha_v\beta_3$ surface binding, internalisation and recycling as a pool of integrins in the hypothesis, is not likely to be correct. RGD-NE may still induce internalisation and receptors may recycle more or less like a pool, returning to the cell membrane at a similar time point. However, this does not occur at the necessary time frame to make these kinetics responsible for the observed *in vivo* targeting kinetics. To conclude, if these *in vitro* studies are applicable to *in vivo* situations, it appears like the observed *in vivo* targeting kinetics are most likely not caused by kinetics of receptor recycling, as proposed by Hak et al.

For further studies of RGD-NE targeting kinetics, it will be important to determine whether RGD-NE are simply co-internalised with $\alpha_v\beta_3$ in their constitutive recycling process, or if binding of RGD-NE to $\alpha_v\beta_3$-integrins induce $\alpha_v\beta_3$ internalisation. If $\alpha_v\beta_3$ internalisation is induced, the time frame and extent of internalisation should be determined, as this is important for the overall targeting efficiency. If immunolabelling of surface $\alpha_v\beta_3$-integrins should be further utilised to determine $\alpha_v\beta_3$ internalisation, an antibody against $\alpha_v\beta_3$ which does not interfere with RGD-binding should be used to reduce possible sources of error. The antibody used in this study was simply used due to availability. Alternatively, a different method to determine extent of $\alpha_v\beta_3$ internalisation could be utilised. For example, Sancey et al. [58] developed a special enzyme-linked immunosorbent assay (ELISA) to demonstrate if RGD peptides induced $\alpha_v\beta_3$ internalisation or not.

If RGD-NE are found to induce internalisation of $\alpha_v\beta_3$, it would further be interesting to study if RGD-NE manage to bind clusters of $\alpha_v\beta_3$. This could give a pinpoint towards how RGD-NE induce $\alpha_v\beta_3$ internalisation. The virus Adenovirus 2, for example, which has been shown to bind clusters of $\alpha_v\beta_3$ with its penton base (five clustered

RGD), has been shown to induce signals, including activation of PI3 kinase, $p130^{CAS}$, and Rho GTPases, that are important for rearrangements in the actin cytoskeleton and initiation of internalisation [56, 51]. If cluster binding is found for RGD-NE, a similar signalling pathway might be applicable. Understanding the mechansim of internalisation is important to understand the overall targeting kinetics. Further, it is important to be able to develop more suitable RGD-based candidates for clinical purposes [48].

After internalisation, it would be interesting to determine at what time frame internalised $\alpha_v\beta_3$ return to the cell membrane. Although the time frame of receptor kinetics do not seem to be as hypothesised by Hak et al., receptor recycling may still have important implications for administration of RGD-conjugated therapeutics and contrast agents. By knowing the kinetics of receptor recycling upon NE exposure, dosage regimes for therapeutics may be tailored to reduce both side-effects and cost. Also, for molecular imaging with RGD-NE, knowledge about receptor recycling may be important to quantify integrin expression levels and for image interpretation [6].

If RGD-NE are not found to induce $\alpha_v\beta_3$ internalisation, the conjugation of multivalent RGD peptides to the NE could be tested. As clustering of $\alpha_v\beta_3$, and binding of clustered $\alpha_v\beta_3$, seems to be important features leading to increased $\alpha_v\beta_3$ internalisation [41, 55, 56, 58], the conjugation of multivalent RGD peptides with the correct distance apart, has the potential to significantly improve *in vivo* NE targeting efficiency, and enhance the efficacy of treatment. For example the RAFT(c[-RGDfK-])$_4$ developed by Boturyn et al. [57], which has been indicated to induce $\alpha_v\beta_3$ clustering and shown to induce $\alpha_v\beta_3$ internalisation upon binding, could be tested. For these new NE, the same studies suggested for RGD-NE would then be interesting to perform.

5.3 Establishing a protocol to monitor NE- and $\alpha_v\beta_3$-distribution

The overall aim of this part of the project was to develop an experimental protocol based on confocal laser scanning microscopy, where the cellular distribution of $\alpha_v\beta_3$-integrins and RGD-conjugated NE, could be monitored during NE-incubation, to study internalisation and recycling kinetics of $\alpha_v\beta_3$-integrins, and internalisation and intracellular trafficking kinetics of NE.

5.3.1 Optimisation of fixation protocol

Utilising fixed cell samples to study the distribution of NE, has the advantage that the samples are 'frozen in time' and preserved. Hence, several areas of the same sample well may be closely examined without time limitations, providing detailed information from multiple cells. However, when utilising fixed samples, it is critical to use appropriate fixation methods to avoid studying artifacts [100]. In these experiments, not only the cells, but also the integrity of nanoemulsions may be affected by the fixation protocol, as they consist of biological lipids [100]. Of the 12 tested fixation protocols, results from 4% PFA in PBS for 15 min at room temperature were most similar to the live cells, in the most reproducible manner, in accordance with results from Kok et al. [101].

Instead of showing NE fluorescence in fluorescent spots like in live cells, most fixation protocols produced cells with diffuse rhodamine-PE fluorescence intensity throughout the cells. This might indicate that somehow, these fixation protocols disrupt the integrity of the NE, and cause spreading of the fluorescently labelled lipids (rhodamine-PE). Especially fixation performed on ice provided poor results for all variables tested. In accordance with this, DiDonato et al. [100] found that fixation on ice led to extraction of lipids and disruption of lipid-based structures, while fixation with PFA at room temperature allowed the cells to retain their lipid content.

In accordance with FCM data, fluorescence intensity from RAD-NE was significantly weaker than from RGD-NE with the same microscope settings for both live and fixed samples. The fluorescent spots visible within each cell area, may both be internalised NE and surface-bound NE. However, as only a thin optical section of the cells are imaged, fluorescent spots close the the nuclei are most likely internalised NE.

Although fixation with 4% PFA for 15 min at room temperature provided reproducible results resembling live cell samples, none of the images appeared exactly like the live cell images. Therefore, we chose to focus on live cell imaging in further development of a protocol to monitor intracellular NE distribution during NE-incubation.

5.3.2 Real-time imaging of NE incubation - optimisation for automated data analysis

The idea behind the real-time imaging experiments, was to visualise the kinetics of NE internalisation and perinuclear accumulation by plotting NE fluorescence intensity in the cell cytosol as a whole and selectively in the perinulcear region of cells, as a function of time.

Automated data analysis As imaging is a qualitative technique, it may be debated how suitable it is for studying kinetics of cellular processes. As only few cells are imaged in one experiment, it is difficult to say how representative these observations are. Therefore, in our studies, we aimed to develop a protocol where at least semi-quantitative information could be collected. By optimising the process for automated data analysis, analysis of many samples may be easily performed. As each time series typically imaged $\sim$ 10 cells, 10 experiments could be performed to gather information from 100 cells.

For cells with no cell staining, it was planned to use the first image of NE fluorescence (where cells were visible as clean, black areas), to define ROIs for whole cell cytosols. These ROIs could then be transferred to each image of the time series, to read out the fluorescence intensity at each time point. This analysis could not be performed, as cells were clearly moving and changing shape throughout the time series. New ROIs for each time point could not be defined either. Due to NE uptake and diffuse cell circumferences with time, thresholding or otherwise manipulating the images to obtain detection of the relevant ROIs, was not possible. A last alternative for analysis was to utilise bright field images to define ROIs for each time point. As the bright field images poorly visualised the cells in the imaged focal plane, this could not be performed either.

For cells stained with Hoechst and CellMask^{TM}, ROIs for the perinuclear region was planned from a dilation of detected Hoechst fluorescence and ROIs for cell cytosols were planned from CellMask^{TM} staining. Hoechst staining clearly visualised cell nuclei and was stable throughout the time series, and was therefore suitable to define ROIs for perinuclear regions. CellMask^{TM} was thought to give a nice staining of the cell circumference in the focal plane, as it marks the plasma membrane. However, the stain clearly internalised and changed throuhgout the time series. Thresholding and otherwise manipulating the images to select the desired ROIs, was not possible, and CellMask^{TM} was therefore not suitable for the analysis.

For cells stained with Hoechst and Calcein AM, analysis was planned similar to Hoechst and CellMask^{TM}. In contrast to CellMask^{TM}, the Calcein fluorescence images showed stable staining, which matched the relevant regions of interest throughout the time series. Calcein fluorescence images were thereby highly suitable to define ROIs for whole cell cytosols. Hence, the combination of Hoechst and Calcein AM stains, enables the desired automated data analysis.

No cell staining Both for NR-NE and RHO-NE, uptake of RGD-NE was clearly visible during the 30 min time series. Generally, fluorescent spots appeared within cells after 10 - 15 min. These fluorescent spots moved around within the cells and tended to gather around the nuclei approximately 20 min or longer after initiation of NE-incubation. As the NE are internalised by endcytosis [86], the fluorescent spots most likely represent vesicles containing fluorescent NE. The movement of fluorescent spots inside the cells, then likely represent trafficking of NE-containing vesicles towards the perinuclear region. The fact that we are actually able to visualise, in real-time, the movement of NE inside the cells, indicates that this real-time imaging strategy may in fact, be utilised to monitor the kinetics of NE uptake and intracellular trafficking as

intended. By simply looking at the images from these inital real-time imaging experiments, we get an impression of the timing of internalisation and trafficking processes.

The fact that uptake of RAD-NE is barely visible in the 30 min time series, is as expected. From flow cytometry experiments, uptake of RAD-NE was always significantly lower than for RGD-NE, especially at long incubation periods. With the same microscope settings, it is therefore expected that RAD-NE are less visible than RGD-NE.

The fluorescence intensity of internalised RGD-RHO-NE appeared brighter than RGD-NR-NE in the captured time series. As different fluorophores have different quantum yield and the amount of fluorophores incorpotrated in the NE may vary, this does not necessarily indicate that uptake of RHO- and NR-NE differ. It was also observed that uptake of RGD-NE occured in approximately the same amount of cells for RHO- and NR-NE. This is an indication that uptake of RHO- and NR-NE occurs similarily.

Although this real-time imaging strategy to study kinetics of NE internalisation and intracellular trafficking shows potential, a complicating factor is that only one focal plane of the cells is imaged. What occurs in this focal plane, is not necessarily representative for the rest of the cell. For example, the observation that after 10 - 15 min, all parallels show at least some fluroescent spots within cells, may lead to the assumption that initiation of RGD-NE internalisation takes approximately 10 min. This is longer than predicted from the hypothesis by Hak et al., but could fit with the suggestion that the time frame of this hypothesis is wrong. However, it is difficult to conclude on this, as we do not know what occurs in the other focal planes. To obtain this information, the time series could be imaged with z-stacks, to image all focal planes for each time point. This would take longer time, and might reduce the temporal resolution of the time series. It would also increase the laser exposure time, and increase the possibilities of inducing phototoxic effects.

Cells stained with Hoechst nuclear stain and CellMask^{TM} plasma membrane stain For cells stained with Hoechst and CellMask^{TM} prior to NE-incubation, uptake of RGD-NE was observed to occur in some regions of the imaged area, but not all. Interestingly, the images of CellMask^{TM} fluorescence, revealed that cells in the regions where no NE uptake was observed, were gradually contracting, losing cell-to-cell contact, and appeared very unhealthy by the end of the 30 min time series. These observations strongly indicate that the cells are dying and thereby detaching from the surface. Not much may be concluded about why the cells are dying, from these results. Different causes of cell death may induce different unknown effects on cell function [10]. Here, it appears that the effect causing cell death, also inhibits internalisation of RGD-NE.

Cells stained with Hoechst nuclear stain and Calcein AM cytoplasm stain For cells stained with Hoechst and Calcein AM, no uptake of either RGD- or RAD-NE was observed in any of the parallels performed. As experiments were performed both with five weeks old and freshly made NE, the possible unstability of old NE was excluded as an explanation. Especially images taken at lower magnification than the time series, visualised that the occurence of no NE uptake, was highly local. Only

cells in the area imaged in the time series and their closest neighbours, showed no NE uptake after the time series. This local effect strongly indicates that the imaging process itself may be a cause of these observations.

In the test of bleaching of internalised NE during a 30 min time series (performed on cells with already internalised NE), no reduction in intracellular fluorescence intensity was observed. Rather, an increase in intracellular fluorescence intensity was observed, most likely due to uptake of more NE during this second time series. This indicates that bleaching is most likely not the problem. Also, if bleaching was the cause of no visible NE uptake, this would not be in compliance with the fact that also surrounding cells of the imaged area, show no NE uptake.

From a closer study of the Calcein fluorescence images in image analysis softwares, it was found that also in these studies, cells contract and lose cell-to-cell contact. Again, this observation indicates that the cells are dying and detach from the surface. It was further found that this contracting movement was also visible in the rhodamine-PE fluorescence images. A fluorescence 'front' gathered around the cells and evenly moved towards the cell centres. Most likely, this fluorescence 'front' was RGD-NE bound to the cell surface, which thereby visualised the contracting movement of the cell membrane. In the one test experiment of cells stained with Hoechst only, a similar, contracting rhodamine-PE fluorescence 'front' was observed. Based on this alone, not much could be said. However, with all this information together, it indicates that also cells stained with only Hoechst may start detaching from the surface and die, during the 30 min time series.

Phototoxicity Taken together, the results indicate that both cells stained with Hoechst and CellMask^{TM}, with Hoechst and Calcein AM, and with Hoechst only, die and detach during the 30 min real-time imaging process. Also, it seems like the effect causing cell death somehow inhibit uptake of NE. For cells stained with Calcein AM, it was found that the effect of no NE uptake was highly local, only affecting a dilation of the area imaged in the time series. From these observations, it is highly likely that the effect inhibiting uptake of NE, is phototoxicity caused by laser exposure and cell stainings. Repeated exposure of fluorescently labelled cells to laser illumination, often causes phototoxic effects [87]. When fluroescent molecules are in their excited state, they may react with molecular oxygen to create free radicals that may significantly damage the cells [87, 102]. In addition to this, several studies report that constituents of culture media, like the vitamin riboflavin, may also cause light-induced damage in cultured cells [87, 103]. Also, synthetic fluorophores, like Hoechst nuclear stain, may be highly toxic to cells even at short illumination times, and short wavelength laser light in general, is more damaging to cells than longer wavelength light[87]. Together, this may nicely explain the observations in our studies. It is also in compliance with the fact that the cells with no staining, showed little effect of the laser exposure, at least during a 30 min time frame.

It might appear surprising that for cells stained with Hoechst and CellMask^{TM}, only some of the cells die and show no uptake, while for cells stained with only Hoechst, no cells show NE uptake. This most likely represent simple batch-to-batch variations in what the cells tolerate.

5.3.3 Introductory studies with transfection of GFP-tagged β_3-integrin

Transfection is known to be toxic to cells. Few transfection reagents on the market are able to achieve both high transfection efficiency and low toxicity. The extent of cellular toxicity and transfection efficiency is largely dependant on cell type and transfection reagent [104]. Also, the concentration of transfection reagent and DNA which perform well vary between cell types [104], and cell density affect transfection performance [105]. Therefore, optimisation of the transfection protocol for a specific experiment is often necessary.

Successful transfection (GFP fluorescence and relatively healthy cells), was observed after 48 h, but not after 24 h, for six of the nine transfection protocols tested. This is in accordance with information from the transfection reagent producer, suggesting to check transfection efficiency 1 - 3 days after protocols were performed [106], indicating different periods are needed to obtain transfection for different experiments. Apart from this, cytotoxicity of transfection was clearly visible at different levels in the various samples, in accordance with [104].

From the 30 min time series of NE-incubation of transfected cells, the localisation of GFP-tagged β_3-integrins became more clear. However, it was still difficult to distinguish surface and intracellular fluorescence. Nevertheless, the GFP fluorescence was mainly visible in fluorescent spots which moved around within the cell areas, similar to NE fluorescence, and a high degree of fluorescence overlap was found for these spots. This indicates that most of the GFP fluorescence detected in the time series, was GFP fluorescence in intracellular vesicles. No clear GFP signal was found at the cell circumferences, further indicating little surface expression of GFP-tagged β_3-integrins. As the time series was initiated 15 min after addition of NE, low surface expression in the time series could be due to $\alpha_v\beta_3$ internalisation upon NE exposure. However, prior to addition of NE, no clearer surface expression was observed.

Results indicating little surface expression of GFP-tagged β_3-integrins, may be representative for expression of native $\alpha_v\beta_3$-integrins in HUVEC, or it may not. To the authors knowledge, no groups have quantified the surface expression compared to intracellular expression of $\alpha_v\beta_3$-integrins in HUVEC under comparable conditions as these experiments. Therefore, it is difficult to conclude on this. As transfection cause cytotoxicity, it may, however, initiate unspecific activation of certain genes [104], which may somehow affect cellular function and expression patterns, resulting in reduced surface expression of GFP-tagged β_3-integrins compared to native $\alpha_v\beta_3$-integrins. Also, the GFP-tag on the β_3-integrins may alter protein function [107].

Another parameter to consider, is that only one focal plane was imaged in the time series, and surface-expression may be more clear in other focal planes. The fact that a high degree of fluorescent spots show co-localisation of GFP and rhodamine-PE fluroescence, might indicate that these spots are internalised vesicles where NE and GFP-tagged β_3-integrins were internalised together from the cell surface. Due to the extent of co-localised spots, this would suggest a relatively clear GFP-tagged β_3 surface expression, and that this expression is simply not visible in the imaged focal plane. To get a better impression of GFP-tagged β_3 expression in coming experiments, it would be benefitial to image multiple focal planes and create a three-dimensional image of

the cells.

In this project, only one test of nine transfection protocols was performed. Further experiments are needed to learn more about suitable transfection protocols for this DNA vector in HUVEC. Lipofectamine® 2000 was used as transfection reagent in the current experiments simply due to availability. If satisfactory results are not obtained with this reagent, other reagents may be tested, e.g. Turbofectine 8 recommended by the producer of the DNA vector [108], or Lipofectamine LTX® which was found the optimal transfection reagent for HUVEC by Hunt et al. [109].

5.3.4 Concluding remarks and further work for the imaging protocol

Studies with real-time imaging of cells incubated with NE, rapidly established that this procedure may be used to monitor the intracellular distribution of internalised NE during NE-incubation, and thereby visualise kinetics of NE internalisation and perinuclear accumulation. To be able to perform the automated data analysis we desire, we established that fluorescent markers to define the relevant ROIs (cell cytosol and perinuclear region) throughout the time series are necessary. Staining with Hoechst and Calcein AM was found suitable to detect the relevant ROIs throughout the time series. However, with these stains, phototoxic effects appeared to inhibit NE uptake and cause cell death. Due to this, no data analysis was performed in this work.

To finish the development of this imaging protocol, further optimisation needs to be performed. Although phototoxic effects were observed with Hoechst and Calcein AM staining, these stains may still be usable if microscope settings are optimised to reduce phototoxic effects. Some suggestions to changes in microscope settings to achieve this, could be; to reduce laser intensities and rather increase detector gains to visualise the fluorophores, exchange the short-wavelenght 405 nm laser with a multiphoton laser, and capture the time series with lower temporal resolution. Also, staining may be optimised to use as low concentrations as possible while still visualising the desired ROIs clear enough. In addition, time series captured with no cell staining were performed with pixel size 512×512, while the rest were captured with 1024×1024. By reducing the resolution to 512×512 again, laser exposure and thereby phototoxic effects may be reduced.

Such optimisation to reduce phototixic effects is comprehensive and time consuming. However, if this is achieved for Hoechst and Calcein AM, the data analysis will be straightforward to perform as the analysis script to perform the desired analysis is, in fact, already written. If it is not achieved to reduce phototoxic effects for Hoechst and Calcein-AM staining, other stains may be tested. If so, fluorophores excited at longer wavelengths should be chosen over shorter wavelengths, to reduce chances of phototoxicity [87].

For minitoring of the distribution of $\alpha_v\beta_3$-integrins during NE-incubation, one initial test experiment with transfection of a GFP-tagged β_3-integrin was performed. As $\alpha_v\beta_3$-integrin is the only β_3-containing integrin in HUVEC [81], successful transfection of a GFP-tagged β_3-integrin should provide a suitable and selective marker for $\alpha_v\beta_3$. Although GFP-fluorescence was observed, it is difficult to conclude if the expression

is representative for native $\alpha_v\beta_3$-integrins, and further studies are needed to optimise transfection protocols and investigate expression in closer detail.

If representative expression of GFP-tagged β_3-integrin is obtained, this could be used to monitor kinetics of $\alpha_v\beta_3$ internalisation and recycling during NE-incubation. By defining an ROI for the plasma membrane (could be done by a dilation of the Calcein fluorescence image) and the cell cytosol, the fluroescence intensity of $\alpha_v\beta_3$-integrins on the cell surface and intracellularly could be detected at each time point. If NE-incubation induce rapid internalisation of the majority of $\alpha_v\beta_3$-integrins, this should be detectable as a decrease in fluroescence intensity in the cell membrane ROIs, and an increase in fluorescence intensity in the cytosol ROIs.

In total, the work in this project has not managed to fully develop an experimental protocol where the cellular distribution of $\alpha_v\beta_3$-integrins and RGD-NE may be monitored during NE-incubation. However, this work represents the beginning of this development.

6 Conclusion

Through experiments presented in this thesis, it has become clear that the hypothesis proposed by Hak et al. [9] concerning receptor recycling as a cause of *in vivo* targeting periodicity for RGD-NE, is most likely not correct. The seperate events contained in the hypothesis (binding, induced internalisation and recycling as a pool of $\alpha_v\beta_3$-integrins) is not proved wrong, but if these events all occur, the work in this thesis indicate that the time frame suggested by Hak et al. is too short. Especially, the suggestion that the *majority* of $\alpha_v\beta_3$-integrins internalise *within minutes* upon RGD-NE exposure, appears unlikely. Evidence is presented herein suggesting that a minimum time of 10 min is needed for RGD-NE to induce $\alpha_v\beta_3$ internalisation, and that the extent of internalisation is more moderate.

The work in this thesis has also shown that real-time imaging of HUVEC incubated with NE, may be used to study kinetics of NE uptake and intracellular trafficking to the perinuclear region. Stainings which allow automated data analysis to relatively easy obtain semi-quantitative data was also established. However, phototoxicity causing inhibition of NE uptake and cell death was observed with these stainings, and optimisation of the imaging process is needed to conduct the intended experiments. To monitor $\alpha_v\beta_3$-distribution during NE-incubation, transfection of GFP-tagged β_3-integrin represents an alternative, but cytotoxicity of transfection may pose a problem.

References

[1] B. W. Stewart and C. P. Wild. *World Cancer Report 2014*. IARC, 2014.

[2] James R. Heath, Mark E. Davis, and Leroy Hood. Nanomedicine Targets Cancer. *Scientific American*, 300(2):44–51, February 2009.

[3] Piotr Grodzinski, Mike Silver, and Linda K Molnar. Nanotechnology for cancer diagnostics: promises and challenges. *Expert review of molecular diagnostics*, 6(3):307–18, May 2006.

[4] Samuel A Wickline and Gregory M Lanza. Molecular imaging, targeted therapeutics, and nanoscience. *Journal of cellular biochemistry. Supplement*, 39:90–7, January 2002.

[5] Willem J M Mulder, Daisy W J van der Schaft, Petra a I Hautvast, Gustav J Strijkers, Gerben a Koning, Gert Storm, Kevin H Mayo, Arjan W Griffioen, and Klaas Nicolay. Early in vivo assessment of angiostatic therapy efficacy by molecular MRI. *The FASEB journal : official publication of the Federation of American Societies for Experimental Biology*, 21(2):378–383, 2007.

[6] Sjoerd Hak. *Optimization of oil-in-water nanoemulsions for tumor targeting and molecular dynamic contrast enhanced MRI*. PhD thesis, Norwegian University of Science and Technology, Faculty of Medicine, Department of Cancer Research and Molecular Medicine., 2013.

[7] Margret Schottelius, Burkhardt Laufer, Horst Kessler, and Hans-Jürgen Wester. Ligands for mapping alphavbeta3-integrin expression in vivo. *Accounts of chemical research*, 42(7):969–980, 2009.

[8] Yu Sakurai, Hiroto Hatakeyama, Yusuke Sato, Mamoru Hyodo, Hidetaka Akita, Noritaka Ohga, Kyoko Hida, and Hideyoshi Harashima. RNAi-mediated gene knockdown and anti-angiogenic therapy of RCCs using a cyclic RGD-modified liposomal-siRNA system. *Journal of Controlled Release*, 173(1):110–118, 2014.

[9] Sjoerd Hak, Jana Cebulla, Else Marie Huuse, Catharina De L Davies, Willem J M Mulder, Henrik B W Larsson, and Olav Haraldseth. Periodicity in tumor vasculature targeting kinetics of ligand-functionalized nanoparticles studied by dynamic contrast enhanced magnetic resonance imaging and intravital microscopy. *Angiogenesis*, 17(1):93–107, 2014.

[10] Wayne M. Becker, Jeff Hardin, Gregory P. Bertoni, and Lewis J. Kleinsmith. *Becker's World of the Cell*. Pearson, San Francisco, eighth edi edition, 2011. Chapter 4, 19, 24.

[11] Dan Peer, Jeffrey M Karp, Seungpyo Hong, Omid C Farokhzad, Rimona Margalit, and Robert Langer. Nanocarriers as an emerging platform for cancer therapy. *Nature nanotechnology*, 2(12):751–60, December 2007.

[12] Ki Hyun Bae, Hyun Jung Chung, and Tae Gwan Park. Nanomaterials for cancer therapy and imaging. *Molecules and cells*, 31(4):295–302, April 2011.

[13] Weibo Cai and Xiaoyuan Chen. Nanoplatforms for targeted molecular imaging in living subjects. *Small (Weinheim an der Bergstrasse, Germany)*, 3(11):1840–54, November 2007.

[14] Alex G Cuenca, Huabei Jiang, Steven N Hochwald, Matthew Delano, William G Cance, and Stephen R Grobmyer. Emerging implications of nanotechnology on cancer diagnostics and therapeutics. *Cancer*, 107(3):459–66, August 2006.

[15] Volker Wagner, Anwyn Dullaart, Anne-Katrin Bock, and Axel Zweck. The emerging nanomedicine landscape. *Nature biotechnology*, 24(10):1211–7, October 2006.

[16] Agnieszka Z Wilczewska, Katarzyna Niemirowicz, Karolina H Markiewicz, and Halina Car. Nanoparticles as drug delivery systems. *Pharmacological reports : PR*, 64(5):1020–37, January 2012.

[17] Kwangjae Cho, Xu Wang, Shuming Nie, Zhuo Georgia Chen, and Dong M Shin. Therapeutic nanoparticles for drug delivery in cancer. *Clinical cancer research : an official journal of the American Association for Cancer Research*, 14(5):1310–6, March 2008.

[18] K K Jain. Nanodiagnostics: application of nanotechnology in molecular diagnostics. *Expert review of molecular diagnostics*, 3(2):153–61, March 2003.

[19] Che-Ming Jack Hu and Liangfang Zhang. Nanoparticle-based combination therapy toward overcoming drug resistance in cancer. *Biochemical pharmacology*, 83(8):1104–11, April 2012.

[20] Sinéad M Ryan, Giuseppe Mantovani, Xuexuan Wang, David M Haddleton, and David J Brayden. Advances in PEGylation of important biotech molecules: delivery aspects. *Expert opinion on drug delivery*, 5(4):371–83, April 2008.

[21] Melissa D Howard, Michael Jay, Thomas D Dziubla, and Xiuling Lu. Pegylation of nanocarrier drug delivery systems: state of the art. *Journal of Biomedical Nanotechnology*, 4(2):133–148, 2008.

[22] M Babincová, P Čičmanec, V Altanerová, Č Altaner, and P Babinec. AC-magnetic field controlled drug release from magnetoliposomes: design of a method for site-specific chemotherapy. *Bioelectrochemistry*, 55(1-2):17–19, January 2002.

[23] Tove J Evjen, Esben A Nilssen, Sabine Barnert, Rolf Schubert, Martin Brandl, and Sigrid L Fossheim. Ultrasound-mediated destabilization and drug release from liposomes comprising dioleoylphosphatidylethanolamine. *European journal of pharmaceutical sciences : official journal of the European Federation for Pharmaceutical Sciences*, 42(4):380–6, March 2011.

[24] Sjoerd Hak, Honorius M H F Sanders, Gustav J Strijkers, and Klaas Nicolay. Lipid-Based Nanoparticles as MRI Contrast Agents: Characterization and Application. In Hari Singh Nalwa, editor, *Encyclopedia of nanoscience and nanotechnology*, volume 15, pages 494–519(427). American Scientific Publisher, 2011.

[25] Hervé Hillaireau and Patrick Couvreur. Nanocarriers' entry into the cell: relevance to drug delivery. *Cellular and molecular life sciences : CMLS*, 66(17):2873–96, September 2009.

[26] Sabrina Benedetto, Roberta Pulito, Simonetta Geninatti Crich, Guido Tarone, Silvio Aime, Lorenzo Silengo, and Jörg Hamm. Quantification of the expression level of integrin receptor $\alpha v\beta 3$ in cell lines and MR imaging with antibody-coated iron oxide particles. *Magnetic Resonance in Medicine*, 56(4):711–716, 2006.

[27] Sneha S Kelkar and Theresa M Reineke. Theranostics: combining imaging and therapy. *Bioconjugate chemistry*, 22(10):1879–903, October 2011.

[28] Twan Lammers, Fabian Kiessling, Wim E Hennink, and Gert Storm. Nanotheranostics and image-guided drug delivery: current concepts and future directions. *Molecular pharmaceutics*, 7(6):1899–912, December 2010.

[29] Uma Prabhakar, Hiroshi Maeda, Rakesh K Jain, Eva M Sevick-Muraca, William Zamboni, Omid C Farokhzad, Simon T Barry, Alberto Gabizon, Piotr Grodzinski, and David C Blakey. Challenges and key considerations of the enhanced permeability and retention effect for nanomedicine drug delivery in oncology. *Cancer research*, 73(8):2412–7, April 2013.

[30] R K Jain. Transport of molecules across tumor vasculature. *Cancer metastasis reviews*, 6(4):559–93, January 1987.

[31] Hideaki Nakamura, Fang Jun, and Hiroshi Maeda. Development of next-generation macromolecular drugs based on the EPR effect: challenges and pitfalls. *Expert opinion on drug delivery*, pages 1–12, November 2014.

[32] Daishun Ling, Wooram Park, Sin-Jung Park, Yang Lu, Kyoung Sub Kim, Michael J Hackett, Byung Hyo Kim, Hyeona Yim, Yong Sun Jeon, Kun Na, and Taeghwan Hyeon. Multifunctional tumor pH-sensitive self-assembled nanoparticles for bimodal imaging and treatment of resistant heterogeneous tumors. *Journal of the American Chemical Society*, 136(15):5647–55, April 2014.

[33] Q A Pankhurst, J Connolly, S K Jones, and J Dobson. Applications of magnetic nanoparticles in biomedicine. *Journal of Physics D: Applied Physics*, 36(13):R167–R181, July 2003.

[34] Roel Deckers and Chrit T W Moonen. Ultrasound triggered, image guided, local drug delivery. *Journal of controlled release : official journal of the Controlled Release Society*, 148(1):25–33, November 2010.

[35] Kerry G Baker, Valma J Robertson, and Francis A Duck. A Review of Therapeutic Ultrasound: Biophysical Effects. *Physical Therapy*, 81(7):1351–1358, July 2001.

[36] Steven Mo, Constantin-C Coussios, Len Seymour, and Robert Carlisle. Ultrasound-enhanced drug delivery for cancer. *Expert opinion on drug delivery*, 9(12):1525–38, December 2012.

[37] William G Pitt, Ghaleb A Husseini, and Bryant J Staples. Ultrasonic drug delivery–a general review. *Expert opinion on drug delivery*, 1(1):37–56, November 2004.

[38] Victor Frenkel. Ultrasound mediated delivery of drugs and genes to solid tumors. *Advanced drug delivery reviews*, 60(10):1193–208, June 2008.

[39] R K Jain. Delivery of molecular medicine to solid tumors. *Science (New York, N.Y.)*, 271(5252):1079–80, February 1996.

[40] Vikash P Chauhan, Triantafyllos Stylianopoulos, Yves Boucher, and Rakesh K Jain. Delivery of molecular and nanoscale medicine to tumors: transport barriers and strategies. *Annual review of chemical and biomolecular engineering*, 2:281–98, January 2011.

[41] Elisabeth Garanger, Didier Boturyn, Jean-Luc Coll, Marie-Christine Favrot, and Pascal Dumy. Multivalent RGD synthetic peptides as potent alphaVbeta3 integrin ligands. *Organic & biomolecular chemistry*, 4(10):1958–65, May 2006.

[42] Judah Folkman. Angiogenesis. *Annual review of medicine*, 57:1–18, January 2006.

[43] J Folkman. Tumor angiogenesis: therapeutic implications. *The New England journal of medicine*, 285(21):1182–6, November 1971.

[44] R.E. Bridgewater, J.C. Norman, and P.T. Caswell. Integrin trafficking at a glance. 2012.

[45] Alison L Dunehoo, Meagan Anderson, Sumit Majumdar, Naoki Kobayashi, Cory Berkland, and Teruna J Siahaan. Cell adhesion molecules for targeted drug delivery. *Journal of pharmaceutical sciences*, 95(9):1856–72, September 2006.

[46] Sara M Weis and David A Cheresh. αV integrins in angiogenesis and cancer. *Cold Spring Harbor perspectives in medicine*, 1(1):a006478, September 2011.

[47] E Ruoslahti. RGD and other recognition sequences for integrins. *Annual review of cell and developmental biology*, 12:697–715, January 1996.

[48] Rita Silva, Gabriela D'Amico, Kairbaan M Hodivala-Dilke, and Louise E Reynolds. Integrins: the keys to unlocking angiogenesis. *Arteriosclerosis, thrombosis, and vascular biology*, 28(10):1703–13, October 2008.

[49] D F Legler, G Wiedle, F P Ross, and B A Imhof. Superactivation of integrin alphavbeta3 by low antagonist concentrations. *Journal of cell science*, 114(Pt 8):1545–53, April 2001.

[50] Thomas J. Wickham, Patricia Mathias, David A. Cheresh, and Glen R. Nemerow. Integrins αvβ3 and αvβ5 promote adenovirus internalization but not virus attachment. *Cell*, 73(2):309–319, April 1993.

[51] Yuanming Zhang and Jeffrey M Bergelson. Adenovirus receptors. *Journal of virology*, 79(19):12125–31, October 2005.

[52] Kai Temming, Raymond M Schiffelers, Grietje Molema, and Robbert J Kok. RGD-based strategies for selective delivery of therapeutics and imaging agents

to the tumour vasculature. *Drug resistance updates : reviews and commentaries in antimicrobial and anticancer chemotherapy*, 8(6):381–402, December 2005.

[53] Glen R Nemerow. A new link between virus cell entry and inflammation: adenovirus interaction with integrins induces specific proinflammatory responses. *Molecular therapy : the journal of the American Society of Gene Therapy*, 17(9):1490–1, September 2009.

[54] Patrick T. Caswell and Jim C. Norman. Integrin trafficking and the control of cell migration. *Traffic*, 7(1):14–21, 2006.

[55] Zhaoming Guo, Bing He, Hongwei Jin, Haoran Zhang, Wenbing Dai, Liangren Zhang, Hua Zhang, Xueqing Wang, Jiancheng Wang, Xuan Zhang, and Qiang Zhang. Targeting efficiency of RGD-modified nanocarriers with different ligand intervals in response to integrin $\alpha v\beta 3$ clustering. *Biomaterials*, 35(23):6106–17, July 2014.

[56] Quinn K T Ng, Marie K Sutton, Pan Soonsawad, Li Xing, Holland Cheng, and Tatiana Segura. Engineering clustered ligand binding into nonviral vectors: alphavbeta3 targeting as an example. *Molecular therapy : the journal of the American Society of Gene Therapy*, 17(5):828–36, May 2009.

[57] Didier Boturyn, Jean-Luc Coll, Elisabeth Garanger, Marie-Christine Favrot, and Pascal Dumy. Template assembled cyclopeptides as multimeric system for integrin targeting and endocytosis. *Journal of the American Chemical Society*, 126(18):5730–9, May 2004.

[58] Lucie Sancey, Elisabeth Garanger, Stéphanie Foillard, Guy Schoehn, Amandine Hurbin, Corinne Albiges-Rizo, Didier Boturyn, Catherine Souchier, Alexeï Grichine, Pascal Dumy, and Jean-Luc Coll. Clustering and internalization of integrin alphavbeta3 with a tetrameric RGD-synthetic peptide. *Molecular therapy : the journal of the American Society of Gene Therapy*, 17(5):837–43, May 2009.

[59] Willem J M Mulder, Gustav J Strijkers, Geralda A F van Tilborg, David P Cormode, Zahi A Fayad, and Klaas Nicolay. Nanoparticulate assemblies of amphiphiles and diagnostically active materials for multimodality imaging. *Accounts of chemical research*, 42(7):904–14, July 2009.

[60] W J M Mulder. *Lipid-based Nanoparticles for Magnetic Resonance Imaging, Design, Characterization, and Application*. PhD thesis, Eindhoven Univercity of Technology, 2006.

[61] Yechezkel Barenholz. Doxil®–the first FDA-approved nano-drug: lessons learned. *Journal of controlled release : official journal of the Controlled Release Society*, 160(2):117–34, June 2012.

[62] Michael Hughes, Shelton Caruthers, Trung Tran, Jon Marsh, Kirk Wallace, Tillman Cyrus, Kathryn Partlow, Michael Scott, Michal Lijowski, Anne Neubauer, Patrick Winter, Grace Hu, Hyuing Zhang, John McCarthy, Brian Maurizi, John Allen, Cordellia Caradine, Robert Neumann, Jeffrey Arbeit, Gregory Lanza, and Samuel Wickline. Perfluorocarbon nanoparticles for molecular imaging and targeted therapeutics. *Proceedings of the IEEE*, 96(3):397–415, 2008.

[63] Huabing Chen, Chalermchai Khemtong, Xiangliang Yang, Xueling Chang, and Jinming Gao. Nanonization strategies for poorly water-soluble drugs. *Drug discovery today*, 16(7-8):354–60, April 2011.

[64] Sjoerd Hak, Zuzana Garaiova, Linda Therese Olsen, Asbjørn Magne Nilsen, and Catharina de Lange Davies. The effects of oil-in-water nanoemulsion polyethylene glycol surface density on intracellular stability, pharmacokinetics, and biodistribution in tumor bearing mice. *Pharmaceutical research*, 32(4):1475–85, April 2015.

[65] Alice L. Givan. Principles of Flow Cytometry: An Overview. In Leslie Wilson, Paul T. Matsudaira, Zbigniew Darzynkiewicz, J. Paul Robinson, and Harry A. Crissman, editors, *Cytometry, Part A*, chapter 2. Academic Press, 3rd edition, 2000.

[66] Marco Rieseberg, Cornelia Kasper, Kenneth F. Reardon, and Thomas Scheper. Flow cytometry in biotechnology. *Applied Microbiology and Biotechnology*, 56(3-4):350–360, August 2001.

[67] Misha Rahman. Introduction to flow cytometry. *AbD SEROTECH*, 2006.

[68] Marion G. Macey. *Flow Cytometry, Principles and Applications*. Humana Press, Totowa, NJ, 2007.

[69] Nathan S Claxton, Thomas J Fellers, and Michael W Davidson. Laser scanning confocal microscopy. *Department of Optical Microscopy and Digital Imaging, Florida State University, Tallahassee, http://www. olympusconfocal. com/theory/LSCMIntro. pdf*, 2006.

[70] Ross Booth and Hanseup Kim. Characterization of a microfluidic in vitro model of the blood-brain barrier (μBBB). *Lab on a chip*, 12(10):1784–92, April 2012.

[71] P C Brooks, R A Clark, and D A Cheresh. Requirement of vascular integrin alpha v beta 3 for angiogenesis. *Science (New York, N.Y.)*, 264(5158):569–71, April 1994.

[72] LifeTechnologies. Guidelines for Maintaining Cultured Cells. `http://www.lifetechnologies.com/no/en/home/references/gibco-cell-culture-basics/cell-culture-protocols/maintaining-cultured-cells.html`. Accessed: 2015-06-04.

[73] Riccardo E Nisato, Jean-Christophe Tille, Alfred Jonczyk, Simon L Goodman, and Michael S Pepper. alphav beta 3 and alphav beta 5 integrin antagonists inhibit angiogenesis in vitro. *Angiogenesis*, 6(2):105–19, January 2003.

[74] LifeTechnologies. CellMask Plasma Membrane Stains, Molecular probes by Life Technologies. `https://tools.lifetechnologies.com/content/sfs/manuals/CellMask\_Plasma\_Membrane\_Stains\_PI.pdf`. Accessed: 2015-05-06.

[75] Invitrogen. Hoechst Stains, Molecular probes by Invitrogen. `https://www.ipmc.cnrs.fr/fichiers/recherche/microscopie/Sondes/Hoechst\_33342.pdf`. Accessed: 2015-05-06.

[76] LifeTechnologies. Calcein AM, cell-permeant dye. https://www.lifetechnologies.com/order/catalog/product/C3100MP. Accessed: 2015-05-06.

[77] Merck Millipore. MAB1976, Anti-Integrin avb3 Antibody, clone LM609. http://www.merckmillipore.com/NO/en/product/Anti-Integrin-αVβ3-Antibody\%2C-clone-LM609,MM_NF-MAB1976. Accessed: 2015-05-06.

[78] LifeTechnologies. F(ab')2-Goat anti-Mouse IgG (H+L) Secondary Antibody, Alexa Fluor 488 conjugate. https://www.lifetechnologies.com/order/genome-database/antibody/Mouse-IgG-H-L-Secondary-Antibody-Polyclonal/A-11017. Accessed: 2015-05-06.

[79] OriGeneTechnologies. ITGB3 (GFP-tagged) - Human integrin, beta 3 (platelet glycoprotein IIIa, antigen CD61). http://www.origene.com/Human_ORF/RG221606.aspx. Accessed: 2015-05-06.

[80] Evrogen. Green fluorescent protein TurboGFP. http://www.evrogen.com/products/TurboGFP/TurboGFP_Detailed_description.shtml. Accessed: 2015-05-06.

[81] D Juliano, Y Wang, C Marcinkiewicz, L A Rosenthal, G J Stewart, and S Niewiarowski. Disintegrin interaction with alpha V beta 3 integrin on human umbilical vein endothelial cells: expression of ligand-induced binding site on beta 3 subunit. *Experimental cell research*, 225(1):132–42, May 1996.

[82] LifeTechnologies. DAPI Protocol for Fluorescence Imaging. https://www.lifetechnologies.com/no/en/home/references/protocols/cell-and-tissue-analysis/protocols/dapi-imaging-protocol.html. Accessed: 2015-05-06.

[83] Peter A Jarzyna, Torjus Skajaa, Anita Gianella, David P Cormode, Daniel D Samber, Stephen D Dickson, Wei Chen, Arjan W Griffioen, Zahi A Fayad, and Willem J M Mulder. Iron oxide core oil-in-water emulsions as a multifunctional nanoparticle platform for tumor targeting and imaging. *Biomaterials*, 30(36):6947–54, December 2009.

[84] Andrey S. Klymchenko, Emilie Roger, Nicolas Anton, Halina Anton, Ievgen Shulov, Julien Vermot, Yves Mely, and Thierry F. Vandamme. Highly lipophilic fluorescent dyes in nano-emulsions: towards bright non-leaking nano-droplets. *RSC Advances*, 2(31):11876, November 2012.

[85] Sonya Cressman, Ying Sun, E. Jane Maxwell, Ning Fang, David D. Y. Chen, and Pieter R. Cullis. Binding and Uptake of RGD-Containing Ligands to Cellular α v β 3 Integrins. *International Journal of Peptide Research and Therapeutics*, 15(1):49–59, December 2008.

[86] Emily Helgesen. Characterization of the Uptake and Trafficking of avb3-targeted and Non-targeted Nanoemulsions in Human Endothelial Cells in vitro. Master's thesis, Norwegain University of Science and Technology, 2011.

[87] Nikon. Phototoxicity in Microscopy Literature References, MicroscopyU - The source for microscopy education. https://www.microscopyu.com/references/phototoxicity.html. Accessed: 2015-06-02.

[88] Sofie Snipstad, Sara Westrøm, Yrr Mørch, Mercy Afadzi, Andreas Aaslund, and Catharina de Lange Davies. Contact-mediated intracellular delivery of hydrophobic drugs from polymeric nanoparticles. *Cancer Nanotechnology*, 5(1):8, December 2014.

[89] Karen Lawler, Gerald O'Sullivan, Aideen Long, and Dermot Kenny. Shear stress induces internalization of E-cadherin and invasiveness in metastatic oesophageal cancer cells by a Src-dependent pathway. *Cancer science*, 100(6):1082–7, June 2009.

[90] M. Mutin, F. George, G. Lesaule, and J. Sampol. Reevaluation of Trypsin-EDTA for Endothelial Cell Detachment before Flow Cytometry Analysis. July 2009.

[91] Biological Industries. EDTA Solution (0.05%) in DPBS. http://www.bioind.com/page_15177. Accessed: 2015-05-28.

[92] David Perrais and Christien J Merrifield. Dynamics of endocytic vesicle creation. *Developmental cell*, 9(5):581–92, November 2005.

[93] U.S. Food and Drug Administration. Drug Development and Review Definitions. http://www.fda.gov/Drugs/DevelopmentApprovalProcess/HowDrugsareDevelopedandApproved/ApprovalApplications/InvestigationalNewDrugINDApplication/ucm176522.htm, 2015. Accessed: 2015-06-12.

[94] Alison J Woods, Dominic P White, Patrick T Caswell, and Jim C Norman. PKD1/PKCmu promotes alphavbeta3 integrin recycling and delivery to nascent focal adhesions. *The EMBO journal*, 23(13):2531–43, July 2004.

[95] Laura di Blasio, Sara Droetto, Jim Norman, Federico Bussolino, and Luca Primo. Protein kinase D1 regulates VEGF-A-induced alphavbeta3 integrin trafficking and endothelial cell migration. *Traffic (Copenhagen, Denmark)*, 11(8):1107–18, August 2010.

[96] Marnie Roberts, Simon Barry, Alison Woods, Peter van der Sluijs, and Jim Norman. PDGF-regulated rab4-dependent recycling of αvβ3 integrin from early endosomes is necessary for cell adhesion and spreading. *Current Biology*, 11(18):1392–1402, September 2001.

[97] Sergej Pirkmajer and Alexander V Chibalin. Serum starvation: caveat emptor. *American journal of physiology. Cell physiology*, 301(2):C272–9, August 2011.

[98] Patrick T Caswell, Suryakiran Vadrevu, and Jim C Norman. Integrins: masters and slaves of endocytic transport. *Nature reviews. Molecular cell biology*, 10(12):843–53, December 2009.

[99] Susanna Castel, Roser Pagan, Francesc Mitjans, Jaume Piulats, Simon Goodman, Alfred Jonczyk, Florian Huber, Senén Vilaró, and Manuel Reina. RGD Peptides and Monoclonal Antibodies, Antagonists of αv-Integrin, Enter the Cells

by Independent Endocytic Pathways. *Laboratory Investigation*, 81(12):1615–1626, December 2001.

[100] Deanna DiDonato and Dawn L Brasaemle. Fixation methods for the study of lipid droplets by immunofluorescence microscopy. *The journal of histochemistry and cytochemistry : official journal of the Histochemistry Society*, 51(6):773–80, June 2003.

[101] Maarten B Kok, Sjoerd Hak, Willem J M Mulder, Daisy W J van der Schaft, Gustav J Strijkers, and Klaas Nicolay. Cellular compartmentalization of internalized paramagnetic liposomes strongly influences both T1 and T2 relaxivity. *Magnetic resonance in medicine*, 61(5):1022–32, May 2009.

[102] Ram Dixit and Richard Cyr. Cell damage and reactive oxygen species production induced by fluorescence microscopy: effect on mitosis and guidelines for non-invasive fluorescence microscopy. *The Plant Journal*, 36(2):280–290, October 2003.

[103] Agnieszka Grzelak, Błażej Rychlik, and Grzegorz Bartosz. Light-dependent generation of reactive oxygen species in cell culture media. *Free Radical Biology and Medicine*, 30(12):1418–1425, June 2001.

[104] Laura Juckem. Cellular Toxicity Caused by Transfection: Why is it important? `http://www.biocompare.com/Bench-Tips/121111-Cellular-Toxicity-Caused-by-Transfection-Why-is-it-important/`, 2012. Accessed: 2015-06-08.

[105] LifeTechnologies. Transfection Reagent FAQs. `http://www.lifetechnologies.com/no/en/home/life-science/cell-culture/transfection/transfection-support/transfection-reagent-faqs.html`. Accessed: 2015-06-08.

[106] Invitrogen. Lipofectamine 2000 Reagent, Protocol Pub. No. MAN0007824 Rev.1.0. `http://tools.lifetechnologies.com/content/sfs/manuals/Lipofectamine\_2000\_Reag\_protocol.pdf`, 2013. Accessed: 2015-06-08.

[107] Susan B. Skube, José M. Chaverri, and Holly V. Goodson. Effect of GFP tags on the localization of EB1 and EB1 fragments in vivo. *Cytoskeleton*, 67(1):1–12, January 2010.

[108] OriGene. TrueORF cDNA Clones and PrecisionShuttle Vector System, Application Guide. `http://www.origene.com/Trueorf\_Manual.pdf`. Accessed: 2015-06-08.

[109] Michelle A Hunt, Margaret J Currie, Bridget A Robinson, and Gabi U Dachs. Optimizing transfection of primary human umbilical vein endothelial cells using commercially available chemical transfection reagents. *Journal of biomolecular techniques : JBT*, 21(2):66–72, July 2010.

Appendix A Flow cytometry data analysis

Excluding cellular fragments, debris and agglomerations from the data analysis

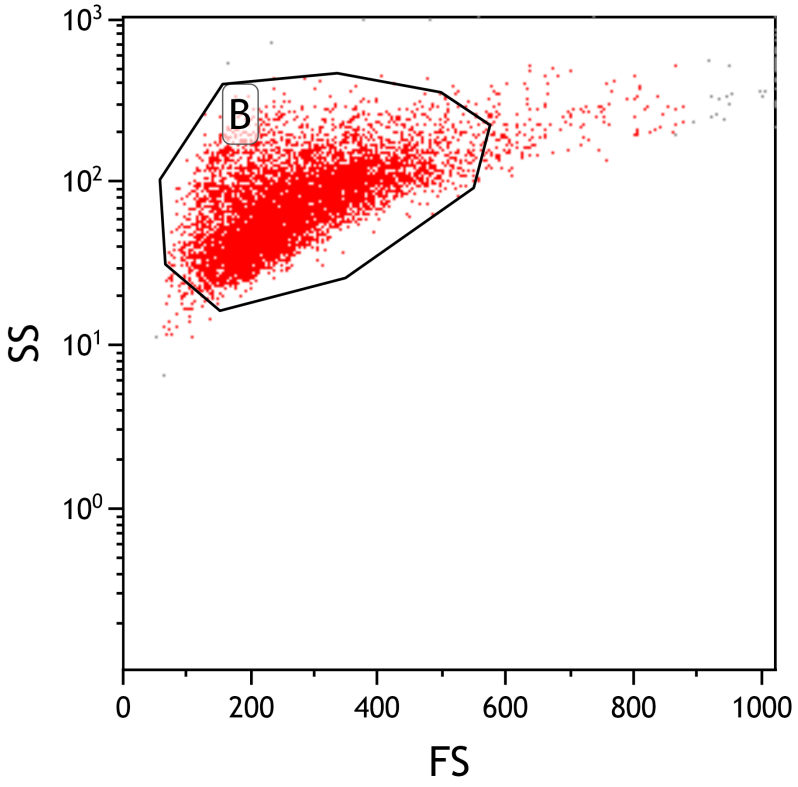

Figure 53: **Gating of SS vs FS plot** An illustration of how the side scatter (SS) vs forward scatter (FS) plot was gated to exclude cellular fragments, debris and agglomerations from the data analysis.

Determination of MFI and percentage of positive cells from raw data

Histogram overlays as presented in figure 54, were utilised to determine values for relative MFI and percentage of positive cells presented in scatter plots. The histogram overlay shows histograms for an autofluorescent sample, in addition to the treated samples. Each histogram show the number of cells (count) as a function of fluorescence intensity for the relevant sample. Under the overlay, a list of numbers is read out by the Kaluza Flow Cytometry Analysis v1.2 software. For each sample, values are read out for the whole cell population ('All') and for the cell population within defined marker lines. Here, the marker line named #1 was defined. The column '%Gated' show the percentage of cells within the relevant marker line, and 'X-med' show the median fluroescence intensity. The marker named #1 was set where the autofluorescent sample show 3% cells within this marker line. Fluorescence intensity below this marker line was considered to be autofluorescence. The percentage of positive cells for each sample was read out as the number '%Gated' within marker line #1. MFI was read out for

each sample as the number 'X-med' for the whole cell population ('All'). Relative MFI is determined by normalising the MFI for each sample towards the MFI for the autofluorescent sample.

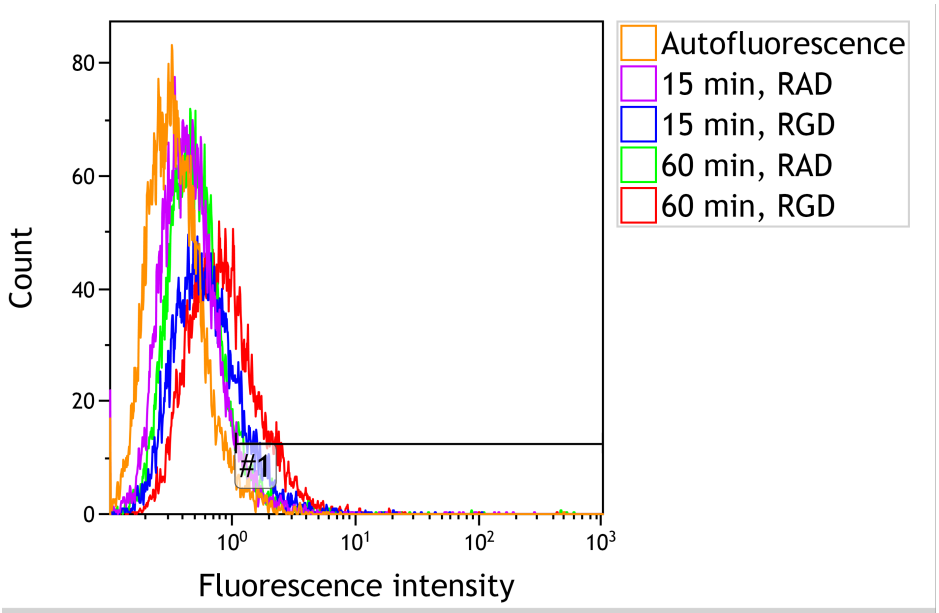

Marker	%Gated	X-Med
All	100,00	0,33
All	100,00	0,44
All	100,00	0,59
All	100,00	0,48
All	100,00	0,79
#1	2,98	1,47
#1	6,11	1,45
#1	16,49	1,50
#1	7,71	1,45
#1	30,39	1,59

Figure 54: **Raw data** Example of a histogram overlay from flow cytometry measurements, illustrating how percentage of positive cells and MFI was determined. An autofluorescent sample, and samples incubated with RGD- and RAD-RHO-NE for 15 and 60 min at 4°C are shown.

Appendix B Real-time imaging of NE incubation

Cells stained with Hoechst nuclear stain and CellMask™ plasma membrane Stain

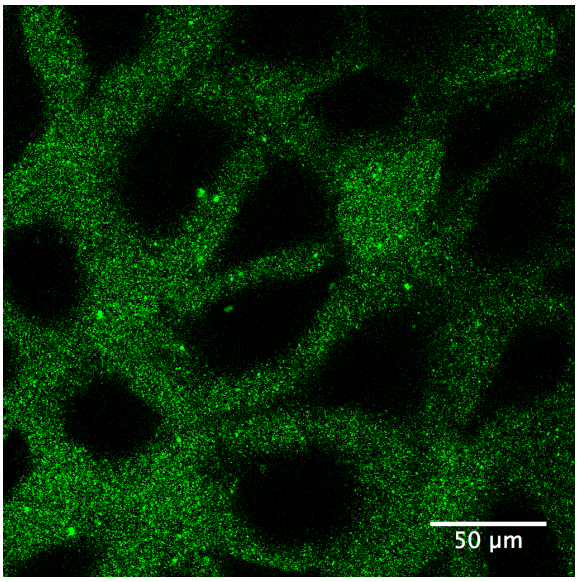

(a) First image of the time series, ∼ 2 minutes after addition of NE

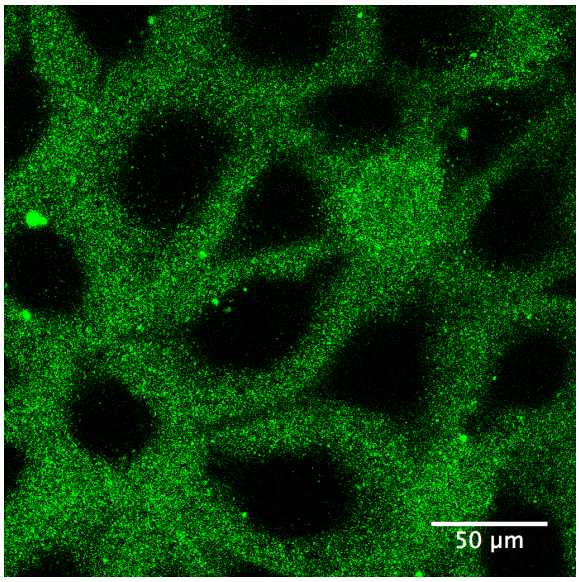

(b) 10 minutes after initiation of the time series

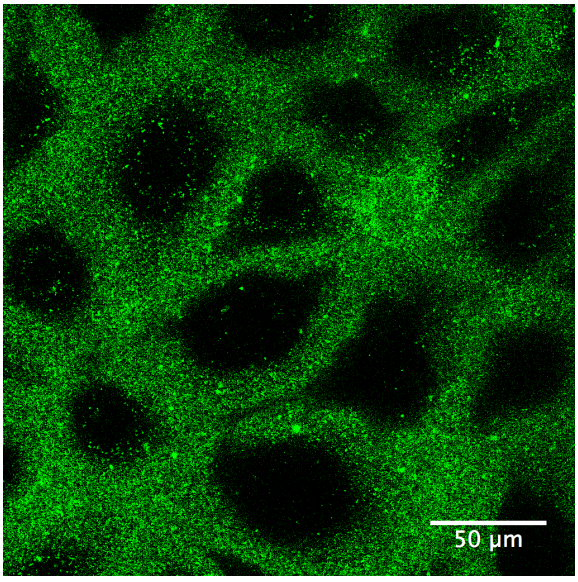

(c) 20 minutes after initiation of the time series

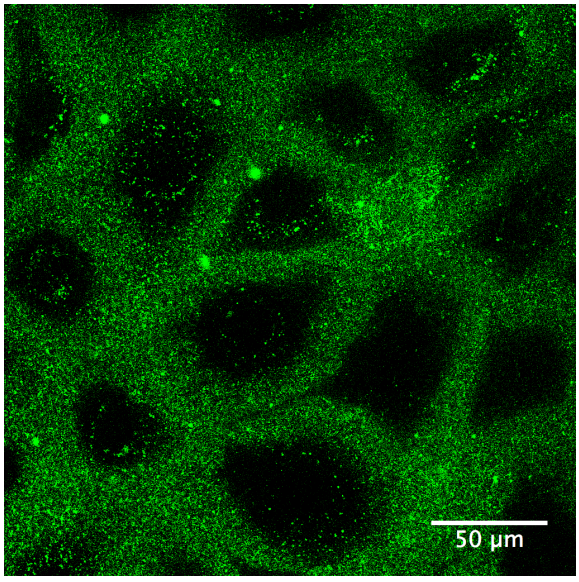

(d) 30 minutes after initiation of the time series

Figure 55: **Incubation with RGD-RHO-NE, Hoechst and CellMask™ staining** Four snapshots from a 30 min time series of HUVEC incubated with 1 mM RGD-RHO-NE captured on a confocal microscope. Cells were stained with Hoechst 34580 and CellMask™ Deep Red Plasma Membrane Stain prior to incubation. The images show the rhodamine-PE fluorescence channel visualised in green. The black areas represent cells. n = 3.

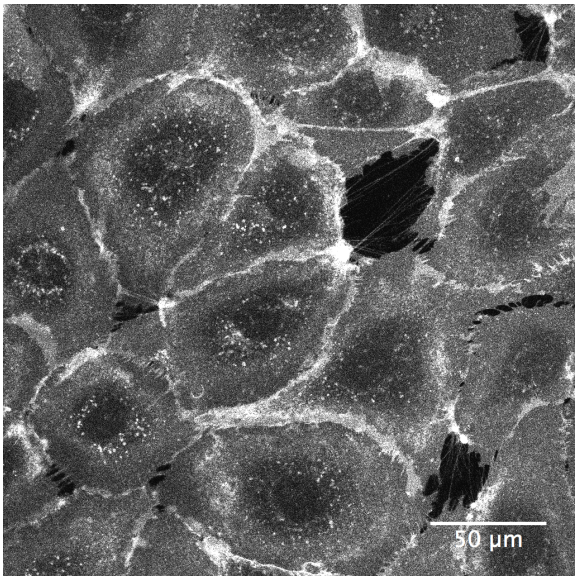

(a) First image of the time series, ∼ 2 minutes after addition of NE

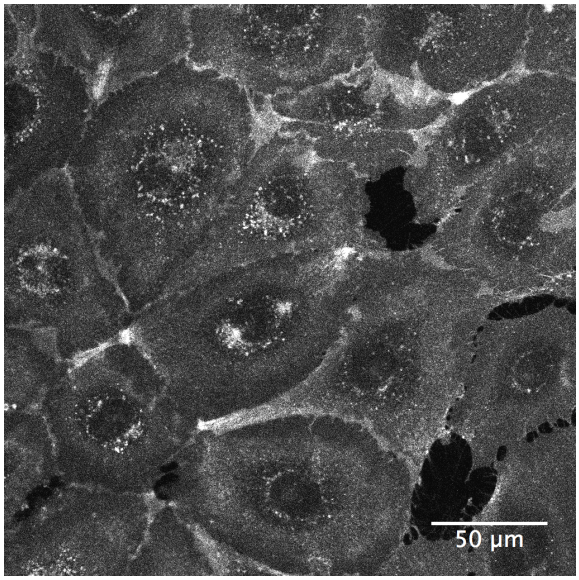

(b) 10 minutes after initiation of the time series

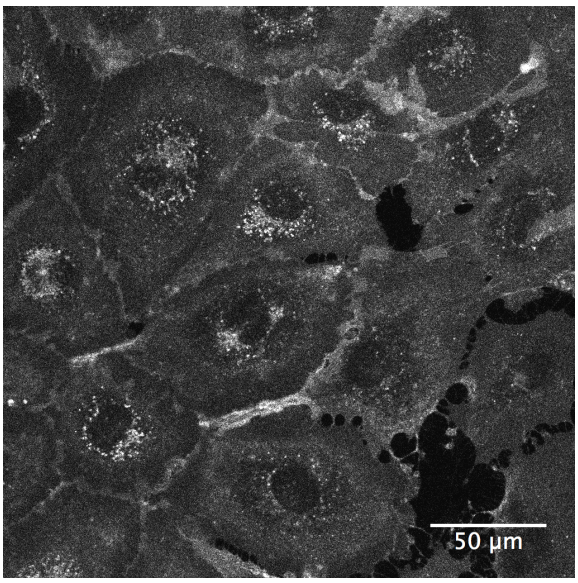

(c) 20 minutes after initiation of the time series

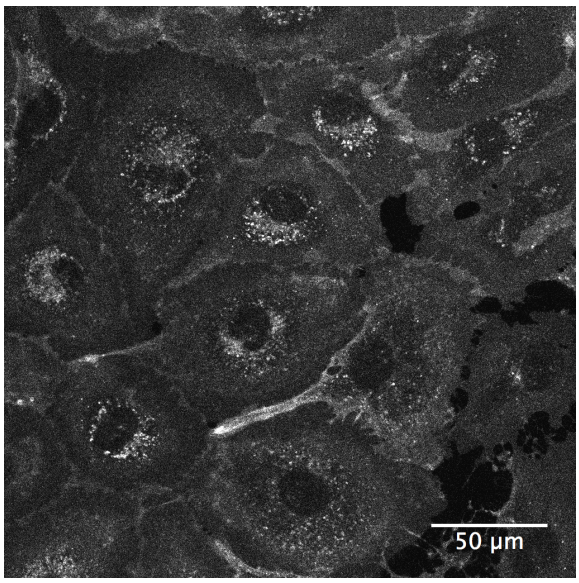

(d) 30 minutes after initiation of the time series

Figure 56: **Incubation with RGD-RHO-NE, Hoechst and CellMask™ staining** Four snapshots from the same 30 min time series of HUVEC incubated with 1 mM RGD-RHO-NE as in figure 55. Cells were stained with Hoechst 34580 and CellMask™ Deep Red Plasma Membrane Stain prior to incubation. The images show the CellMask™ Deep Red Plasma Membrane Stain fluorescence channel, visualised in white. n = 3.

Appendix C Real-time imaging of NE incubation of transfected cells

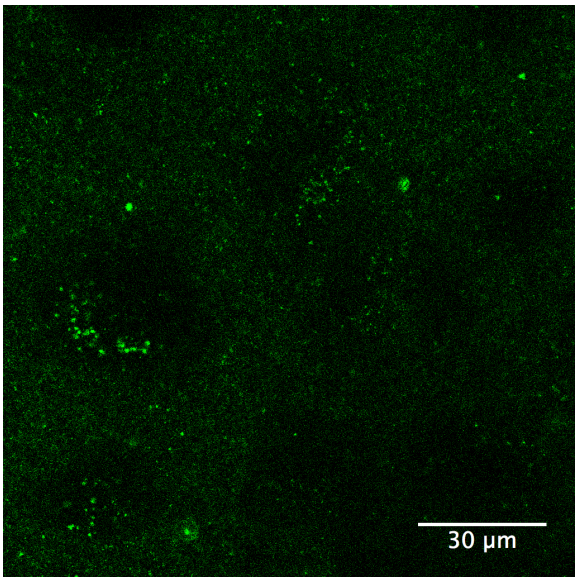

(a) First image of the timeseries, ∼ 15 minutes after addition of NE

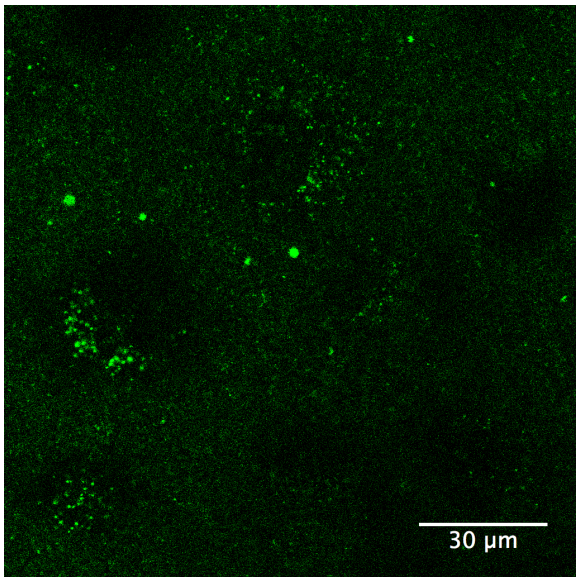

(b) 10 minutes after initiation of the timeseries. 25 minutes after addition of NE.

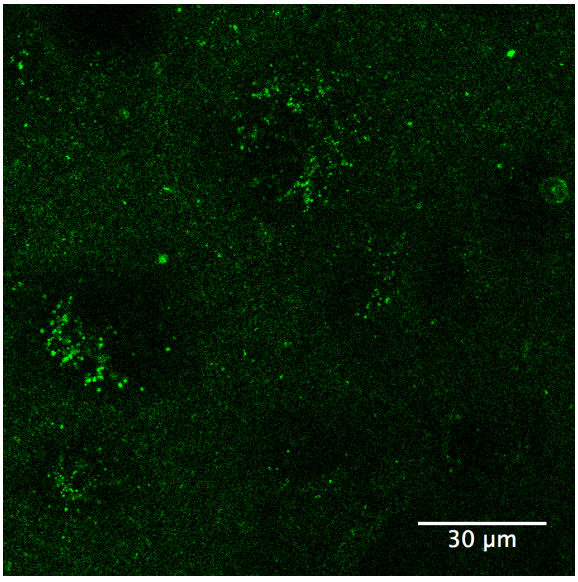

(c) 20 minutes after initiation of the timeseries. 35 minutes after addition of NE.

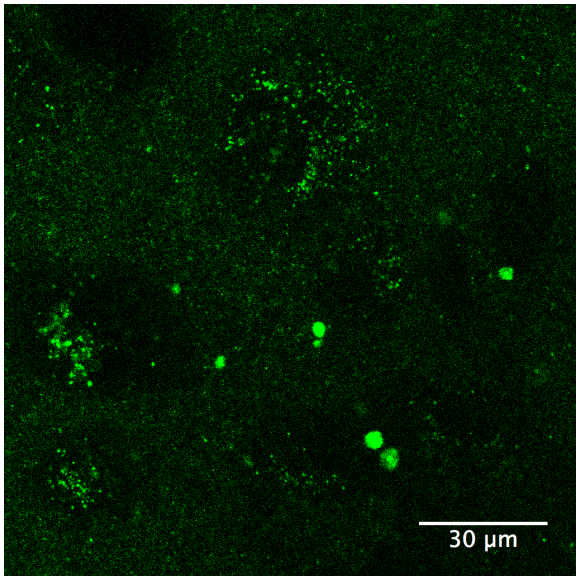

(d) 30 minutes after initiation of the timeseries. 45 minutes after addition of NE.

Figure 57: **Incubation of transfected cells with RGD-RHO-NE** Four snapshots from a 30 min time series of HUVEC incubated with 1 mM RGD-RHO-NE captured on a confocal microscope. Cells were transfected with 0.05 μg of DNA (GFP-tagged human β_3-integrin), ratio 0.5:1 of Lipofectamine® 2000 (μl) : plasmid DNA (μg) 48 h prior to incubation. The images show the rhodamine-PE fluorescence channel visualised in green. n = 1.

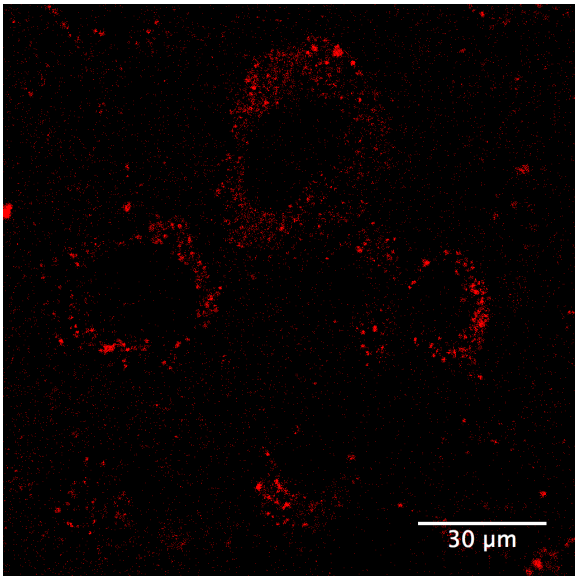

(a) First image of the timeseries, ∼ 15 minutes after addition of NE

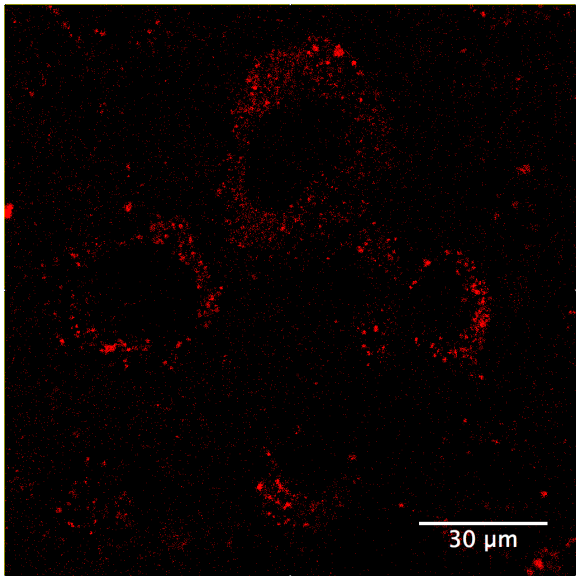

(b) 10 minutes after initiation of the timeseries. 25 minutes after addition of NE.

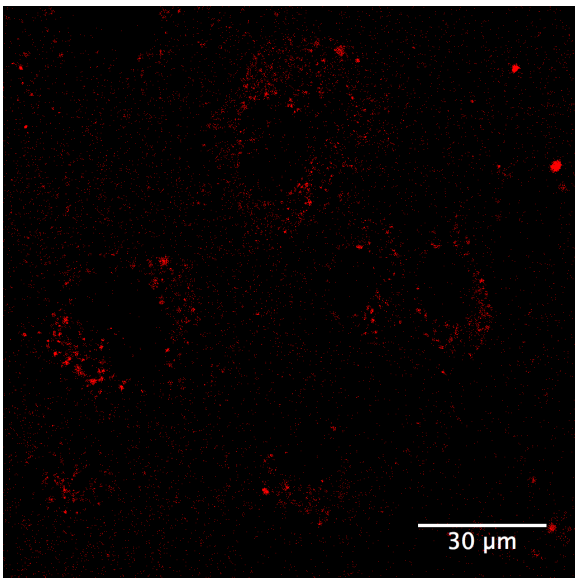

(c) 20 minutes after initiation of the timeseries. 35 minutes after addition of NE.

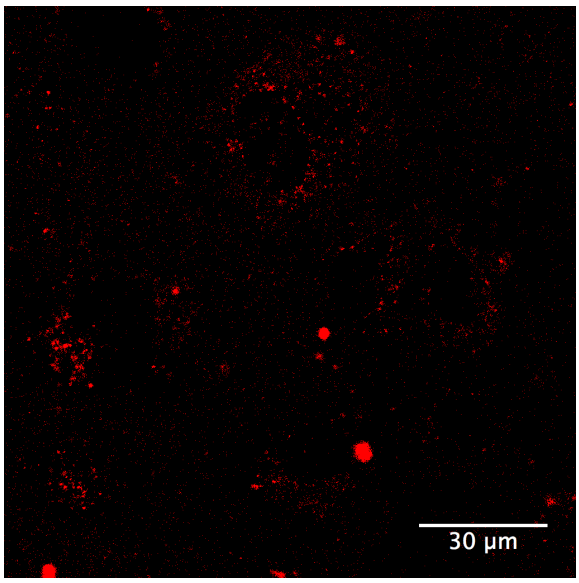

(d) 30 minutes after initiation of the timeseries. 45 minutes after addition of NE.

Figure 58: **Incubation of transfected cells with RGD-RHO-NE** Four snapshots from a 30 min time series of HUVEC incubated with 1 mM RGD-RHO-NE captured on a confocal microscope. Cells were transfected with 0.05 μg of DNA (GFP-tagged human β_3-integrin), ratio 0.5:1 of Lipofectamine® 2000 (μl) : plasmid DNA (μg) 48 h prior to incubation. The images show the GFP fluorescence channel visualised in red. n = 1.